Advanced plasma current start-up using RF heating for Tokamak fusion plasma

小島, 信一郎

出版情報：Kyushu University, 2020, 博士（工学）, 課程博士
バージョン：
権利関係：

Advanced plasma current start-up using RF heating for Tokamak fusion plasma

トカマク型核融合プラズマのための RF 加熱を用いた先進的プラズマ電流立ち上げ

Doctoral Thesis

2021

Kojima Shinichiro

（小島　信一郎）

Supervisor: Prof. Kazuaki Hanada

Interdisciplinary Graduate School of Engineering Sciences,

Kyushu University

論文要旨

トカマク型装置でプラズマ平衡を得るにはプラズマ電流が不可欠である。トカマク型装置におけるプラズマ電流立ち上げは、一般的には装置中心部の中心ソレノイド（CS）コイルによる誘導起電力を利用する誘導方式で行われる。ベータ値が高く経済的に有利な球状トカマクではCSコイル断面積が小さく誘導方式は不向きであり、非誘導方式のプラズマ電流立ち上げ手法の確立が必要である。非誘導方式の一つである電子サイクロトロン共鳴加熱・電流駆動（ECH/ECCD）によるプラズマ電流立ち上げは、真空容器内に特別な構造物の設置が不要で、長時間運転可能な高周波装置を用いるため汎用性が高い有効な手法である。これまでに基本波ECHを用いたプラズマ電流立ち上げについて数多くの研究がなされ、高い実績があげられてきた。しかしながら、プラズマ周波数が電子サイクロトロン共鳴周波数を超える高密度プラズマが生成されると基本波ECHを用いることができない。本論文では、高密度プラズマを加熱可能な高周波加熱として、磁力線に対して斜めに伝搬するQuasi-eXtraordinary mode（QX-mode）の第二高調波ECH/ECCD、及びSlow wave eXtraordinary mode（SX-mode）の高磁場側入射（高磁場側入射）による電子バーンシュタイン波（EBW）加熱の2種類の非誘導方式のプラズマ電流立ち上げを実験的に評価した結果を記述する。QX-mode第二高調波ECH/ECCDによる立ち上げでは、高調波ECH特有と考えられるバルク電子加熱からテール電子加熱への移行現象（電子エネルギー移行）を実験的に発見し、電子サイクロトロン波（ECW）の高周波電力吸収量の評価により発生機構を明らかにした。高磁場側入射によるEBW加熱を用いた方式では、パラメトリック崩壊不安定性（PDI）による崩壊波（PDW）の観測からEBWの励起を検証し、EBW加熱によるトカマク配位形成を実証した。本論文は上記の研究について以下に示す6章構成で記述する。

第1章では、核融合反応、プラズマ閉じ込め、トカマクについて解説し、球状トカマクの経済的有効性と球状トカマクにおける非誘導方式のプラズマ電流立ち上げの重要性について示し、本研究の位置づけを示す。

第2章では、QX-modeの第二高調波ECH/ECCD、及びSX-modeの高磁場側入射によるEBW加熱を用いた非誘導方式のプラズマ電流立ち上げ研究の意義を述べる。

第3章では高周波加熱によるプラズマ加熱、電流駆動を解説する。まずECWについて分散関係を解説しO-mode、X-modeの伝搬、吸収、遮断についての関係式を示す。さらに、電子サイクロトロン共鳴条件を示し、斜め入射時にはドップラー効果が強く表れることを示す。そして、ECCDの機構としてFisch-Boozer効果と電流駆動効率を低減する大河効果について解説する。次にEBWの分散関係を解説し、ECWからEBWへの3つのモード変換方法を述べる。また、EBWの励起時に発生するPDIとPDW周波数について解説する。

第4章では、28GHzのECWを用いたQX-mode第二高調波ECH/ECCDによるプラズマ電流立ち上げ実験について纏めている。実験方法、使用した主な計測装置について述べた上で、典型的な電子エネルギー移行を示す観測された特徴を報告する。電子エネルギー移行は

3 段階（A, B, C 段階）の過程により発生している。A 段階では、140 eV 程度の高いバルク電子温度、13 kA 程度の低いプラズマ電流の観測より、バルク電子加熱が示され、B 段階ではプラズマ電流は同程度でありながらもバルク電子温度が減少に伴い硬 X 線が観測され始め、バルク電子加熱からテール電子加熱への加熱の移行が見られた。C 段階では、バルク電子温度は 10 eV 程度で一定でありながら、硬 X 線強度の増加と共に 50 kA 程度までの急激なプラズマ電流上昇を観測しテール電子加熱が示された。電子エネルギー移行の発生機構の解明のためバルク電子、テール電子に対する高周波電力吸収量の数値解析を行った。シングルパス吸収を仮定して光線追跡コード RT-4 から得られる ECCD による駆動電流量と実験時の駆動電流量、及びテール電子温度・密度を含め計算した蓄積エネルギーと磁気面再構成コード EFIT から得られる実験時の蓄積エネルギーのそれぞれを比較し、双方を満たすテール電子温度、密度における高周波電力吸収量を見積もった。これにより、テール電子加熱時はテール電子の高周波電力吸収量が大半であることが示された。パワーバランスに基づいたマルチパス吸収の評価でも同様に、テール電子加熱時はテール電子の高周波電力吸収量が主となることが示された。このことにより電子エネルギー移行の発生機構として、テール電子の増加に伴ってテール電子の高周波電力吸収量がバルク電子の高周波電力吸収量を上回ると、バルク電子は加熱されず低温となり高周波電力吸収効率が低下し、テール電子は高温となり高周波電力吸収効率が増大するため、テール電子加熱が促進され続ける機構が形成されることが示された。相互相関解析から、電子密度一定時に水素原子密度に依存する水素原子のバルマー系列である H_α 光強度の減少が急激なプラズマ電流上昇より数 10 msec 程度先んじて発生していることを明らかにした。H_α 光強度の減少は電子-中性粒子衝突の低下を示すため、中性粒子の減少により電流を担うテール電子の生成が促進され、プラズマ電流が増加すると考えられる。高速カメラ画像解析から CS 壁面と接するプラズマ領域の大きさと H_α 光強度との相関が強く、これによりプラズマ-壁相互作用がプラズマ電流立ち上げに影響を与えていることが明らかになった。

第 5 章では、高磁場側入射による EBW 加熱を用いた非誘導方式プラズマ電流立ち上げ実験について纏めている。高磁場側入射による EBW の励起を明確にするため、O-mode 低磁場側入射（低磁場側入射）と比較した。開いた磁気面配位のプラズマにおいて、高磁場側入射では低磁場側入射の場合に比べプラズマ電流が 4 倍程度高く、線積分電子密度も 2 倍程度高くなることを確認した。真空容器外側に設置したアンテナを用いた漏洩高周波観測による高周波電力吸収効率推定において高磁場側入射では高周波電力吸収効率が 90%以上であることを示した。EBW の励起を確認するため、低磁場側から静電プローブを挿入し、得た信号の高速フーリエ変換解析を行うことで、PDW の検証を行った。トムソン散乱計測で得られた電子密度、温度分布より、高域混成共鳴（UHR）層位置、$R \sim 575$ mm（高磁場側入射）、$R \sim 600$ mm（低磁場側入射）において PDW 周波数は 95MHz 程度である。高磁場側入射では低磁場側入射では観測されない 80-120 MHz にスペクトルが観測され、これにより高磁場側入射においてのみ EBW の強い励起を確認した。さらに閉磁気面形成のため外部垂直

磁場曲率を調整し、高磁場側入射のみで閉磁気面の形成が確認され、プラズマ電流は 4 kA に達した。一方、低磁場側入射では、プラズマ電流値は 0.5 kA に留まった。この電流が EBWCD によるものかを確認するために、トロイダル磁場を反転させ EBWCD で期待される電流反転効果の確認をしたところ、反転効果は確認できなかった。これらの結果から、EBW による高効率のプラズマ加熱が、閉磁気面形成に十分な圧力駆動電流を生み、閉磁気面が形成されたことを確認した。

第 6 章では、本論文全体の結果を纏めている

Contents

1. Introduction

1.1 Energy production of nuclear fusion and power plant

The most promising nuclear fusion reaction is the D – T reaction that fuses their nuclei to produce an alpha particle and a neutron. The mass energy follows the total mass deficit δm thorough reaction.

$$\overset{\mathrm{D}}{(2-0.000994)m_p} + \overset{\mathrm{T}}{(3-0.006284)m_p} \rightarrow \overset{\alpha}{(4-0.027404)m_p} + \overset{\mathrm{n}}{(1+0.001378)m_p} \quad 1.1$$

m_p is the mass of proton. The mass deficit is $0.01875m_\mathrm{p}$. The released energy is

$$\varepsilon = \delta m_p c^2 = 0.001875 m_p c^2 = 17.59 \text{ MeV} \quad 1.2$$

For fusion reaction, impact energy is needed to overcome the Coulomb barrier that prevents the nucleus from approaching the nuclear dimension. The cross-section is shown in Figure 1.1 [1]. The maximum cross-section for the reaction is at over 100 keV. Due to quantum mechanical tunneling, D-T reaction occur at energies below the energy required to overcome the Coulomb barrier. The cross-sections of other reactions are also shown in Figure 1.1. D-T reaction has large cross-sections in relatively low energy for other reactions as show in Eq. 1.3, so D-T reaction is the easiest way to obtain artificially. The human begins to face energy problems and global warming. The nuclear fusion power plant will not emit greenhouse gas and use mostly eternal fuels from sea-water. It might be the ideal clean energy.

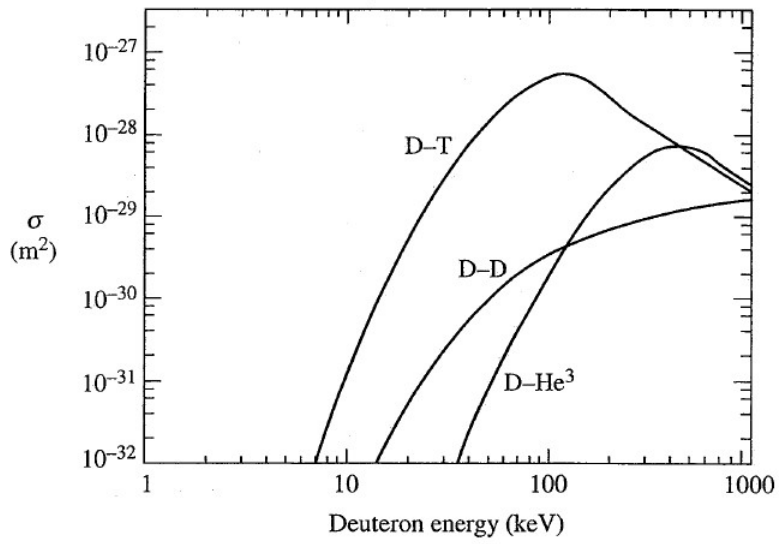

Figure 1.1 Cross-section for the D-T, D-D, D-He^3 reactions. Copied from [1]

$$\begin{aligned} \mathrm{D}^2 + \mathrm{D}^2 &\rightarrow \mathrm{He}^3 + \mathrm{n}^1 + 3.27 \text{ MeV} \\ \mathrm{D}^2 + \mathrm{D}^2 &\rightarrow \mathrm{T}^3 + \mathrm{H}^1 + 4.03 \text{ MeV} \\ \mathrm{D}^2 + \mathrm{He}^3 &\rightarrow \mathrm{He}^4 + \mathrm{H}^1 + 18.3 \text{ MeV} \end{aligned} \quad 1.3$$

1.2 Plasma confinement

The thermonuclear power per unit volume in a D-T reaction is

$$P_{thermo} = n_D n_T \langle \sigma v \rangle \varepsilon \qquad 1.4$$

where n_D and n_T are the Deuterium and Tritium densities, $\langle \sigma v \rangle$ is the reaction rate and ε is the energy released per reaction. The total density is given as n. This power is maximized by $n_D = \frac{1}{2}n$ and $n_T = \frac{1}{2}n$. Thus, the optimized thermonuclear power density is

$$p_{thermo} = \frac{1}{4} n^2 \langle \sigma v \rangle \varepsilon \qquad 1.5$$

In D-T reaction, the alpha heating sustains the reaction against the energy loss. The alpha-particles transfer their 3.5 MeV energy to the plasma through collisions, the neutrons leave the plasma without the interaction. The power should be balanced the loss and alpha-particles heating. The loss power is described by the and loss energy $W = 3\overline{nT}V$, and energy loss time τ_E. In balanced condition, the external heating is not needed.

$$\frac{3\overline{nT}V}{\tau_E} = \frac{1}{4} n^2 \langle \sigma v \rangle \varepsilon_\alpha V \qquad 1.6$$

This provides the condition for ignition.

$$n\tau_E > \frac{12T}{\langle \sigma v \rangle \varepsilon_\alpha} \qquad 1.7$$

The reaction rate can be approximately described by the temperature in range 10-20 keV within 10 % error.

$$\langle \sigma v \rangle = 1.1 \times 10^{-24} T^2 \ \text{m}^3\text{s}^{-1} \qquad 1.8$$

The alpha-energy 3.5 MeV applies in Eq. 1. 6. Then the ignition condition is

$$nT\tau_E > 3 \times 10^{21} \ \text{m}^{-3}\text{keVs} \qquad 1.9$$

This convenient form gives the clear requirements on density, temperature and confinement time. The condition shows the example of $n = 10^{20}$ m^{-3}, T=10 keV and $\tau_E = 3$ sec. The ignition condition assumes flat profiles. For parabolic density and temperature profiles the required ignition condition on the peak values is

$$\hat{n}\hat{T}\tau_E > 5 \times 10^{21} \ \text{m}^{-3}\text{keVs} \qquad 1.10$$

To achieve ignition, the high plasma density, temperature and confinement time are necessary. Because high temperatures preclude confinement by material walls, some special method of confinement is needed. Inertia and magnetic confinements are major. Inertia confinement is demonstrated by the high-power laser injections to fuel pellets and produce high density and temperature by implosion. In this method, density and temperature are high despite low confinement time. On the other hand, magnetic confinement is carried out by the magnetic structure because the charged particle follows magnetic lines.

1.3 Tokamak concept and principle

Here, a linear device is available to understand how magnetic confinement works. In the magnetic field, a charged particle moves spiral motion follow the magnetic line due to Larmor motion. The angular frequency that is named cyclotron frequency is given as $\omega_{ce} = ZeB/m$. The Larmor radius is given as $r_c = v_\perp/\omega_{ce}$. The magnetic moment is given as $\mu_m = I \cdot S = -Ze\frac{\omega_{ce}}{2\pi} \cdot \pi r_c^2 = \frac{mv_\perp^2}{2B}$ by vertical velocity for magnetic line. This magnetic moment is conserved in case of slow magnetic described by W as Eq. 1. 11.

$$W = \frac{mv^2}{2} = \frac{m(v_\perp^2+v_\parallel^2)}{2} \quad 1.\ 11$$

In the static magnetic field, the parallel velocity for magnetic field is shown by these conservative quantities.

$$v_\parallel = \pm\left\{\frac{2(W-\mu_m B)}{m}\right\}^{1/2} = \pm v\left(1-\frac{2\mu_m B}{mv^2}\right)^{1/2} \quad 1.\ 12$$

The shown equation above shows the trapping condition.

$$\frac{2\mu_m B}{mv^2} > 1 \quad 1.\ 13$$

The satisfied particle for the trapping condition is reflected at the larger magnetic field because $v_\parallel$ will be imaginary value. In case of right-hand side of Eq.1. 12 equals to zero, the charged particle is reflected and cannot pass thorough large magnetic field. The pitch angle ξ which shows the angle between velocity vector and magnetic vector is shown as $v_\perp/v = \sin\xi$. The pitch angle substates into the trapping condition of Eq. 1. 14.

$$v_\perp{}^2/v^2 = \sin^2\xi > \sin^2\xi_{loss} = \frac{B_0}{B_{max}} \quad 1.\ 14$$

where B_0 is magnetic field between confinement coils and B_{max} is the highest magnetic field. The ratio of B_0/B_{max} is named as mirror ratio. Particles having larger pitch angle than mirror ratio are trapped. The mirror configuration which is one of linear devices uses the mirror effect. However, the particles having smaller pitch angle ξ_{loss} are lost from the end. For example, GAMMA 10 tandem mirror as the representative linear device has achieved the high ion temperature above 10 keV, however the density was relatively lower (lower than 10^{18} m^{-3}) than torus devices [2]. To overcome the problem, the torus device which does not have the end is developed. The tokamak (toroidal'naya kamera s magnitnymnymi katushkami in Russian. torodail chamber with magnetic coils) is a typical toroidal device with magnetic coils. Tokamak has a toroidal magnetic field created by coaxial magnetic field coils with torus direction. The toroidal magnetic field is described by the magnetic field B_0 at the major radius R_0 which shows the radius of center plasma and radius position.

$$B_\varphi = \frac{R_0}{R} B_0 \qquad 1.15$$

The toroidal field has toroidal magnetic field gradient for radius direction. The magnetic field gradient makes the grad B drift and curvature drift as Eq. 1. 16. The drift is given as toroidal drift.

$$v_d = \left(\frac{1}{2} \frac{v_\perp^2}{\omega_{cj}} + \frac{v_\parallel^2}{\omega_{cj}} \right) \frac{B \times \nabla B}{B^2} \qquad 1.16$$

In the case of the simple torus which has only a toroidal field magnetic field, the charge separation is caused by toroidal drift because ion and electron drifts direction are the opposite. The charge separation makes the vertical electric field. The vertical electric field and the toroidal magnetic field cause E×B drift which forces charge particle outside. The simple torus has also the problem. In order to solve the problem, the poloidal magnetic field or the poloidal drift is necessary. The poloidal motion can do neutralization by connecting the separated charge particle and extinguish the vertical electric field. The best way to create poloidal magnetic field is a plasma current which is produced mainly by the current in the plasma itself, this current flowing in the toroidal direction. Thus, the plasma current drive is importance in tokamak. Tokamak is the promising candidate to achieve nuclear fusion reactor. ITER which is the largest tokamak are constructed in France with worldwide collaboration on the construction phase to prove the production of nuclear fusion energy.

1.4 Spherical tokamak

Aspect ratio *A* is defined as the ratio of major radius *R* and minor radius *a*. Spherical tokamak (ST) is a tokamak which is less aspect ratio of 2. ST has a specific magnetic construction which has long field line in high toroidal magnetic field and short field line in low toroidal magnetic field as shown in Figure 1.2. Potential advantages of ST were first suggested by Sykes and Troyon about plasma beta β. $\beta = 2p/\mu_0 B^2$ is one of important factor in tokamak to estimate plasma performance for given magnetic field. High plasma beta means that it has advantage for economy, because high plasma pressure is sustained by low magnetic field. However, magnetic hydrodynamics (MHD) instability prevents from making and keeping high plasma beta. Troyon induced the limitation of the toroidal average beta β as Eq. 1. 17.

$$\beta_{Tmax} \approx 5\beta_N \kappa / A q_a \approx \beta_N I_p / a B_T \qquad 1.17$$

Here β_N is the normalized beta, κ (=b/a) is the elongation of the plasma cross section, q_a is the safety factor at plasma edge. I_p is plasma current and B_T is the toroidal magnetic field. From this scaling, reducing *A* alone by a factor of 2 would double β_{Tmax}. This suggested the performance of tokamak plasma can be increased with increasing 1/*A* as ST.

Actually, in START which was first ST device, the expected experiment was performed. The β_T values observed were drawn as function of the normalized current I_p/aB_T as shown in Figure 1.3. A record of β_T was 40 % corresponding to β_N~6 [3]. In conventional tokamak DIII-D, the β_T was

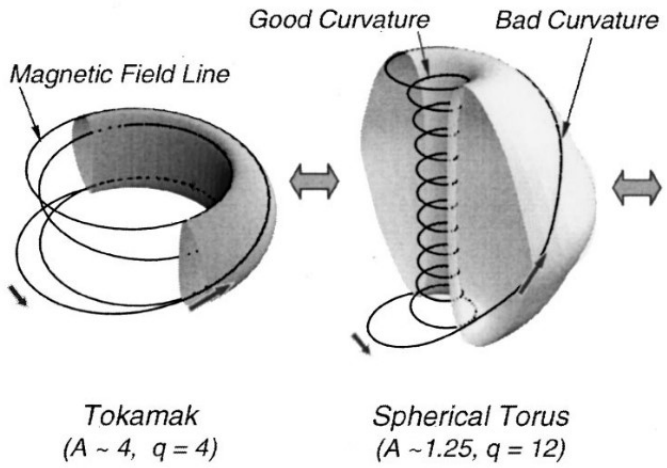

Figure 1.2 The magnetic configuration of the Spherical Tokamak and conventional tokamak. Copied from [3].

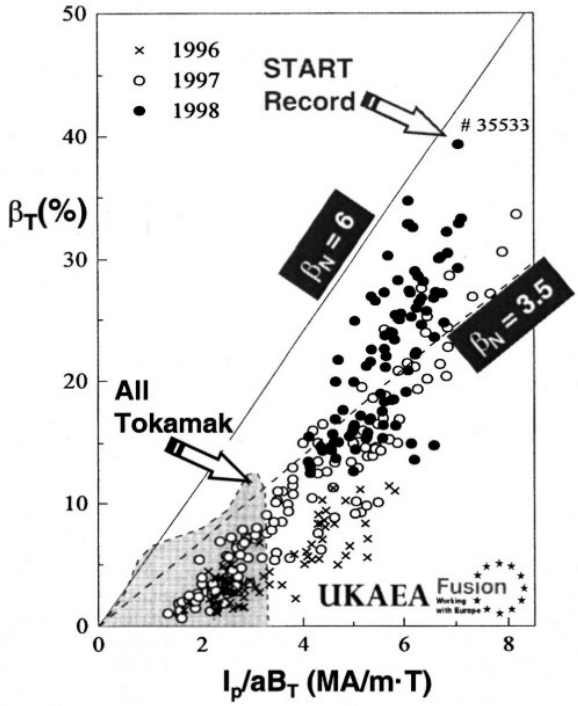

Figure 1.3 Average toroidal beta β_T measured in START during 1996-1998 as a fucntion of I_p/aB_T. Copied from [3]

11 %. The Troyon limit of $\beta_N \sim 3.5$ found in conventional tokamaks. ST beyond plasma performance of conventional tokamak. Not only START, the National Spherical Torus Experiment (NSTX) as different ST has obtained $\beta_N \sim 6.8$ and high toroidal beta $\beta_T \sim 30$ % [4]. The reason for high beta can be understood from a special magnetic configuration. The ST's specific magnetic field line

combines a short field line in bad curvature for pressure driven MHD instability in the outboard region, with the long field line of good curvature in the plasma inboard region. The increasing field line of good curvature leads to MHD stability at higher plasma beta.

ST design should make efforts to reduce center stack space. In such ST, an inductive current drive start-up is not useful, because the space available for the center solenoid is insufficient and the available Vs must be limited. This naturally leads to development of non-inductive plasma current production. There are several works on center solenoid-free current production with radio frequency (RF) as electron cyclotron resonance heating (ECRH) and an initial closed flux seed current as coaxial helicity injection (CHI) [5]. As ECRH will be equipped in nuclear fusion reactor, the study of plasma current start-up by ECRH is acceptable for nuclear fusion power plant. ECRH was used for fully non-inductive plasma current start-up in STs as LATE [6], TST-2 [7] and QUEST [8].

1.5 QUEST

Q-shu University Experiments with Steady-State Spherical Tokamak (QUEST) which is spherical tokamak experimental equipment has been operated in Advanced Fusion Research Center, Research Institute for Applied Mechanics, Kyushu university from October 2008. The purpose of QUEST was proposed as following [9].

1. To examine the steady state current drive and plasma generation by EBW.
2. To comprehensively establish recycling control base on wall temperature control, advanced wall control under high plasma performance.
3. To improve diverter concepts and to establish the way of controlling particles and heat loads during long duration operation.

In this study, the first purpose is the main motivation for the contribution on QUEST.

In Figure 1. 4Figure 1. 4, the schematic drawing of QUEST overall is shown. QUET is a medium-sized ST has a typical major radius of R = 0.64 m and a minor radius of a = 0.4 m. The radius of CS coils R_{CS} = 0.2 m. Both of the height and the diameter of the vacuum vessel is 2.8 m. QUEST has 4 poloidal field coils and 3 separated central CS coils for various shapes of magnetic configurations. Toroidal field coils are made up 2 turns and 8 coils. When current of 50 kA is turned on, 0.25 T of toroidal magnetic field is generated on R = 0.64 m. Outside of vacuum vessel, 4 pairs of poloidal field coil is installed to control position of plasma as PF1-7, PF2-6, PF3-5-1 and PF 3-5-2 (See Figure 1. 5). There are center stack coils inside of center stack (CS) of center of vacuum vessel as PF4-1, PF4-2-a, PF4-2-b and PF4-3. In additional, the cancellation coils are put around outside of the vacuum vessel.

The many heating systems are equipped in QUEST as the 8.2 GHz ECRH system, 28 GHz ECRH system and coaxial helicity injection (CHI) system and OH system. The 8.2 GHz ECRH system was utilized for wide application in QUEST. The 8.2 GHz ECRH system can operate long pulse operation for the study of the steady-state operation and the plasma wall interaction. The fully non-inductive

plasma was maintained for more than 1 hour 55 minutes by 8.2 GHz ECRH system with 40 kW [10]. An issue of uncountability of hydrogen recycling was cleared and it was explained by the model considering the presence of hydrogen transport barrier between deposited layer and the substrate. The comparison of fully non-inductive plasma start-up by 8. 2 GHz ECRH with either of fundamental resonance and second harmonic resonance was also demonstrated [11]. The 28 GHz ECRH system has a relatively higher input power of 200 kW than 8.2 GHz ECRH system. The 28 GHz gyrotron with TE8,3 cavity and a triode magnetron injection was developed by the collaboration work with Tsukuba university [12]. The maximum outpower of the gyrotron is 1 MW, and a 400 kW power capability is confirmed in QUEST experiment [13]. The fully non-inducive plasma current start-up by second harmonics ECRH was achieved mostly 70 kA [13]. CHI was equipped to achieve non-inductive plasma current drive. In HIT-II [14] and NSTX [15], CHI have been successes for non-inductive plasma current start-up. QUEST have equipped the different electrode type with HIT-II and NSTX and achieved 20 kA toroidal current as the breakdown by CHI [16]. We have tried various method to aim high beta with fully non-inductive current drive and heating system. In this study also, the improved and advanced non-inducive heating and current drive were researched.

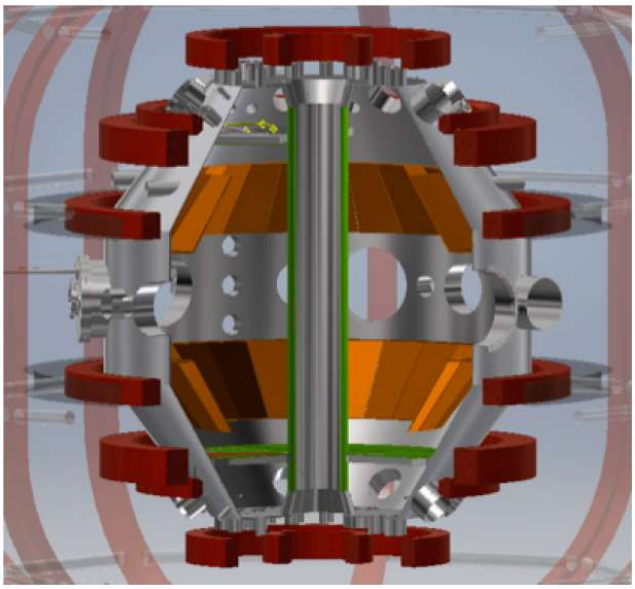

Figure 1. 4 Skematic drawing of QUEST overall.

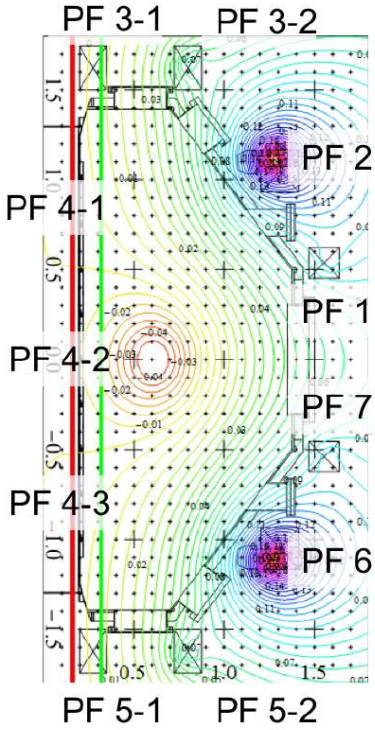

Figure. 1.5 The poloidal coil positions

2. Object and outline

ST is the economically advanced reactor formation because it has a high potential to achieve high beta. To realize ST as a future reactor system, it needs to find the most effective non-inductive current drive method. Many non-inductive current drive methods have been studied by using ECRH in DIII-D [17], TCV [18], LATE [6], TST-2 [7], QUEST [19], lower hybrid wave (LHW) in JT-60U [20], TST-2 [21], coaxial helicity injection (CHI) in NSTX [22], QUEST [16], local helicity injection in CDX [23] Pegasus [24] and plasma merging in TS-4 [25], UTST [26]. The establish of non-inductive current drive method using electron cyclotron wave (ECW) has a great impact for nuclear fusion research, because most of devices have already equipped ECRH, and ITER and DEMO. In QUEST, the ECRH has been utilized for plasma current start-up and steady-state operation. The RF heating by ECRH is commonly used many tokamaks and STs. However, the cut-off density of ECW for each propagation mode exists as shown in Figure 2.1. The commonly used ECW is O-mode fundamental ECRH by low field side injection. In case of low toroidal magnetic field scenario, ECR frequency is low. The lower plasma density than β limit density and Greenwald density would be obtained because of the lower

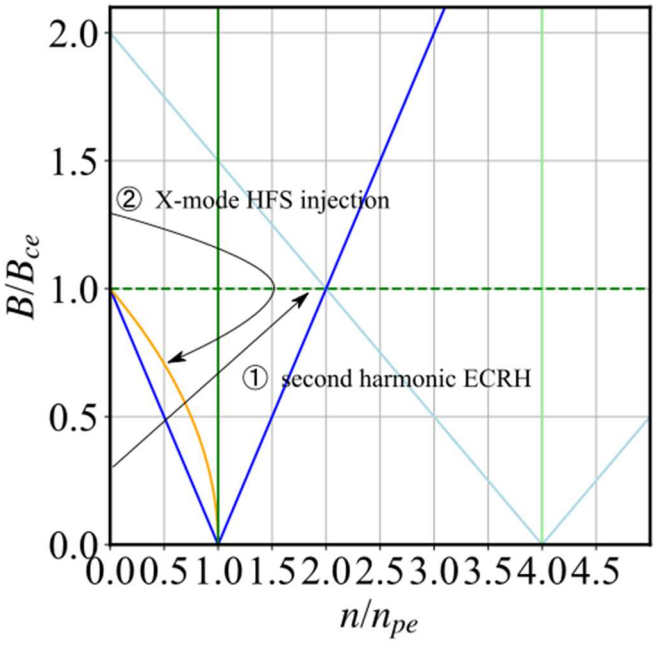

Figure 2.1: The function of normalized magnetic field for electron cyclotron resonance magnetic field against the normalized density for the O-mode cut-off density. Blue, green, orange lines are X-mode cut-off density, O-mode cut-off density and upper hybrid resonance density on each magnetic field for fundamental ECRH. Light blue, light green, orange lines are X-mode cut-off density, O-mode cut-off density and upper hybrid resonance density on each magnetic field for second harmonic ECRH.

cut-off density than those. Generally, the ST plasma is likely to have a higher electric permittivity for a relatively low magnetic field and an advanced scenario for RF plasma current start-up has been desired. My work is aimed to research the physic principle of the heating properties using advanced RF heating methods of 1) second harmonic ECRH/CD, 2) X-mode fundamental ECRH by high field side (HFS) injection to overcome the cut-off density of fundamental O-mode ECRH. The X-mode second harmonic ECRH/CD by low field side (LFS) injection of double ECW frequency can achieve double plasma cut-off density in case of vertical injection due to right-hand cut-off density. The oblique injection causes the reduction of cut-off density. The X-mode fundamental ECRH by HFS injection can also achieve double plasma cut-off density due to left-hand cut-off density. Both methods can achieve double plasma density. In this study, the plasma start-up by using advanced RF heating methods was demonstrated and investigated about specific features. The plasma start-up can be classified the four process. The four process is 1. breakdown, 2. closed flux surface formation, 3. plasma current ramp-up, 4. high density generation. However, the final process of high density generation to be suitable for neutral beam injection is not research object. This study focuses to understand the fundamental plasma physics on the plasma start-up by advanced RF heating methods as following.

1) Second harmonic ECRH is attracted not only ST devices but also large tokamak devices as JT-60 SA and ITER. The large tokamak devices operate in the low toroidal magnetic field in the initial experimental phase. The second harmonic ECRH works in half of the magnetic field to use fundamental electron cyclotron resonance. However, the finite Larmor radius effect which is not related to fundamental ECRH is strong. The higher energetic electron highly absorbs RF power. The oblique X-mode injection causes the coupling with electron having parallel velocity to drive plasma current due to high Doppler shift effect. The second harmonic ECCD by the oblique X-mode injection should heat the energetic electron that gives rise to high Doppler shift and cause the high absorption due to the high finite Larmor radius effect. Thus, we clarify the detailed knowledge of heating and current drive properties by second harmonic ECRH.

2) The X-mode fundamental ECRH by HFS injection has a potential to excite electron Bernstein wave (EBW). EBW heating (EBWH) is the most attractive method using RF in ST because of no density limitation for RF propagation. However, EBWH is difficult to demonstrate because EBW is needed to excite in plasma though mode conversion from ECW. The mode conversion was established by three methods of 1) O-X-B mode conversion by LFS oblique injection, 2) X-B mode conversion by LFS perpendicular injection, 3) X-B mode conversion by HFS injection. The X-B mode conversion by HFS injection is the most convenient way because it is expected highly efficient mode conversion with no sophisticated condition and control. To determine the EBW excitation, the collateral observation of mode conversion method should be accomplished. The observation of parametric decay instability (PDI), also known as three-wave parametric decay process which is caused by the large

amplitude of the electric filed is a good candidate for collateral observation of mode conversion. The plasma current direction by EBW current drive (EBWCD) depends on the toroidal magnetic field direction, in contrast, the plasma current direction driven by pressure depends on the poloidal magnetic field direction. Thus, we proved the EBW excitation and investigated the capability of the current drive.

This thesis is consisted of the following.

In section 3, the basic of plasma heating and current drive is introduced. Therefore, the fundamental theory for ECRH and EBW is explained.

In section 4, the heating and current drive property by 28 GHz second harmonic ECRH is indicated. The heated electron energy shift as specific heating property on second harmonic ECRH is mainly explained, and the neutral particle effect in the tail electron heating is discussed.

In section 5, X-mode HFS injection experiment for EBW excitation is described. The difference of X-mode HFS injection and O-mode LFS injection is shown. The PDI measurement is indicated as collateral evidence to show EBW excitation.

In section 6, the summary for a whole of study is shown.

3. Plasma heating and current drive by RF heating

3.1 Plasma heating and current drive system

Plasma heating and current drive system are the most important to achieve fusion reaction in tokamak. Familiar and general initial heating and current drive system are ohmic heating (OH). This method is classified as inductive heating. As non-inductive heating, neutral beam injection (NBI), ECRH, lower hybrid wave (LHW) heating and ion cyclotron resonance heating (ICRH) are known.

OH is the common method for Tokamak and will be installed in ITER also. Commonly, plasma current is driven by an induced toroidal electric field by transformer action in which a rapid flux change as known as OH. The large and rapid flux change is brought by the center solenoid coil. In the case of ITER, the ohmic plasma startup with the electric field value of ITER (0.3 V/m) is marginally possible for optimized magnetic configurations [27]. The approximation the average OH power density P_Ω is

$$P_\Omega = Ej = \eta\langle j^2\rangle \tag{3. 18}$$

where E is the inductive electric field, η is resistivity of plasma [1]. Spitzer resistivity is approximately given as

$$\eta \cong 8 \times 10^{-8} Z_{\mathrm{eff}}/T_{\mathrm{e}}^{3/2} \text{ ohm m, } T_{\mathrm{e}} \text{ in keV} \tag{3. 19}$$

The current profile is

$$j = j_0\left(1 - \frac{r^2}{a^2}\right)^n \tag{3. 20}$$

$\langle j^2\rangle$ is given by

$$\langle j^2\rangle = \frac{j_0}{2n+1} \tag{3. 21}$$

Above equations mean OH is useful in low temperature, but in high temperature cannot be useful because of low resistivity.

The inductive electric potential is given as

$$V = NS\frac{dB}{dt} \tag{3. 22}$$

OH heating is possible in the time range in which the CS coil current can rise. Thus, it is not useful for steady-state operation. Not only that but also OH heating cannot be expected for the device with a superconductor CS coil, because superconductor is difficult to change coil current immediately. In order to obtain enough inductive electric field, the cross section of CS coil is needed. In case of ST, the cross section of CS coil is quite smaller than conventional tokamak. ST needs non-inductive heating method as described in introduction. Radio frequency (RF) heating as ECRH and LHW heating have been applied as non-inductive current drive. However, in the non-inductive current drive ramp-up, the inductive current exists by the magnetic field change due to plasma current ramp-up. The

inductive current direction is opposite to the plasma current. In the case of high electron temperature, the inductive current by the plasma ramp-up by RF heating cannot be ignored due to low resistivity. In the plasma current start-up, the electron temperature tends to low and the resistivity is high. The inductive current can be ignored. In case of low toroidal electric field 1 mV/m and electron temperature 100 eV, the inductive current is approximate 400 A.

3.2 Electron cyclotron resonance heating and current drive

ECRH and ECCD by RF of the electron cyclotron frequency and its low harmonics has established and widely used to plasma heating and driving current. ECRH will be a common application in a nuclear fusion reactor because it is useful for magnetohydrodynamics stabilization not only plasma heating.

3.2.1 Dispersion relation and Propagation mode

In order to use ECW, the propagation mode should be considered. The electromagnetic wave can be complemented by Maxwell equations.

$$\nabla \times \boldsymbol{E} = -\frac{\partial \boldsymbol{B}}{\partial t}$$

$$\nabla \times \boldsymbol{B} = \mu_0 \left(J + \epsilon_0 \frac{\partial \boldsymbol{E}}{\partial t} \right) \qquad 3.23$$

The total magnetic induction and the electron number density are separated into two parts as $\boldsymbol{B}(\boldsymbol{r},t) = \boldsymbol{B}_0(\boldsymbol{r}) + \boldsymbol{B}_1(\boldsymbol{r},t)$ and $n(\boldsymbol{r},t) = n_0(\boldsymbol{r}) + n_1(\boldsymbol{r},t)$. $\boldsymbol{B}_1$ and n_1 are first-order terms. For harmonic plane wave as $\psi_j(\boldsymbol{r},t) = \psi_j \exp(i\boldsymbol{k}\cdot\boldsymbol{r} - i\omega t)$, the differential operators ∇ and $\frac{\partial}{\partial t}$ are replaced by $i\boldsymbol{k}$ and $-i\omega$ respectively [28].

$$\boldsymbol{k} \times \boldsymbol{E} = \omega \boldsymbol{B}_1$$

$$i\boldsymbol{k} \times \boldsymbol{B}_1 = \mu_0(-en_0\boldsymbol{u} - i\omega\epsilon_0\boldsymbol{E}) \qquad 3.24$$

To simplify the propagation model, we assume cold plasma model which ignores the thermal kinetic energy of the particles. The Langevin equation of motion for the electrons are described as

$$-i\omega m\boldsymbol{u} = -e(\boldsymbol{E} + \boldsymbol{u} \times \boldsymbol{B}_0) - m\nu\boldsymbol{u} \qquad 3.25$$

To derive dispersion relation for this case, equations are combined.

$$\boldsymbol{k} \times (\boldsymbol{k} \times \boldsymbol{E}) + \frac{\omega^2}{c^2}\boldsymbol{E} = \frac{i\omega e n_0}{\epsilon_0 c^2}\boldsymbol{u} \qquad 3.26$$

$$\left(1 + i\frac{\nu}{\omega}\right)\boldsymbol{u} + \frac{ie}{m\omega}(\boldsymbol{u} \times \boldsymbol{B}_0) = -\frac{ie}{m\omega}\boldsymbol{E} \qquad 3.27$$

In here, a Cartesian coordinate system is applied, and $\mathbf{z}$ is the direction of $\mathbf{B}_0$. k is shown by the angle θ for $\mathbf{B}_0$ as Figure 3.1.

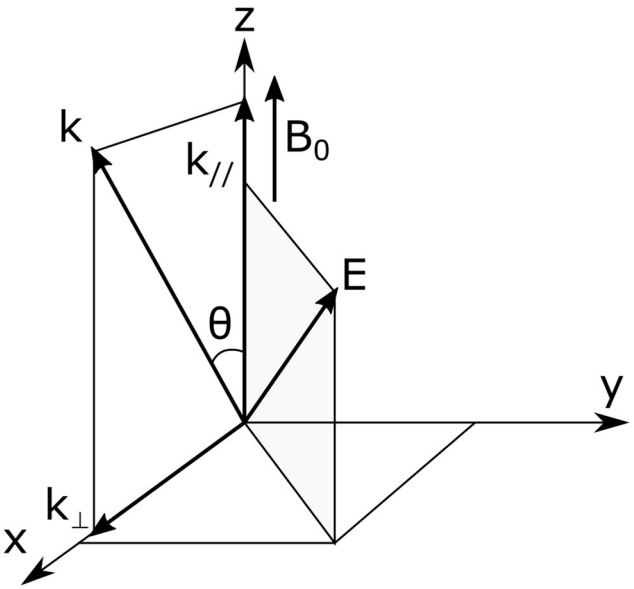

Figure 3.3 Cartesian coordinate system (x, y, z), chosen such that z is along $\mathbf{B}_0$ and y is perpendicular to the plane formed by $\mathbf{B}_0$ and **k**.

$$\boldsymbol{k} = k\sin\theta\,\hat{x} + k\cos\theta\,\hat{z} \qquad 3.\,28$$

Eq. 3. 26 and 3. 28 are combined, and Eq. 3. 26 is denoted by Electric field for x, y, z directions in matrix form.

$$\begin{pmatrix} (1-\eta^2\cos^2\theta) & 0 & \eta^2\sin\theta\cos\theta \\ 0 & (1-\eta^2) & 0 \\ \eta^2\sin\theta\cos\theta & 0 & (1-\eta^2\sin^2\theta) \end{pmatrix}\begin{pmatrix} E_x \\ E_y \\ E_z \end{pmatrix} = \frac{ien_0}{\epsilon_0\omega}\begin{pmatrix} u_x \\ u_y \\ u_z \end{pmatrix} \qquad 3.\,29$$

The index of refraction by the medium are denoted as $\eta = c/v_{ph} = kc/\omega$. In same method, Eq. 3.10 are denoted in matrix.

$$\begin{pmatrix} 1+i\frac{\nu}{\omega} & i\frac{eB}{m\omega} & 0 \\ -i\frac{eB}{m\omega} & 1+i\frac{\nu}{\omega} & 0 \\ 0 & 0 & 1+i\frac{\nu}{\omega} \end{pmatrix}\begin{pmatrix} u_x \\ u_y \\ u_z \end{pmatrix} = -\frac{ie}{m\omega}\begin{pmatrix} E_x \\ E_y \\ E_z \end{pmatrix} \qquad 3.\,30$$

By inverting the matrix 3.13, the velocity space is described. Introducing here the notations are $U = 1 + i\frac{\nu}{\omega},\ Y = \frac{\Omega_{ce}}{\omega}$.

$$\begin{pmatrix} u_x \\ u_y \\ u_z \end{pmatrix} = -\frac{ie}{m\omega U(U^2-Y^2)}\begin{pmatrix} U^2 & -iUY & 0 \\ iUY & U^2 & 0 \\ 0 & 0 & U^2-Y^2 \end{pmatrix}\begin{pmatrix} E_x \\ E_y \\ E_z \end{pmatrix} \qquad 3.\,31$$

Eq. 3.12 and 3.14 are combined and described with notations $\omega_{pe} = \sqrt{\frac{n_0 e^2}{\epsilon_0 m}}$, $X = \frac{\omega_{pe}^2}{\omega^2}$, $S = 1 - \frac{XU}{U^2 - Y^2}$, $D = -\frac{XY}{U^2 - Y^2}$, $P = 1 - \frac{X}{U}$.

$$\begin{pmatrix} (S - \eta^2 \cos^2\theta) & -iD & \eta^2 \sin\theta \cos\theta \\ iD & (S - \eta^2) & 0 \\ \eta^2 \sin\theta \cos\theta & 0 & (P - \eta^2 \sin^2\theta) \end{pmatrix} \begin{pmatrix} E_x \\ E_y \\ E_z \end{pmatrix} = 0 \qquad 3.32$$

This condition gives the dispersion relation with notations $R = S + D$, $L = S - D$.

$$(S \sin^2\theta + P \cos^2\theta)\eta^4 - [RL \sin^2\theta + SP(1 + \cos^2\theta)]\eta^2 + PRL = 0 \qquad 3.33$$

Since Eq. 3.16 is a quadratic equation in η^2, general two solutions will be given as

$$\eta^2 = \frac{B \pm \sqrt{B^2 - 4AC}}{2A} \qquad 3.34$$

where,

$$A = (S \sin^2\theta + P \cos^2\theta)$$
$$B = RL \sin^2\theta + SP(1 + \cos^2\theta)$$
$$C = PRL$$

Thus, at each frequency there can be two types of waves that propagate or two modes of propagation. The mode having fast phase velocity is called as fast wave and the mode having slow phase velocity is called as slow wave. In this study, the ray-tracing code RT-4 was used to simulate the ray-trajectory to satisfy the above dispersion relation.

We simply consider two solutions of the dispersion relationship for wave propagation in the direction perpendicular to the magneto static field as $\theta = \pi/2$. Thus, dispersion relations are

$$\eta_O^2 = P$$
$$\eta_X^2 = \frac{RL}{S} \qquad 3.35$$

The index O means ordinary mode (O-mode). The index X means extraordinary mode (X-mode). The O-mode is also commonly called a transverse electric magnetic (TEM) mode. The electric and magnetic field are transverse to the direction of propagation. When $\eta = 0$ because phase velocity is infinity, the wave cannot propagate and reflects. In case of O-mode in collision less, the dispersion relation $\eta_O^2 = 1 - \frac{\omega_{pe}^2}{\omega^2}$ shows cutoff frequency as $\omega = \omega_{pe}$. The O-mode propagates without the influence of magnetic field, however, the X-mode depends on the magnetic field. The X-mode is also commonly called a transverse magnetic (TM) mode. The wave electric field has in general longitudinal component along k and a transverse component. The dispersion relation of X-mode in collision less is written as

$$\eta_X^2 = \frac{(\omega^2 + \omega\Omega_{ce} - \omega_{pe}^2)(\omega^2 - \omega\Omega_{ce} - \omega_{pe}^2)}{\omega^2(\omega^2 - \Omega_{ce}^2 - \omega_{pe}^2)} \quad 3.36$$

The left- and right-hand cutoff frequency ω_L and ω_R and resonance frequency ω_{UH} as $\eta = \infty$ are given as

$$\omega_L = \frac{1}{2}\left[-\Omega_{ce} + \sqrt{\Omega_{ce}^2 + 4\omega_{pe}^2}\right] \quad 3.37$$

$$\omega_R = \frac{1}{2}\left[\Omega_{ce} + \sqrt{\Omega_{ce}^2 + 4\omega_{pe}^2}\right]$$

$$\omega_{UH} = \sqrt{\Omega_{ce}^2 + \omega_{pe}^2}$$

The resonance frequency is called the upper hybrid (UH) frequency. The special region resonant with UH frequency is upper hybrid resonance (UHR) layer. The dispersion relation indicates phase velocity for the propagatable frequency.

In the case of 8.2 GHz injection, the schematic plots indicating cut-off density and the resonant magnetic field is shown in Figure 3.4. The plasma density of 8.2 GHz which is O-mode cut-off density of 8.2 GHz is on 8.3×10^{17} m^{-3}. In case of ECRH by 8.2 GHz LFS injection, the plasma over the O-mode cut-off density cannot be heated. In contrast, in case of the HFS injection, the wave propagates until achieving the left-hand cut-off density.

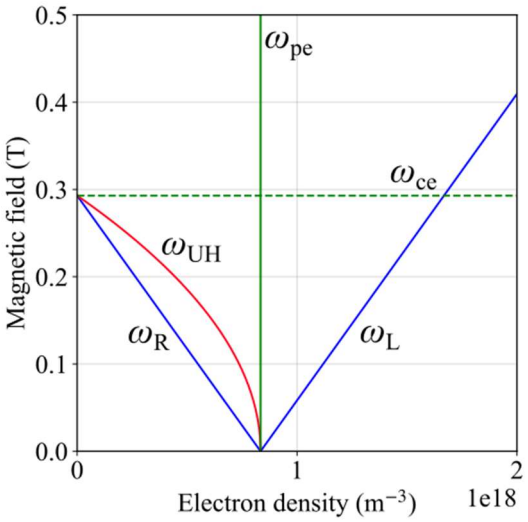

Figure 3.2 The cut-off layers and the upper hybrid ECR layer of 8.2 GHz on electron density and the magnetic field.

3.2.2 Resonance condition

The resonance condition with ECW is given by real space and velocity space [29].

$$\omega - k_{\parallel} v_{\parallel} - \frac{n\Omega_{ce}}{\Upsilon} = 0 \tag{3.38}$$

The wave with frequency ω can interact only with electrons having parallel and perpendicular velocity $(v_{\parallel}, v_{\perp})$ for the magnetic field to satisfy the indicated relation. This relationship is written by classical mechanism. $k_{\parallel}$ is parallel wave number depending on injection angle, because $k_{\parallel}$ is a function of index of refraction $\eta_{\parallel}$ as $k_{\parallel} = \omega\eta_{\parallel}/c$ and $\eta_{\parallel}$ is a function of injection angle as $\eta_{\parallel} = \cos\theta$. n is the higher harmonic numbers. Υ is relativistic factor as

$$\Upsilon = 1/\sqrt{1 - \frac{v_{\parallel}^2 + v_{\perp}^2}{c^2}} \tag{3.39}$$

In case of perpendicular injection, the resonance condition for each magnetic field is shown in Figure 3.5 **エラー! 参照元が見つかりません。**. The magnetic field is indicated as the ratio of Ω_{ce}/ω. The resonance conditions are appeared on higher magnetic field than cold ECR layer ($\Omega_{ce}/\omega = 0$). The electron particle having high energy can resonant with electron in near cold ECR layer. The effect as known Doppler shift effect $k_{\parallel} v_{\parallel}$ is not appeared. The interaction between wave and plasma is in the region as $\omega > n\Omega_{ce}$ as known the name of up-shifted absorption. In case of oblique injection of 28 GHz X-mode second harmonic ECW , the Doppler shift effect is appeared as

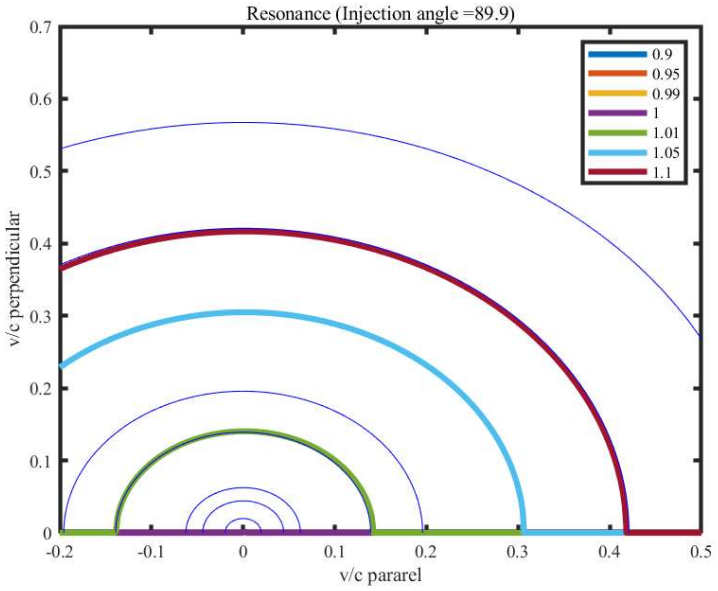

Figure 3.5 The resonance condition for each magnetic field ($\boldsymbol{\Omega_{ce}/\omega}$=[0.9, 0.95, 0.99, 1, 1.01, 1.05, 1.1]) with injection angle 89 degree. The wave frequency is 8.2 GHz. The blue lines show particle energy (100 eV, 500 eV, 1 keV, 5 keV, 10 keV, 50 keV, 100 keV).

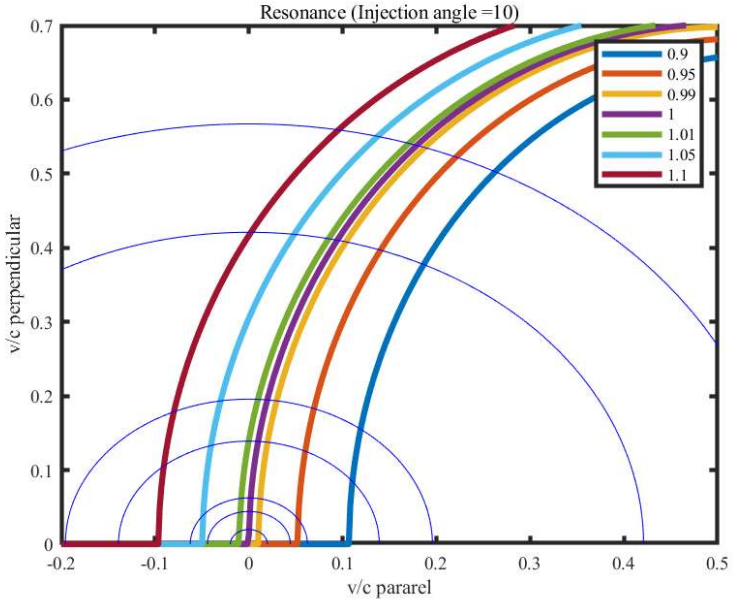

Figure 3.6 The resonance condition for each magnetic field ($\boldsymbol{\Omega_{ce}/\omega}$=[0.9, 0.95, 0.99, 1, 1.01, 1.05, 1.1]) with injection angle 10 degree. The wave frequency is 8.2 GHz. The blue lines show particle energy (100 eV, 500 eV, 1 keV, 5 keV, 10 keV, 50 keV, 100 keV).

shown in Figure 3.6. The Doppler shift causes the asymmetry of coupling region for electron velocity space. The oblique injection is completely different from the perpendicular injection that the resonant ellipses are not symmetric in velocity space. In the oblique injection, the higher electrons start to absorb waves on the ray-trajectory. This asymmetric resonant ellipse and the property to resonant to higher energy in case of high temperature cause effective current drive.

3.2.3 Ohkawa and Fisch-Boozer current drive

ECCD has the potential to drive current locally around ECR layer, so it is useful for NTM stabilization, and depression of pressure driven current as Bootstrap current in case of stellarators. ECCD mechanism was explained by Ohkawa and by Fisch and Boozer [30]. Fisch and Boozer considers the perpendicular acceleration in the velocity of a group of electrons with positive $v_{\parallel}$ which is called Fisch-Boozer current [31].

The acceleration to perpendicular direction rises up electrons to the energy regions which less collision. The collisional relaxation process symmetrizes the energy by giving the high energy for the perpendicular motion to low energy for parallel motion. As shown in Figure 3.7 (a) and (c), the acceleration of electrons occurs in positive velocity space in case of positive $\eta_{\parallel}$ determined by injection angle, so the driven current is negative direction for toroidal.

The current efficiency of Fisch-Boozer current was simply described as

$$J = -e\left(\frac{v_{\parallel 1}/\nu_1 - v_{\parallel 2}/\nu_2}{E_1 - E_2}\right)P_d \qquad 3.40$$

Subscripted 1 shows before lose energy and subscripted 2 shows after lose energy. $v_\parallel$ is velocity for parallel direction with magnetic field which resonant with wave. ν is collisional rate. E is electron's energy. P_d is the absorbed RF power. The current drive around cold ECR layer is driven locally by resonated electrons. Ohkawa found other current drive mechanism which is called Ohkawa current [7, 8]. Ohkawa current is important in the case of a toroidal plasma having a large trapped region in velocity space. If EC induced to move electrons from the passing region to the trapped region, the asymmetry of electron distribution for velocity space occurs. This asymmetry makes the current. In steady-state the electron collisional flux out of the trapped region and EC-induced electron flux into the trapped region are balanced. However, the de-trapping process is symmetric, so the asymmetry is maintained. The total electron energy in negative electron velocity space exceeds the total electron

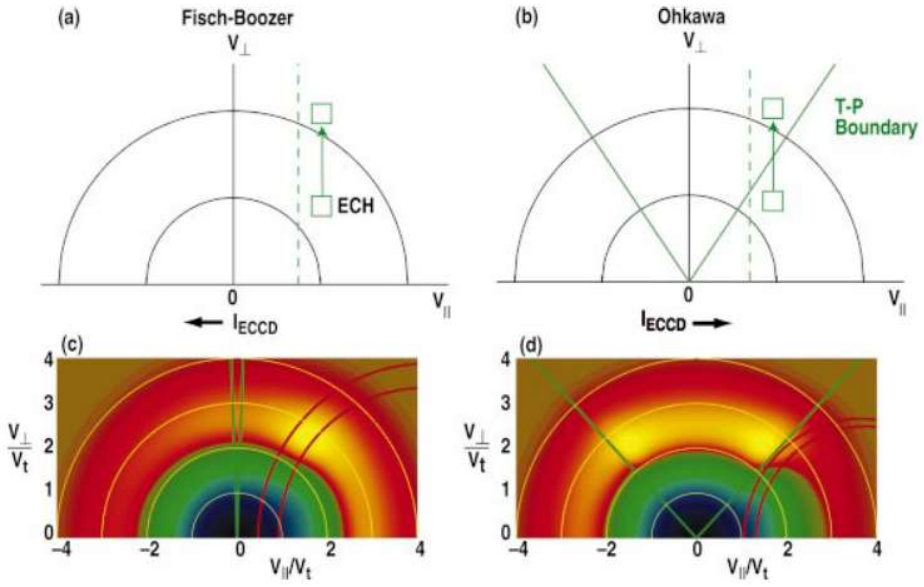

Figure 3.7 (a) Schematic illustration in velocity space of electron cyclotron current drive by the Fisch–Boozer process in a linear geometry and (b) by the Ohkawa process in a toroidal geometry. Using the CQL3D Fokker–Planck code which will be discussed later, (c) net changes in the electron distribution function for a wave/particle interaction on the high field side of a tokamak where trapping is minimal to illustrate the effects of the Fisch–Boozer process, and (d) same for a wave/particle interaction on the low field side to illustrate the Ohkawa process. The cool colors represent a decrease in the distribution function and the warm colors represent an increase. The normalized minor radius is 0.75, and $\boldsymbol{\eta}_\parallel$ is chosen to maximize the magnitude of driven current in both cases [for (c) $\boldsymbol{\eta}_\parallel$ =0.28 and for (d) $\boldsymbol{\eta}_\parallel$ =0.24]. Copied from [30].

energy in positive electron velocity as shown in Figure 3.7 (b) and (d). As the result, the current is generated opposite direction with Fisch-Boozer current direction. In case of small trapped region, the energetic electron does not drive current by Ohkawa current because the region satisfied the resonance condition are far from the trapped region. In this study, the current drive by the energetic electron was assumed by the Fisch-Boozer current because the passing region should be wide as Figure 3.7 (c).

3.3 Electron Bernstein heating

3.3.1 Electron Bernstein wave

ECW is a kind of electromagnetic wave. EBW is a kind of electrostatic wave. EBW does not have such cut-off frequency and can propagate in high density plasma due to electrostatic wave. In 1958, EBW was first studied by Ira B. Bernstein theoretically [34]. In 1964, it was observed experimentally [35]. To discuss about EBW, the hot dispersion relation should be discussed. In hot dispersion relation, the finite Larmor radius effects is needed, because the refractive index becomes infinite in case of the cold plasma approximation. The finite Larmor parameter is given $\mu = \frac{1}{2}k_{\perp}^2 v_{th}^2 \Big/ \Omega_{ce}^2$. In here, the Maxwellian velocity distribution function is assumed and relativistic effect is neglected. Finally dielectric tensor of hot plasma can be expressed [36] as

$$\epsilon = 1 + \frac{\omega_p^2}{\omega^2}\zeta_0 \sum_{n=-\infty}^{\infty} \begin{bmatrix} \frac{n^2}{\mu}\tilde{I}_n Z_n & in\tilde{I}_n' Z_n & -n\sqrt{\frac{2}{\mu}}\tilde{I}_n(1+\zeta_n Z_n) \\ -in\tilde{I}_n' Z_n & \left(\frac{n^2}{\mu}\tilde{I}_n - 2\mu\tilde{I}_n'\right)Z_n & i\sqrt{2\mu}\tilde{I}_n'(1+\zeta_n Z_n) \\ -n\sqrt{\frac{2}{\mu}}\tilde{I}_n(1+\zeta_n Z_n) & -i\sqrt{2\mu}\tilde{I}_n'(1+\zeta_n Z_n) & 2\zeta_n\tilde{I}_n(1+\zeta_n Z_n) \end{bmatrix} \quad 3.41$$

The abbreviation $Z_n = Z(\xi_n)$ shows the plasma dispersion function on the n-th cyclotron harmonic resonance by $\xi_n = (\omega + n\Omega_{ce})/(|k_{\parallel}|v_{th}^2)$.

$$Z(\zeta_j) = \frac{1}{\sqrt{n}}\int_{-\infty}^{\infty}\frac{e^{-s^2}}{s-\zeta_j}ds \quad 3.42$$

The abbreviation $\tilde{I}_n = e^{-\mu}I_n(\mu)$, I_n is the n-th order modified Bessel function. This hot dielectric tensor is expressed by not only Ω_{ce} and ω_p, but also temperature and the wave vector. The hot dielectric tensor leads to a new kind of solutions for the dispersion relation, the electrostatic modes. The electrostatic wave is restricted to perpendicular propagation for magnetic field ($\eta_{\parallel}$=0) at UHR layer. The sum over the Bessel functions gives a lot of possible roots for η. One of roots is X-mode ECW and another of roots is the EB mode. For the approximation of large Larmor effect, two modes decouple and an analytical formula for the EBW dispersion relation can be found. The EBW dispersion

relation [37] is written with the approximation $Z_n \cong -(1/\zeta_n)$ as

$$\mu = \frac{\omega_p^2}{\omega^2} \sum_{n=-\infty}^{\infty} \frac{n^2 \widetilde{I_n}(\mu)}{1 + n(\Omega_{ce}/\omega)} \qquad 3.43$$

EBW are characterized by wavelength of the order of four times the electron gyro radius. Electrostatic wave causes periodic charge accumulations propagate in the *k* vector direction. Although electric field is perpendicular to magnetic field, E×B drift does not occur because the wave frequency is larger than the cyclotron frequency. Thus, average electric field will cancel during the gyro motion.

As shown in Figure 3.8, in the vicinity of every cyclotron harmonic resonance, the refractive index becomes infinite and the wave strongly cyclotron damped due to large Larmor effect.

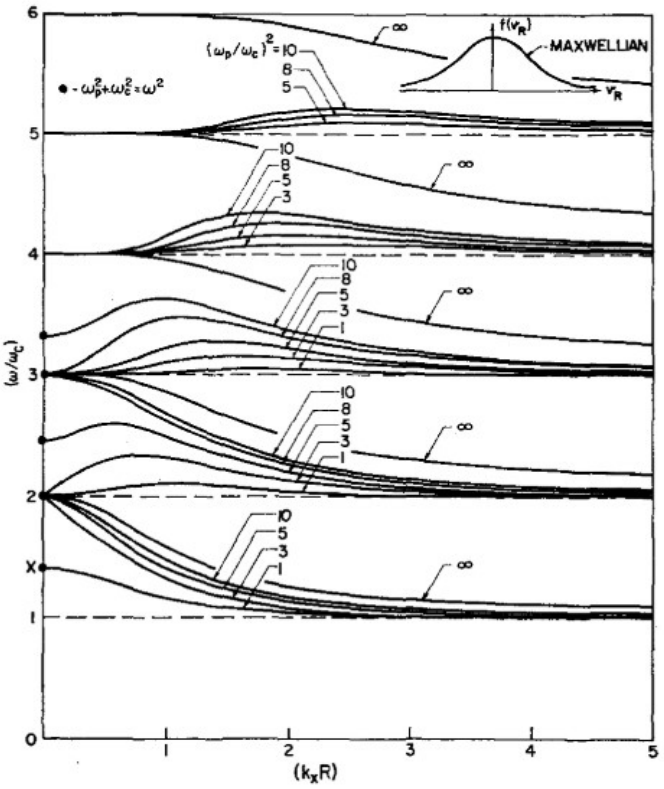

Figure 3.8 Dispersion relation of perpendicular propagation for EBW for $\boldsymbol{k_\perp \rho_e}$. Copied from [35].

However, EBW cannot be excited directly, so the mode conversion from ECW is necessary. Generally, when the X-mode ECW achieves at the upper hybrid resonance layer (UHRL), it coupled into an EB due to the corresponding with the X-mode dispersion and the EBW dispersion.

3.3.2 Mode conversion

The methods for the mode conversion to EBW are three ways. One is the X-B mode conversion by HFS injection. Other methods are the X-B mode conversion and O-X-B mode conversion by LFS injection.

X-B mode conversion by HFS injection is the simplest and highly efficient way to obtain EBW

excitation. If the density is higher than the cut-off density by left-hand cut-off, the X-mode cannot propagate, and no mode conversion occurs. Already X-B mode conversion by HFS injection has been demonstrated in some devices. In Versator II [38], McDermott et al. injected the X-mode from HFS by using the mirror reflection located on center stack. The X-mode was converted to EBW and confirmed by the observation of parametric decay instability (PDI) which will be explained latter. In LHD [39], Igami et al. demonstrated the X-mode HFS injection by utilizing the advantage of helical magnetic field. The X-mode and O-mode were injected, respectively. In only case of X-mode injection, PDI signal has been measured. Thus, the EBW excitation by X-mode HFS injection was confirmed. In MAST [40] and COMPASS-D [41], Shevchenko et al. demonstrated EBWH and EBWCD by X-B mode conversion by X-mode HFS injection. ECE intensity during EBWH was higher than ECRH [40]. The change of plasma current by injection angle showed the property of EBWCD rather than ECCD [41].

X-B mode conversion by LFS injection has been achieved in some devices. In classical mechanism, the X-mode ECW cannot propagate in plasma and no mode conversion can be expected to occur EBW due to R cut-off. In actual, the fast X-mode tunnels through the evanescent region between the R cut-off and the UHR layer and couples to the slow X-mode which, in turn, mode converts to EBW at the UHR layer. This is referred to as the X-B mode conversion process [42]. In TST-2, Shiraiwa et al. [43] demonstrated X-B mode conversion by LFS injection. In the experiment, the density gradient was enough to mode convert well. The plasma heating was observed even the plasma density achieved in cut-off density. In LATE, Uchida et al. [44]. observed the over dense plasma which is 7 times of plasma cutoff density. Direct X-mode mode conversion by LFS injection is achieved by the fine adjustment of L_n.

O-X-B mode conversion by LFS injection is one of methods. The mode conversion from O-mode to X-mode is the key in this mode conversion method. Preinhealter et al. [45] proposed a O-X-B mode conversion. First O-wave is injected from LFS with an oblique angle or non-vanishing parallel refractive index $N_{||}$, respectively. For an optimal value $N_{||opt}$, the O-mode and the X-mode can be converted at O-mode cut-off, because both modes have the same phase and group velocities and the power is transferred perfectly. For not optimized launch, an evanescent region exists, but it is possible to mode convert by an angular window, which depends on the vacuum wavelength and the density gradient. In theoretical study, analytic formulas for the angular window were given by Preinhaelter [46], Weitzner ans Batchelor [47], Zharov, Mjolhus [48] and compared with full wave calculation by Hansen [49]. In experimental study, in the stellarator W7-AS, Laqua et al. successfully demonstrated EBWH by O-X-B mode conversion for the first time [50]. In LHD, O-X-B mode conversion was demonstrated and confirmed the highly mode conversion rate by searching mode conversion window with measuring RF reflection by Igami et al. [51]. In TCV, Mueck et al. O-X-B mode conversion was demonstrated in over-dense H-mode plasma with changing injection angle [52]. The electron heating

was observed by soft X-ray even in over-dense.

The simplest and highly efficient mode conversion method is X-B mode conversion by the HFS injection. X-B mode conversion by HFS injection is highly effective mode conversion method in theory. However, the spatial limitation of device causes the difficulty to demonstrate HFS injection. In this study, the direct X-mode HFS injection without the mirror reflection was demonstrated due to the use of the space inboard side in ST.

3.4 Parametric decay instability

The parametric decay instability (PDI) occurs by the large amplitude electric field oscillation for propagation direction [53]. The three-wave coupling process is one of the simplest examples of the PDI. If a certain electric field exceeds threshold electric field, the decay wave may lead to energy conversion to new modes and change the absorption efficiency and profiles [29]. If the energy and momentum of wave are conserved as liner coupling process [54], the three-wave coupling process can be written as

$$\omega_0 = \omega_1 + \omega_2 \qquad 3.44$$
$$\boldsymbol{k}_0 = \boldsymbol{k}_1 + \boldsymbol{k}_2$$

where ω_0 and $\boldsymbol{k}_0$ are the pump wave frequency and the wave vector, and $\omega_1, \boldsymbol{k}_1$ and $\omega_2, \boldsymbol{k}_2$ are the frequencies and wave vectors of the decay waves, respectively. In case of the X-mode ECW injection, the electromagnetic wave couples nonlinearly to electrostatic wave in nature at the UHR.

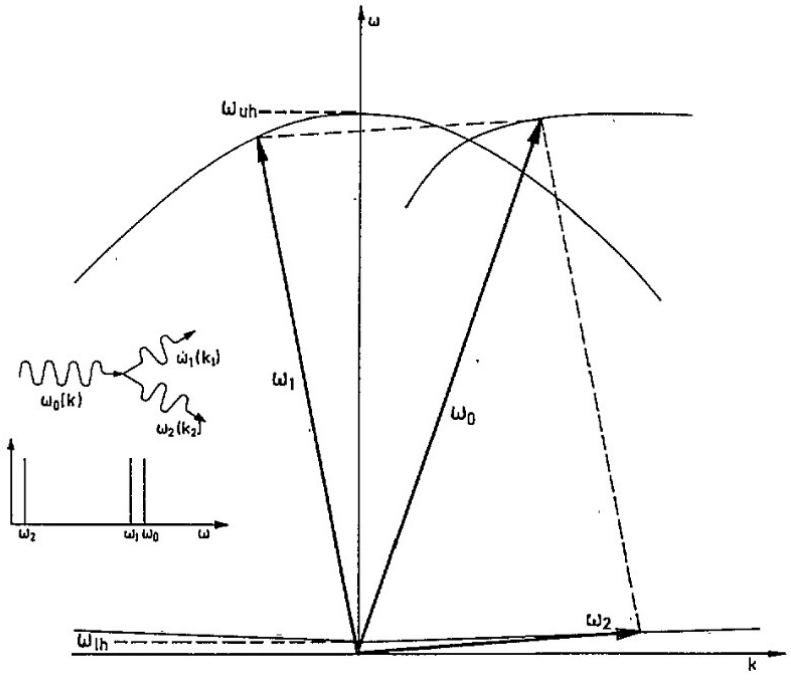

Figure 3.9 Principle sketch of ω-k to show three-wave coupling process. Copied from [29].

The clear sketch were shown in **エラー! 参照元が見つかりません。** given by Erckmann and Gasparino [29].

The predicted waves are lower hybrid mode ω_2 and electron Bernstein mode ω_1. If the tow decay waves propagate perpendicular to the toroidal magnetic field so that the parallel wavenumbers $\boldsymbol{k}_{1\parallel}$ and $\boldsymbol{k}_{2\parallel}$ are approximately equal to zero, the dispersion relations of the two modes are given [38]by

$$\omega_1^2 = \omega_{LH}^2[1 + (3b_1\omega_{ce}\omega_{ci}T_i)/(\omega_1^2 T_e)] \qquad 3.45$$

$$\omega_2^2 = \omega_{UH}^2 - \omega_{pe}^2 b_2$$

where $b_1 = k_{1\perp}^2 r_{ce}^2$, $b_2 = k_{2\perp}^2 r_{ce}^2$, and $r_{ce}^2 = (T_e/m)^{1/2}\omega_{ce}^{-1}$ is the electron gyro-radius. ω_{UH} was shown in eq. 3.20.

$$\omega_{LH} = \frac{1}{\sqrt{\frac{1}{\Omega_e\Omega_i} + \frac{1}{\omega_{pi}{}^2}}} \qquad 3.46$$

These decay waves have been observed in mode conversion in Verstor II [38], FM-1 [55] and LHD [39]. The observation of the parametric decay process may lead to collateral evidence to show mode conversion to EBW. In this study, to investigate the possibility of observing the three-wave coupling process, lower hybrid mode was measured by inserting a probe and higher hybrid mode was measured by unused antenna for injection in each case of HFS and LFS injection.

4. 28 GHz second harmonic wave electron cyclotron heating

4.1 Introduction and motivation

The second harmonic wave ECRH is attracted to apply on the large tokamak devices as ITER [56], JT-60 SA [57] as EC assistance on the low toroidal magnetic field scenario which cannot be applied the fundamental harmonic wave ECRH. In JT-60 SA, the main RF sources of 110 and 138 GHz are prepared, but in initial experimental phase and the low toroidal magnetic field scenario, the toroidal magnetic field will be 2.3 T which cannot be applied fundamental harmonic wave [57]. As sportive RF source of 82 GHz is prepared, but the injection time is restricted for short pulse. DIII-D [17] and KSTAR [58] have successfully demonstrated a start-up that combined heating with ECRH and OH. The plasma current drive by non-inductive current drive using second harmonic ECRH have been first proved in WT-3 by Tanaka *et al.* [59].

In ST, the fully non-inductive current drive by the second harmonic ECRH is more attractive than EC assistance with OH, because the center solenoid does not have the enough cross-section and to increase the limitation of plasma density. In QUEST, the fully non-inductive current drive by 28 GHz second harmonic ECRH have been demonstrated [60]. As explained in chapter 1, the 8.2 GHz fundamental ECRH is also equipped in QUEST, but the cut-off density is quite low. The merit of ST is to obtain high beta than a conventional tokamak, the achievable plasma density by 8.2 GHz cannot be high plasma density due to cutoff density. 28 GHz second harmonic ECRH has the potential to obtain a higher beta than one by 8.2 GHz fundamental ECRH. In 28 GHz second harmonic ECRH, the plasma current has been ramped up to 80 kA by 250 kW [61]. The engineering plasma current efficiency achieves to 0.32 A/W. This is mostly same with the engineering plasma current efficiency by 8.2 GHz fundamental ECRH which is obtained in inboard null configuration by Mishra *et al.* [62]. Generally, the RF absorption efficiency of the second harmonic ECW is lower than the fundamental ECW. However, it is interesting to achieve same plasma current efficiency. The mechanism of plasma heating and current drive by the second harmonic ECRH has not been cleared. In this study, I report a specific heating property of the second harmonic ECRH observed by the two different measurement systems which can measure the behavior of electrons having different electron energy as Thomson scattering measurement and the hard X-ray measurement. We explain the mechanism of the specific heating property by the numerical analysis of the considering RF absorption energy on single- and multi-pass absorption.

4.2 Experiment set-up

In QUEST, the maximum toroidal magnetic field in center of plasma is 0.25 T. The maximum toroidal magnetic field was applied. The second and third harmonic electron cyclotron resonance (ECR) layers at 28 GHz were located at R_{2nd} = 0.32 m and R_{3rd} = 0.48 m, respectively. The 28 GHz fundamental

ECR layer was located inside the CS coil and not in the vessel. The right-hand cut-off density for the 28 GHz second harmonic X-mode is $n_e \sim 4.8 \times 10^{18}$ m^{-3} (at $N_{\parallel} = 1$), which is 2 times higher than cut-off density of the 14 GHz fundamental ECW O-mode and 5.8 times higher than the cut-off density of the 8.2 GHz fundamental ECW O-mode.

8.2 GHz ECRH with a 20 kW was used at plasma initiation to improve the reproducibility of the plasma breakdown; although, only 28 GHz second harmonic ECRH could also achieve the breakdown [13]. The 28 GHz gyrotron could be supplied with up to 400 kW of power, and the associated injection system was designed the focusing mirror to increase the power density and permit variations in the injection angle [6]. The 28 GHz launcher facilitated the focusing of the plasma beam to a diameter size of $r_{beam} < 0.1$ m when the second harmonic ECR layer was employed with a low power test bench [60]. In this experiment, the injection power was 200 kW and oblique injected with 38.3° to be $N_{\parallel} = 0.78$ at second harmonic ECR layer. The measurement locations are shown in the cross-sectional top-view of QUEST in Figure 4.10. To investigate two kinds of electrons for a bulk component and a tail component of the electron having of Maxwellian distribution, Thomson scattering system and CdTe detector were equipped. The Thomson scattering system can measure the electron temperature and density of the bulk component. The Thomson scattering system was consisted of a 1064 nm Nd:YAG laser [63] with a repetition rate of 100 ms. Measurement locations were at R direction of 340, 470, 618, 770, 926, and 1082 mm. CdTe detector can assess hard X-ray (HXR) emission which is induced by the tail component of electron by pulse height analysis. The CdTe detector (CLEAR-PULSE: 5623-GCT404010) is comprised of a 4 mm × 4 mm × 1 mm CdTe module which attached to a 100 μm thick aluminum filter, which was absorbable the radiation below 20 keV. Thus, the measuring energy area was limited over 25 keV. The CdTe detector faced the second harmonic ECR layer. To make the accurate direction of X-rays through the targeted line of sight (LOS), the CdTe detector was covered by a 76 mm thick cylindrical lead shield in its side and backside and by a 125 mm thick shield in the front and a collimator with a radius of 1 mm was placed in front of the detector. As other supportive measurement system, a visible light monochromator to detect H_α radiation, an array of absolute extended ultraviolet (AXUV) detector to monitor the radiation, and a RF detector to monitor RF leakage, a medium speed visible camera were equipped on the mid-plane. The central wavelength of the visible light monochromator (Nikon: P-250) was set as 656.28 nm to facilitate an accurate detection of the H_α radiation which is a line of Balmer series of hydrogen. An AXUV detector is composed of 16 channels. AXUV has a good responsivity for wide detectable energy range from visible light to soft X-ray. The AXUV signal is nearly proportional to the radiation brightness within the soft X-ray wavelength range, with the response constant $R_{es} = 0.26$ A/W. The field of view (FOV) of each AXUV was restricted by a slit (2.3 mm × 3.3 mm). The red region in Figure 4.10 represents an overhead view of the resulting FOV. The AXUV channels was located to assess the radiation from top to bottom as shown in Figure 4.11. The center of AXUV detector was used to monitor the center

of the plasma. By calculating etendue and responsivity values, AXUV signal provided a measure of the radiation brightness (in W/m^2). The temporal resolution of the AXUV detector array was limited by the cut-off frequency of the pre-amplifier (300 kHz). The RF detector was installed out of the vacuum vessel to monitor RF leakage. It could be the monitor of RF leakage from vacuum vessel. The mid-speed visible camera can observe visible light image as mono-color with the of 8 bits intensity with 100 frames per second. The installed 64 magnetic flux were also equipped on the vessel [64].

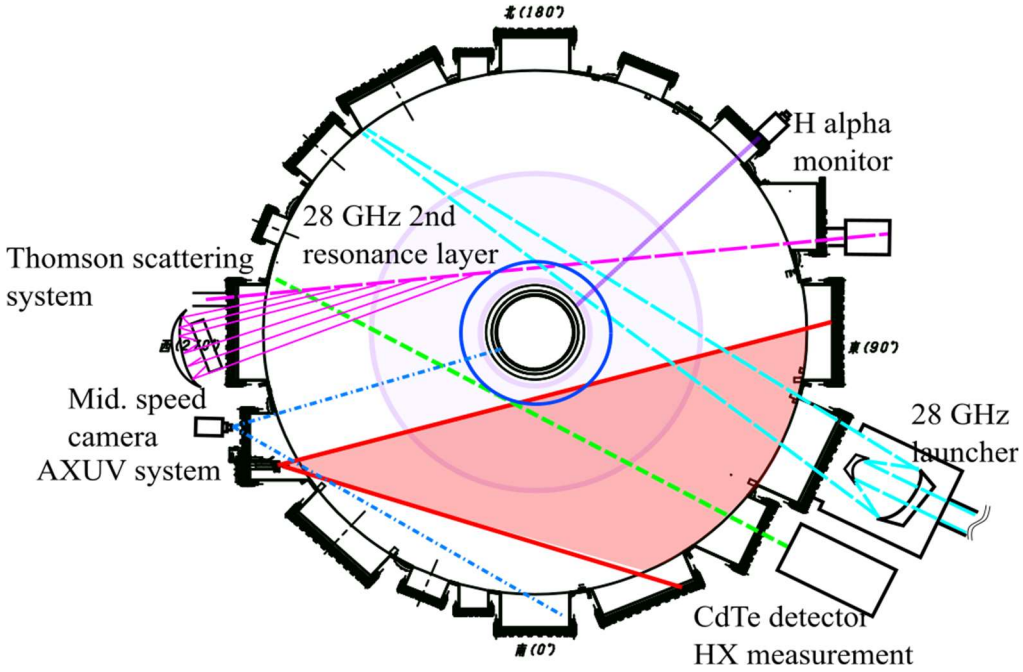

Figure 4.10. Top view of QUEST showing the locations of each measurement system. The FOV of the AXUV detector array is indicated by the region in red, while the green, purple, and orange lines show the LOSs for the CdTe, H_α, and Thomson scattering detectors (measurements were performed at R = 340, 470, 618, 770, 926, and 1082 mm). The second harmonic ECR layer and the 28 GHz ECW injected from the launcher are shown by the blue circle and cyan lines, respectively.

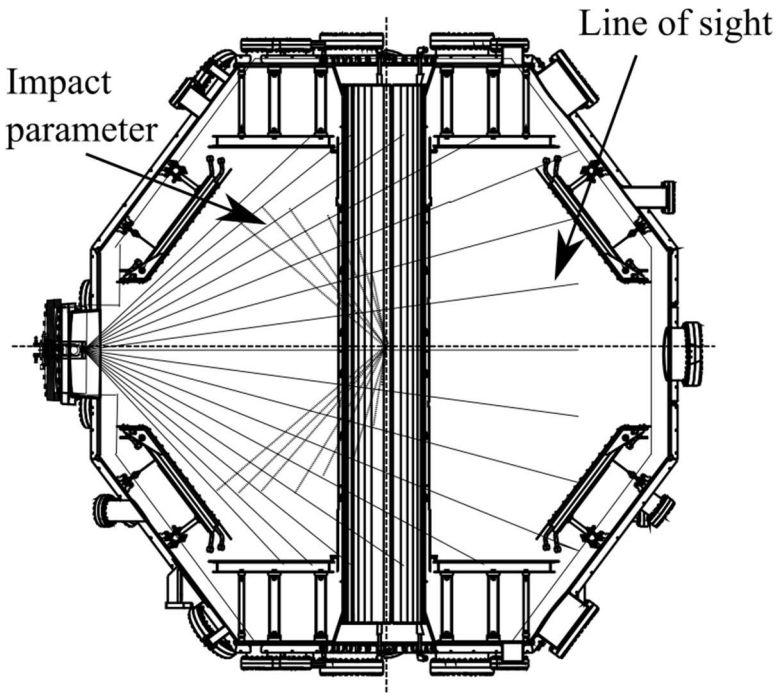

Figure 4.11. Cross-sectional view showing the LOSs of the AXUV detector array and the impact parameter on each LOS. From top to bottom, the channel numbers are from CH1 to CH16, with CH8 positioned almost exactly at the center line.

4.3 Observation of heated electron energy shift

The plasma start-up by 28 GHz second harmonic ECRH has been demonstrated successfully. The specific discharge showing the reduction of bulk electron temperature during plasma current ramp-up were often obtained. The typical observed discharge is shown in Figure 4.12. We classified the time evolution to three stages as A-C. In stage A, the I_p was 12 kA with the bulk electron temperature ~ 140 eV and no HXR emission as Figure 4.12 (b, e, f). H_α radiation was increased and the brightness of AXUV was high. The stage A is identified as RF bulk heating dominant. In stage B, the I_p was mostly not changed. The bulk electron temperature and brightness were decreased. The bulk electron temperature and brightness showed a similar trend. The time resolution of AXUV detector system is higher than Thomson scattering system. Thus, the degradation of the brightness by AXUV was affected by the bulk electron temperature. The slight HXR emission was appeared. H_α radiation was kept increasing. The stage B is characterized by electron energy shift of RF coupling. In stage C, the I_p was rapidly increased. The bulk electron temperature showed almost constant value with quite low ~ 10eV. Instead of the decrease of the bulk electron temperature, the HXR emission was increased. The brightness was slightly increased in the latter part with different trend with the bulk electron temperature. It might be influenced due to soft X-ray induced by a high energy electron generation.

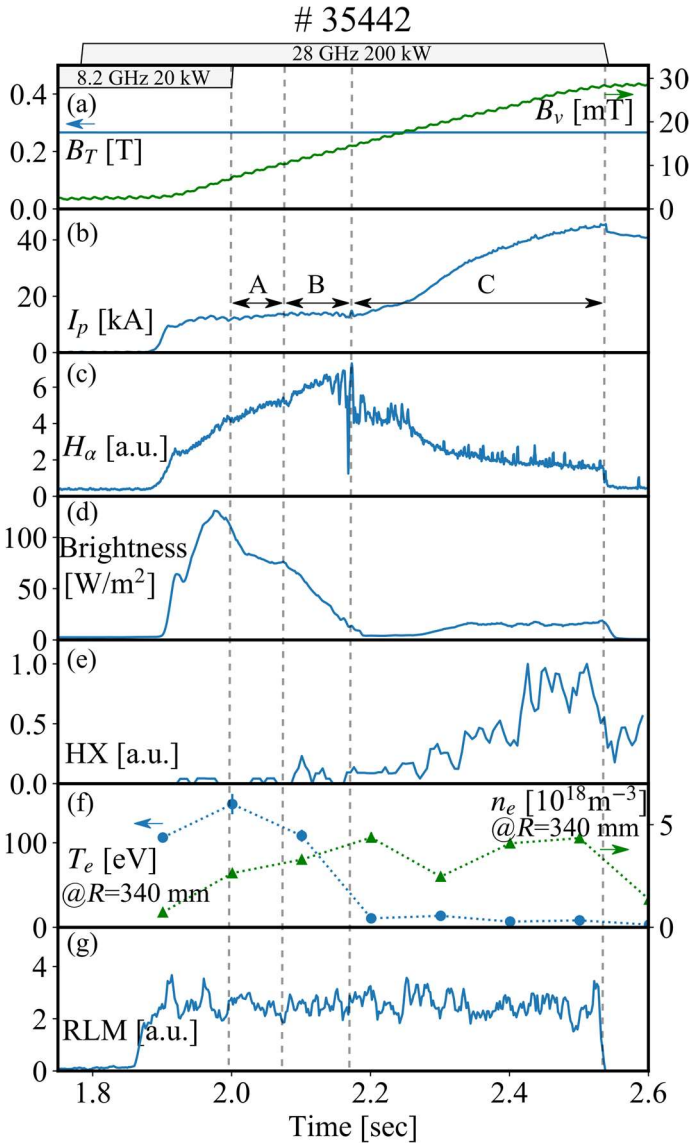

Figure 4.12. Time evolution of (a) the toroidal and poloidal magnetic field B_t and B_v, (b) the plasma current I_p, (c) H_α radiation, (d) the radiation brightness measured by AXUV, (e) Hard X-ray emission, (f) Electron temperature T_e and density n_e around ECR layer measured by Thomson scattering system. (g) RF leakage monitor signal. Each specific stage is classified as A-C with dot lines.

The stage C is identified as RF tail heating dominant and consequently I_p was quickly ramp-up.

In entire of 28 GHz RF injection, the electron density around ECR layer was almost constant. The RF leakage was the same level in the entire discharge. The bulk electron temperature and density denote the values around ECR layer in Figure 4.12 (f). The temperature and density in other locations had the similar tendency. The increase of plasma current after the decrease of the bulk electron

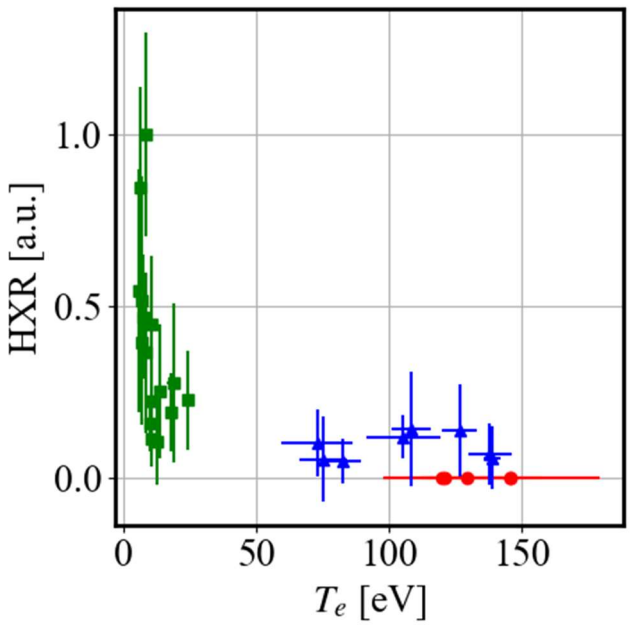

Figure 4.13. HXR intensity as a function of the bulk electron temperature T_e. Red, blue, and green circles denote the stages A, B, and C, respectively.

temperature was reproducible. This has never observed in plasma current start-up using fundamental ECRH and, in the sense, the future is discriminative in the second harmonic ECRH. Electron energy to be coupled by ECW is denoted in Figure 4.13 and a clear electron energy shift was observed. In stage A, bulk electron heating could be observed. The electron energy shift to energetic electron could be observed in stage B and finally tail electron heating was dominant in stage C. It should be noted that the electron energy shift was not caused by the X-mode cut-off density, because the shift has been commonly observed in discharges in the lower density $n_e \sim 1 \times 10^{18}$ m^{-3} that is far from X-mode cut-off density.

The electron energy shift was accompanied with the deformation of plasma configuration. The deformation was investigated with magnetic surface reconstruction using EFIT code and 2D images measured with a visible camera as shown in Figure 4.15. In the stage A, the plasma configuration was expanded and then the shape was shrinking during the stage B, and maintained the magnetic configuration in the stage C. The shrinking was caused by increment of the vertical magnetic field for constant I_p. However, it was the most reproducible operation in the experiment. The deformation was confirmed with brightness profile by AXUV as shown in Figure 4.14. The first reduction of radiation was caused by the termination of RF injection of 8.2 GHz. The brightness profile was almost constant during the stage A. Subsequently, the size of the bright region was shrinking during the stage B, and the brightness was a little bit at the beginning of the stage C. It means the electron energy shift may give a significant impact on plasma equilibrium and electron space distribution.

The EFIT code can provide the stored energy as well as plasma configuration. The time evolution of the stored energy is denoted in Figure 4.16. It should be noted that the EFIT code could not be converged around a part of the stages B and C because of the insufficient spatial resolution of magnetic

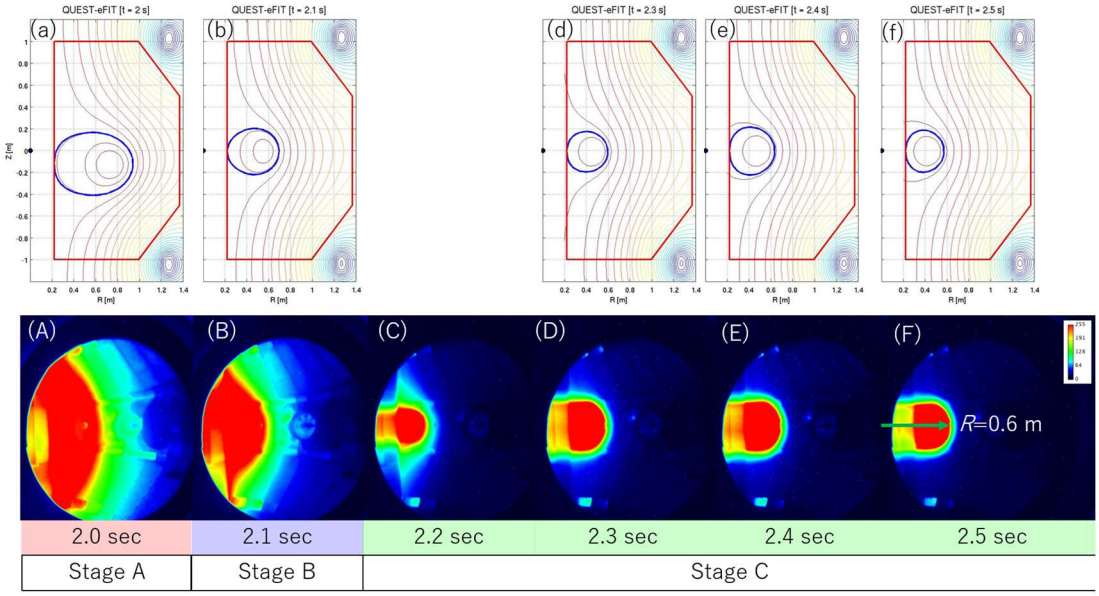

Figure 4.15. (a-f) The reconstructed magnetic flux surface at every 100 ms by using the EFIT code. (A-F): Visible light images of the right-side half at the same timing of flux surface reconstruction. The color scale indicates the visible light intensity. The progression of the stage is denoted in the bottom of the figure.

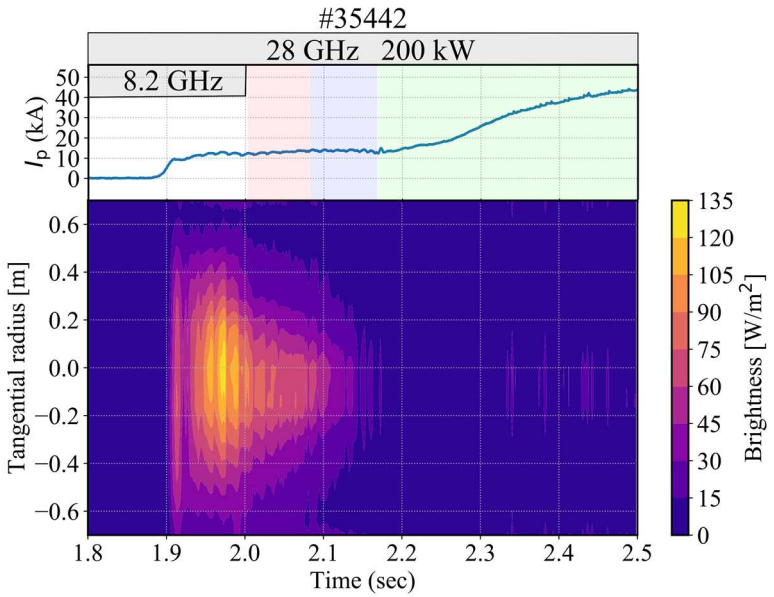

Figure 4.14. The plasma current and brightness along the impact parameter during the first ramp-up phase. Red, blue, green and pink regions indicate stages A, B and C.

measurements. The stored energy was gradually increasing in the stage A and then the sudden jump-up of the stored energy can be observed at the turning point from stage A to B as shown in Figure 4.16 (e). While the AXUV brightness started to be reduced at the timing in Figure 4.14. A little HXR radiation was also observed after the timing. It suggests that the significant number of tail electrons was produced. The electron energy shift was caused by the production of the tail electron and the process should be quantitatively discussed.

The key parameters are the stored energy and the plasma current to consider about tail electron parameters. Ray-tracing calculation is useful to estimate how much of plasma current can be driven by the RF injection, but we must assume only single-pass absorption of RF to estimate driven current because it is difficult to account how the RF is reflected on the plasma facing wall to estimate what propagation mode, polarization and angle to the magnetic field the reflected RF has. Power balance is available to estimate RF multi-pass absorption. We will combine the ray-tracing code and the power balance to quantitatively understand the electron energy shift.

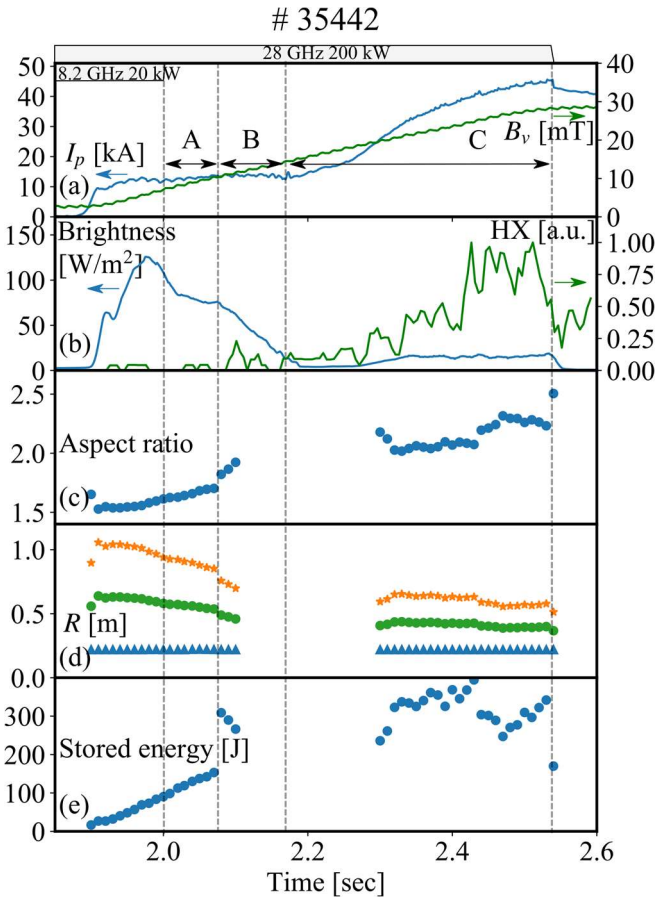

Figure 4.16. Time evolution of (a) the plasma current I_p and vertical magnetic field B_v at R = 600 mm, (b) the radiation brightness measured by AXUV and HXR intensity, (c) the aspect ratio, (d) the major radius of outer edge, axis and inner edge, (e) stored energy. The aspect ratio, radius and stored energy was calculated by EFIT.

4.4 Quantitative discussion using ray-tracing and power balance for electron energy shift

A ray-tracing analysis was executed to understand the mechanism of the electron energy shift. The used ray-tracing code RT-4 was developed in PPPL by M. Ono [65]. It can simulate power absorption and driven current by two interlaced Maxwellian electron distribution, so it can simulate the effect of the bulk and the tail electrons. To simplify the calculation of the ray-trajectory, the cold dispersion relation was solved because the dominant electron is the bulk electron which does not be influenced of the relativistic effects. The power absorption on each ray location was calculated fully kinetic harmonic absorption up to 4th harmonic Bessel function terms for Maxwellian distribution. The current drive efficiency was based on Fisch and Boozer theory [31]. The measured temperature and density distribution by Thomson scattering measurement were used for the bulk electron distribution to simulate the experiment.

The interpolated distribution by original natural logarithm was given as the bulk electron distribution for raytracing. The tail electron distribution was assumed that the formation of density distribution is of the same with the bulk electron distribution and the temperature distribution is assumed to be flat. The ray was oblique injected from R = 1.94 m with antenna rotation angle was 17° to be $N_{||}$ = 0.78 at cold second harmonic ECR layer. The ray-tracing calculation was started from outside plasma given by EFIT. The five rays to simulate the beam with diameter 0.1 m were calculated with the Gaussian power distribution which was indicated the low power test bench [60].

As the example of the ray-tracing calculation, the ray-tracing was calculated with the tail electron temperature 20 keV and the tail electron density with 5% of the bulk electron density and the bulk

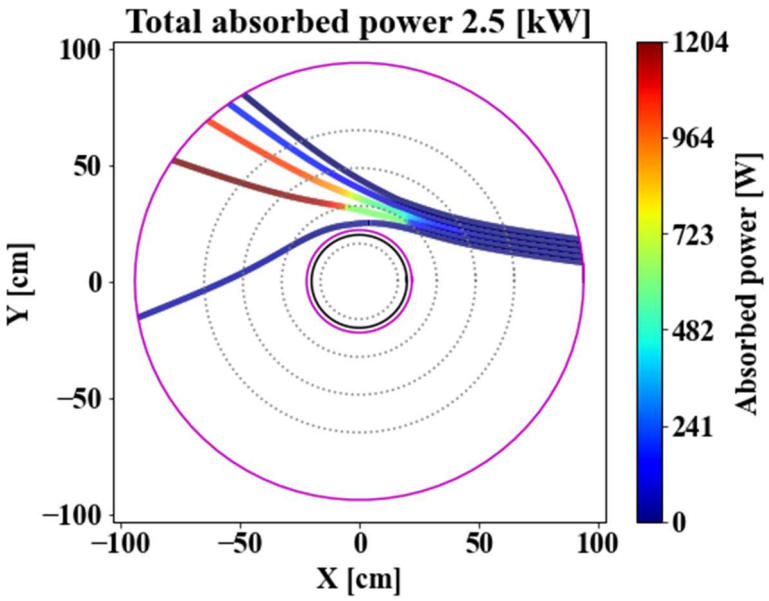

Figure 4.17. The absorbed power on each ray. The pink line shows the plasma boundary. The dot lines show the resonance layers from fundamental to forth harmonic.

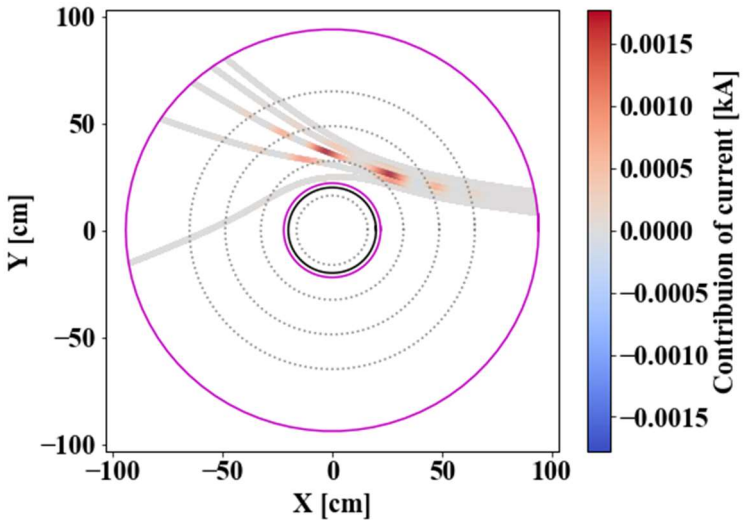

Figure 4.18. The contribution for plasma current on each ray. The pink line shows the plasma boundary. The dot lines show the resonance layers from fundamental to forth harmonic. The color bar shows the contribution of driven current.

electron temperature and density at t = 2.0 s in X-mode 200 kW injection. The single-pass absorption was shown in Figure 4.17. Mainly the RF power are absorbed in second harmonic ECR layer. The total RF single-pass absorption was quite low as 1.2 % of the injection power in this case. The RF power was absorbed from LFS of cold ECR layer due to Doppler shift effect. The contribution for driven current was shown in Figure 4.18. By taking Doppler shift effect into consideration the electron coming toward the ray ($k_{||}\boldsymbol{v}_{||} < 0$) can be resonated in the LFS of ECR layer, the electron going away from the ray ($k_{||}\boldsymbol{v}_{||} > 0$) can be resonated in the HFS of ECR layer. The RF absorption on lower harmonic ECR layer is higher efficiency than the higher harmonic ECR layer. In case of the crossing the lower harmonic ECR layer and higher harmonic ECR layer. The electron coming toward the ray ($k_{||}\boldsymbol{v}_{||} < 0$) has higher RF absorption and higher current drive efficiency in the LFS injection. The tail electron has large parallel velocity $\boldsymbol{v}_{||}$ and the large contribution to drive the plasma current in the case of oblique injection ($k_{||} \neq 0$) can be expected in the LFS of each cold ECR layer due to the Doppler shift effect.

The key parameters, the stored energy and the plasma current applied to estimate the tail electron density and temperature. These parameters are expressed by the following Eqs.4. 47 and 4. 48.

$$I_{ECCD}\left(T_{e\,bulk,}n_{e\,bulk,}T_{e\,tail,}n_{e\,tail}\right) = I_p - I_{BS} \qquad 4.\ 47$$

$$W_{cal}\left(T_{e\,bulk,}n_{e\,bulk,}T_{e\,tail,}n_{e\,tail}\right) = W_{EFIT}$$

$$W_{cal}\left(T_{e\,bulk,}n_{e\,bulk,}T_{e\,tail,}n_{e\,tail}\right) = \frac{3}{2}\left(\overline{n_{e\,bulk}}\,\overline{T_{e\,bulk}} + \overline{n_{e\,tail}}\,\overline{T_{e\,tail}} + \overline{n_i}\,\overline{T_i}\right)V \qquad 4.\ 48$$

where I_{ECCD} is the driven current calculated by RT-4 ray-tracing, given $T_{e\,bulk}$ denotes the bulk electron temperature, $n_{e\,bulk}$ is the bulk density, $T_{e\,tail}$ is the tail electron temperature, and $n_{e\,tail}$

is the tail density. I_p is the plasma current, and I_{BS} denotes the bootstrap current estimated by the scaling given by Forest et al.[66], W_{cal} is the calculated value of the stored energy for the given bulk and tail electron parameters, and W_{EFIT} is the stored energy given by the EFIT code, here, $\overline{n_{e\,bulk}}, \overline{T_{e\,bulk}}$ are averaged bulk electron density and bulk temperature on volume, $\overline{n_{e\,tail}}, \overline{T_{e\,tail}}$ are averaged tail electron density and tail temperature on volume, $\overline{n_i}, \overline{T_i}$ are averaged hydrogen ion density and ion temperature on volume, V is the plasma volume. We have two equations to decide two parameters, $n_{e\,bulk}$ and $T_{e\,tail}$. The ion density distribution assumed the charge neutrality. The average ion temperature was assumed to be flat with 5 eV that was typically obtained by spectroscopy of C_{III} line.

An example of the solution of the Eq. 4. 48 can be illustrated in Figure 4.19. The cross point of the curves is the solution. In the calculation, the error in the stored energy by EFIT code is taken into consideration, because the separation of the average poloidal beta β_p and half internal inductance $l_i/2$ is the difficult, because of low delta. The error value was assumed to be 10 %.

The time evolution of tail electron temperature and density as solutions of the Eq. 4. 47 are shown in Figure 4.20. In the bulk electron heating phase at t = 2.0 s, the tail electron density was quite small ~

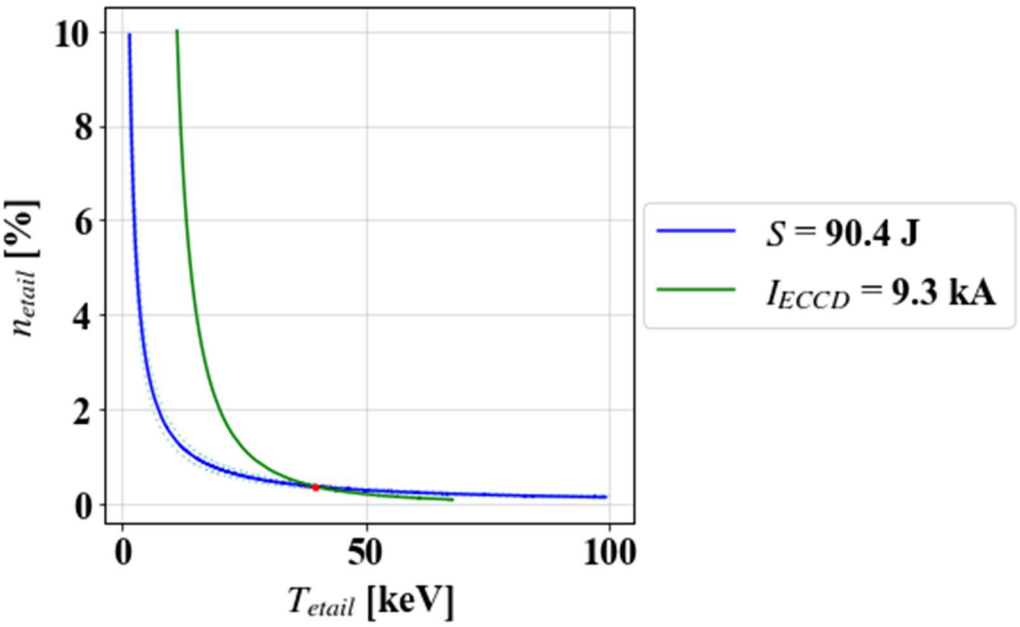

Figure 4.19. The experimentally satisfying lines of the drive current and the stored energy. The cross point shows the estimable tail electron temperature and density. A green line shows the driven current. A blue line shows the stored energy.

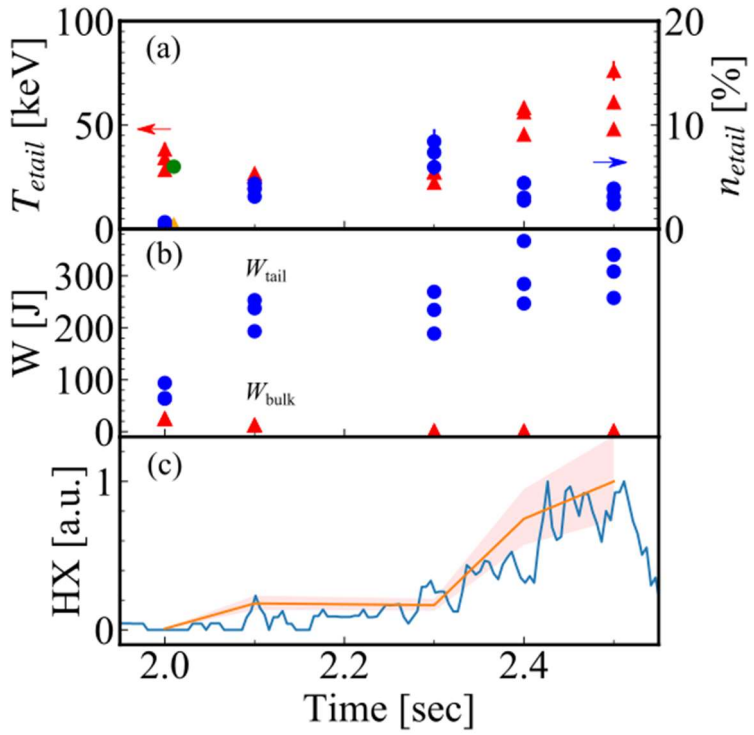

Figure 4.20. The time evolution of (a) estimated tail electron temperatures and density rates for the bulk electron density, (b) stored energy of bulk electron and tail electron and (c) normalized the measured hard X-ray intensity and estimated bremsstrahlung by estimated tail electron temperatures and density rates. On #35440, #35441, #35442. Orange triangle and green circle points show the estimated tail electron temperatures and density rates for the bulk electron density, 2 keV and 6 % of bulk density, which satisfy the stored energy and the power balance assuming multi-pass absorption, respectively.

0.4 % of the bulk electron density.The tail electron temperature was estimated to be ~ 30 keV, because the stored energies of tail electrons are large which is comparable with bulk electrons. Generally, RF absorption is rather poor in the start-up phase because of low electron temperature and density. Thus, multi-pass absorption should be considered in the start-up phase. The multi-pass absorption process will be discussed latter. The tail electron density increases from the transition phase at t = 2.1 s, and the stored energy of the tail electron becomes dominant. The tail electron density reaches several percent of the bulk electron density through effective tail electron heating. Finally, the tail electron temperature and density became 60 keV and 3 % of bulk electron density.

The accuracy of the tail electron parameters was evaluated by the comparison of normalized HXR emission measurement and the estimated bremsstrahlung [see Appendix II] as shown in Figure 4.20 (c). The both were shown as a function of the plasma current in Figure 4.21. It is well known that the HXR is radiated through bremsstrahlung. We assumed a relativistic Maxwellian distribution with

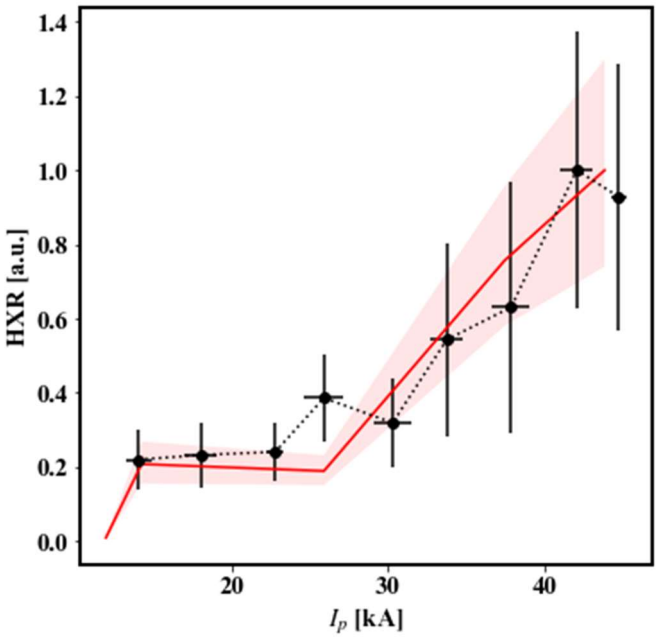

Figure 4.21. HXR intensity as a function of the plasma current on #35442. The circles show the average HXR intensity with the corresponding standard deviation indicated by error bars. The red line indicates the evaluated detectable hard X-ray intensity by the bremsstrahlung estimation.

$T_{e\,tail}$ and $n_{e\,tail}$ to estimate the bremsstrahlung intensity. The CdTe detector is sensitive to the HXR in the range of 25 keV – few hundred keV and the intensity calculation is taking the sensitivity of 25 – 400 keV into consideration. The accuracy of evaluated tail electron temperature and density was confirmed by the consistency of measured HXR emission and the estimated bremsstrahlung for the plasma current. This observation can support the RF induced plasma current is driven by the RF generated tail electrons. This tail electron generation is same with the plasma current start-up by rich tail electrons using fundamental ECRH [67].

The calculated RF single-pass absorption rate for the total RF single-pass absorption is shown in Figure 4.23. After enhancement of the tail electron temperature and density, the RF single-pass absorption rate for the tail electron is dominant and causes the tail electron heating. In tail electron heating, the almost RF power were absorbed in the tail electron. The only RF absorption rate for the tail-bulk electron cannot decide the criteria for the electron energy shift occurrence because the bulk electron heating is given by not only RF absorption but also the energy exchange by tail-bulk electron collision. In order to consider about the criteria for the electron energy shift, the power balance for input power and out power have to be calculated as assuming multi-pass absorption process.

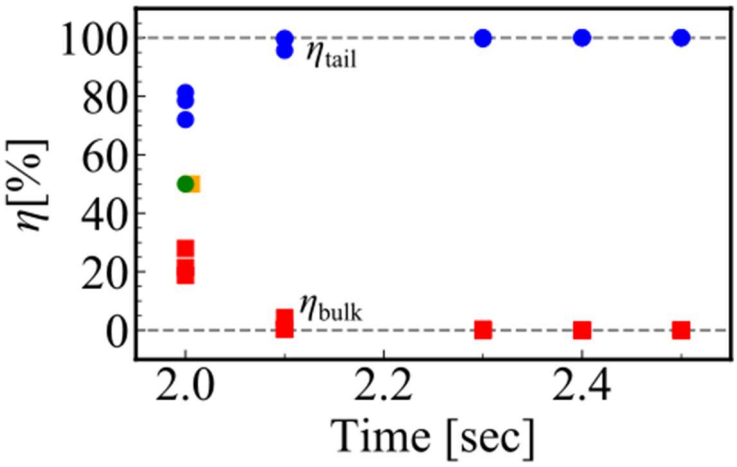

Figure 4.23. The absorption rates of tail and bulk electron for the total single pass absorption. On #35440, 35441, 35442. Orange square and green circle points show the absorption rates of bulk and tail electron for the total single pass absorption, 2 keV and 6 % of bulk density, which satisfy the stored energy and the power balance assuming multi-pass absorption.

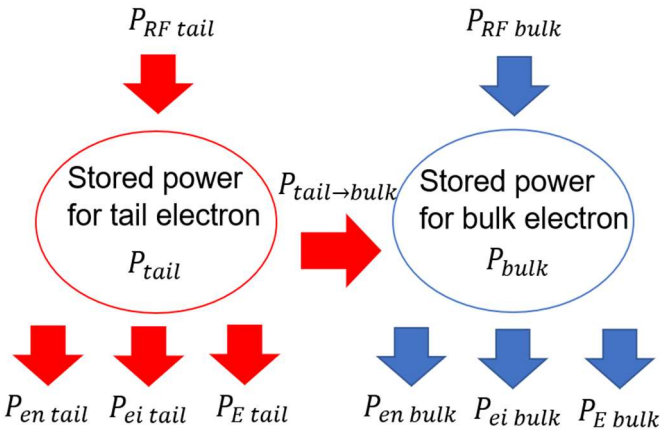

Figure 4.22. The schematic image of power balance of the bulk electron and the tail electron.

The power balances for the tail and bulk electrons were calculated to estimate the total absorbed power. The input power and the output power have to be balanced in each component. For the tail electron, the input power is the absorbed RF power, $P_{RF\,tail}$ only. The output power as the power loss is brought from the collision between bulk electrons, $P_{tail\rightarrow bulk}$, ions, P_{eitail} and neutral particles, P_{entail} and some radiation and transport, $P_{E\,tail}$. For the bulk electron, the input power is the absorbed RF power, $P_{RF\,bulk}$ and the energy exchange between tail-bulk electron through the Coulomb collision, $P_{tail\rightarrow bulk}$. The output power as the power loss is caused by the collision between ions, P_{eibulk} and neutral particles, P_{enbulk}, and plasma confinement including radiation, $P_{E\,bulk}$.

The power balance is expressed by as Eq. 4. 49 and the schematic drawing is also shown in Figure 4.22.

$$P_{RF\,bulk} + P_{tail\rightarrow bulk} = P_{enbulk} + P_{eibulk} + P_{E\,bulk} \qquad 4.\ 49$$
$$P_{RF\,tail} = P_{tail\rightarrow bulk} + P_{entail} + P_{eitail} + P_{E\,tail}$$

The expression of each term is described in Appendix III. The power loss $P_{E\,bulk}$ is given by the global energy confinement time scaling. The global energy confinement time was used the L-mode scaling given by Kaye, et al [68]. While there is no scaling for the confinement of tail electron. The global energy confinement time for the tail electron $P_{E\,tail}$ was postulated 10 ms based on the experimental observation in fundamental ECRH experiment on QUEST. In 8.2 GHz fundamental ECRH experiment, the tail electron power loss ~ 20 kW was measured by water cooling system [69], and the stored energy was ~ 200 J, so the confinement time should be ~ 10 ms.

The calculated power balance for the bulk and tail electron were shown in Figure 4.24. The RF power to maintain the bulk plasma from 2.3 s to 2.5 s shows the negative value. The negative value of the RF absorption means that the global energy confinement time is worse than the ITER89-P scaling because of the quite low bulk electron. However, the required power < 5 kW is maintained by the power supply by $P_{tail\rightarrow bulk}$. The almost total RF power is absorbed in tail electron. This is coincidence with the RF absorption rate assuming single-pass absorption as shown in Figure 4.23. In contrast, in the bulk heating at 2.0 s, the deposited power on bulk electron should be 40 kW due to the power balance calculation. However, the expected RF absorption rate for the power deposition to bulk electrons is just 20 % due to single-pass absorption. This discrepancy is originated by the estimation of tail electron density and temperature. This discrepancy indicates that multi-pass RF absorption works significantly at the time. The tail electron temperature and density should satisfy Eq. 4. 50 to consider the multi-pass absorption process.

$$\frac{P_{RF\,tail}\left(T_{e\,tail,}n_{e\,tail}\right)}{P_{RF\,bulk}\left(T_{e\,tail,}n_{e\,tail}\right)} \sim \frac{\eta_{tail}\left(T_{e\,tail,}n_{e\,tail}\right)}{\eta_{bulk}\left(T_{e\,tail,}n_{e\,tail}\right)} \qquad 4.\ 50$$
$$W_{cal}\left(T_{e\,bulk,}n_{e\,bulk,}T_{e\,tail,}n_{e\,tail}\right) = W_{EFIT}$$

where η_{tail}, η_{bulk} are the absorption rate for total single-pass absorption for tail and bulk electron. The single-pass absorption rate should be calculated averaged injection angle of $N_{\|}$ = 0.5. The absorption rate between tail and bulk electron on total RF absorption should be same with total single-pass RF absorption. In averaged angle of $N_{\|}$ = 0.5, the RF absorption rate satisfying the stored energy should 1:1 for tail and bulk electron. The total RF absorption rate for tail and bulk electron also be 1:1. The estimated tail electron temperature and density were 2 keV and 6 % of bulk electron density as explained in appendix IV. The calculation considering multi-pass absorption provides the tail electron of 2 keV in temperature, 6 % of bulk electron density, instead of 30 keV in temperature, 0.4 % of bulk electron density. These values are more acceptable in electron energy progress because acceleration

of electron was expected from 2.0 s to 2.1 s from 2 keV to 20 keV. The result can be supported by the analysis provided previously [65]. The total RF absorption is expected to be 25 % of the injection RF power during the start-up. It agreed with the observation of the constant RF leakage.

The multi-pass absorption also showed a higher RF absorption for the tail electron after electron energy shift. The tail electron has a higher heating efficiency by the finite Larmor radius effect than bulk electron for higher harmonic ECRH. Moreover, the increase of the tail electron temperature causes the reduction of energy exchange through tail-bulk electron collision, and the maintaining bulk electron is difficult. First, the bulk electron is cooled by the power reduction due to electron energy exchange by the increase of tail electron temperature. The RF absorption by the bulk electron decreases and the RF absorption by the tail electron increases. In result, the positive feedback loop for tail electron heating and the negative feedback loop for the bulk electron heating are constructed. This is a mechanism of the electron energy shift. On the other hand, the fundamental ECRH can heat electrons

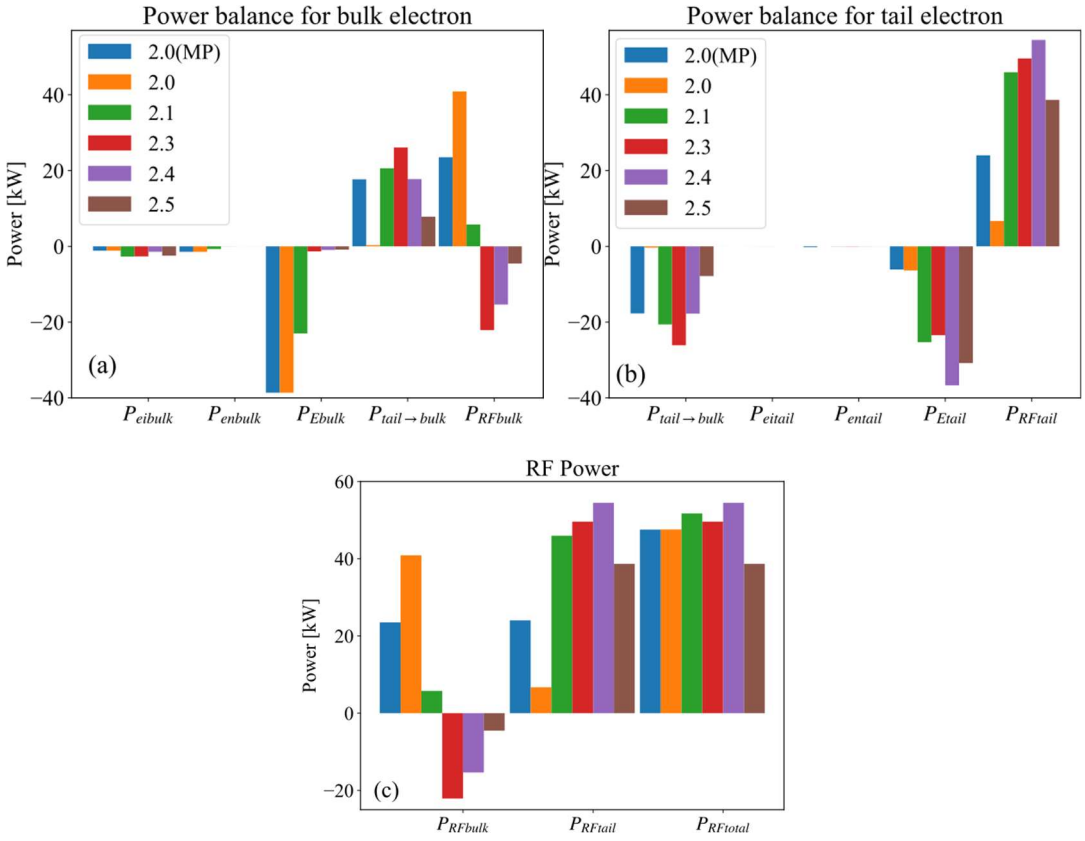

Figure 4.24. The result of power balance. (a) is the power balance of the bulk electron. (b) is the power balance of the tail electron. (c) is RF absorption power. In the label, 2.0 (MP) shows the power balance result, which satisfy the stored energy and the power balance assuming multi-pass absorption with tail electron of 2 keV, 6% of bulk electron density. The negative power means the power loss. The positive power means the power deposition.

without the finite Larmor radius effect, and the negative feedback loop for the bulk electron is difficult to occur. Thus, the electron energy shift will not be observed.

4.5 Neutral particle effect for plasma current ramp-up

Finally, we have to discuss how the plasma current ramp-up could be triggered. In the plasma current start-up experiment, the most significant result is a plasma current generation. The electron energy shift is important to develop plasma current start-up, but this is not the necessary and sufficient condition. In fact, the electron energy shift had been caused in the transition phase of stage B, but plasma current ramp-up occurred in the tail electron heating of stage C. The good correlation of HXR emission and the plasma current provides the presence and the development of tail electron heating is a key to the plasma current ramp-up. Experimentally, the neutral particle effect for the tail electron increase was observed. The plasma current was also increased with the degradation of the H_α radiation as shown in Figure 4.25. H_α radiation is regard as the hydrogen atom density in case of constant n_e and T_e. Actually, in the high plasma current $I_p > 25$ kA, n_e and T_e were almost constant. To investigate their causal correction, the start timing of the H_α radiation reduction and the I_p increase was investigated by the mutual correlation. The result is shown in Figure 4.26. The reduction of H_α radiation foregoes the plasma current ramp-up in the range of 10–60 ms. The reduction interaction between the neutral-particle and electron driving plasma current can be trigger if plasma current ramp-up. It is strongly

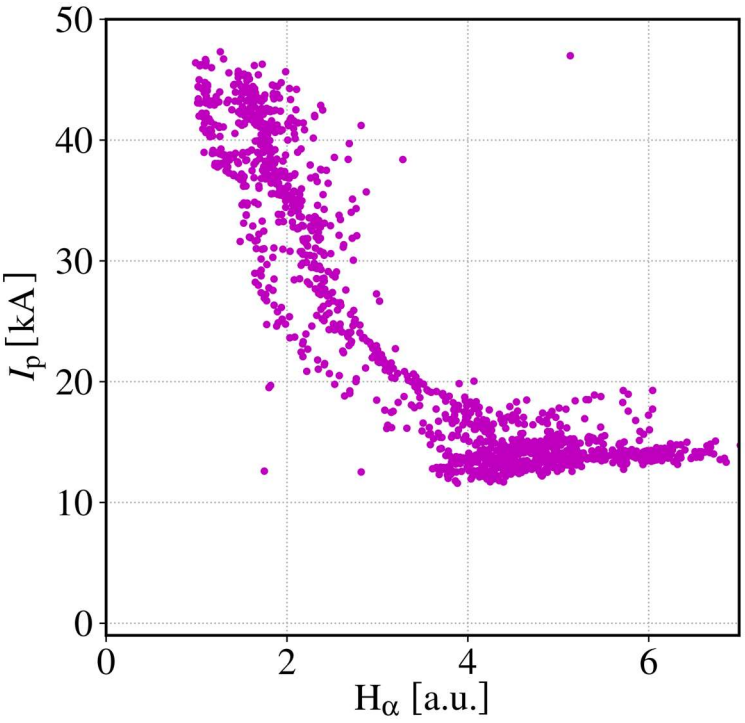

Figure 4.25. The plasma current I_p as a function of H_α intensity.

affected by the plasma-wall interaction via netural emission from wall.

The influence of plasma-wall interaction was evaluated by the plasma touching area measurement by 2D visible light image. The vicinity of the surface of the CS cover was selected as shown in Figure 4.27. There are 640×480 pixels in the image, and the selected region of 215–230 and 130–420 pixels along the x and y axes, respectively. In order to count the bright pixel number showing the presence of plasma in this observed area, the threshold intensity was set the intensity level 250 in the maximum intensity level 256 for 8–bit intensity. In Figure 4.28, the reduction of the counted bright area and the shrinking of the plasma size on the CS cover surface as same as the H_α reduction were shown. The plasma shrinking in the transition phase might reduce the plasma-wall interaction. The plasma-wall interaction plays an important role in the plasma ramp-up and is likely to bring the difficulty of the reproducibility of plasma ramp-up. In fact, plasma ramp-up was frequently fault due to the excessive gas emission caused by the recycling of hydrogen stored in the wall. The high reproducibility could be confirmed when the plasma position was controlled by the CS coil to keep a plasma detachment from the wall during plasma ramp-up. This also predicts that a sophisticated control of neutral density is possible to maintain the bulk heating for a longer duration, but it could not be obtained due to the difficulty of electron density control. This will be a future work.

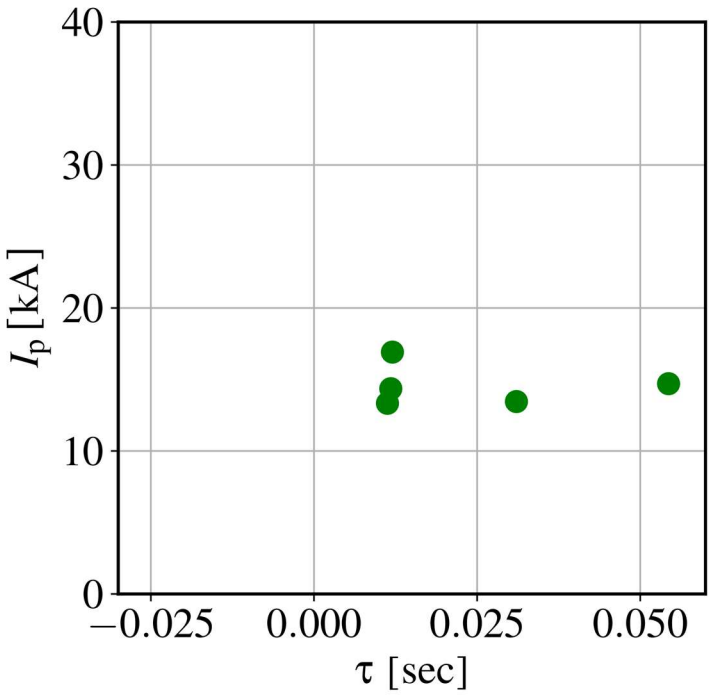

Figure 4.26. The plasma current I_p as a function of the time delay $\boldsymbol{\tau}$. The plots are based on the maximum negative mutual correlation function between H_α and I_p. A positive time delay τ indicates that the H_α reduction occurred faster than the plasma current increment.

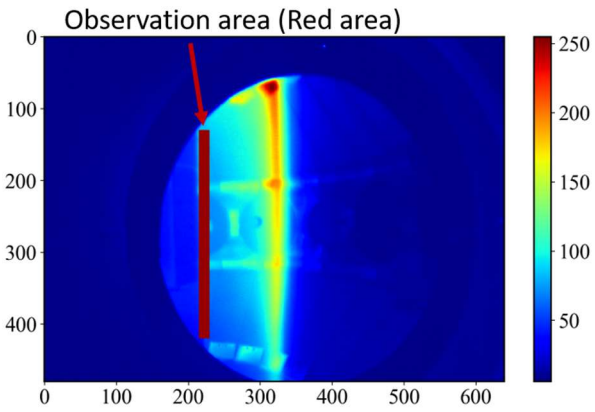

Figure 4.27. The observation area around the CS cover in the visible camera analysis.

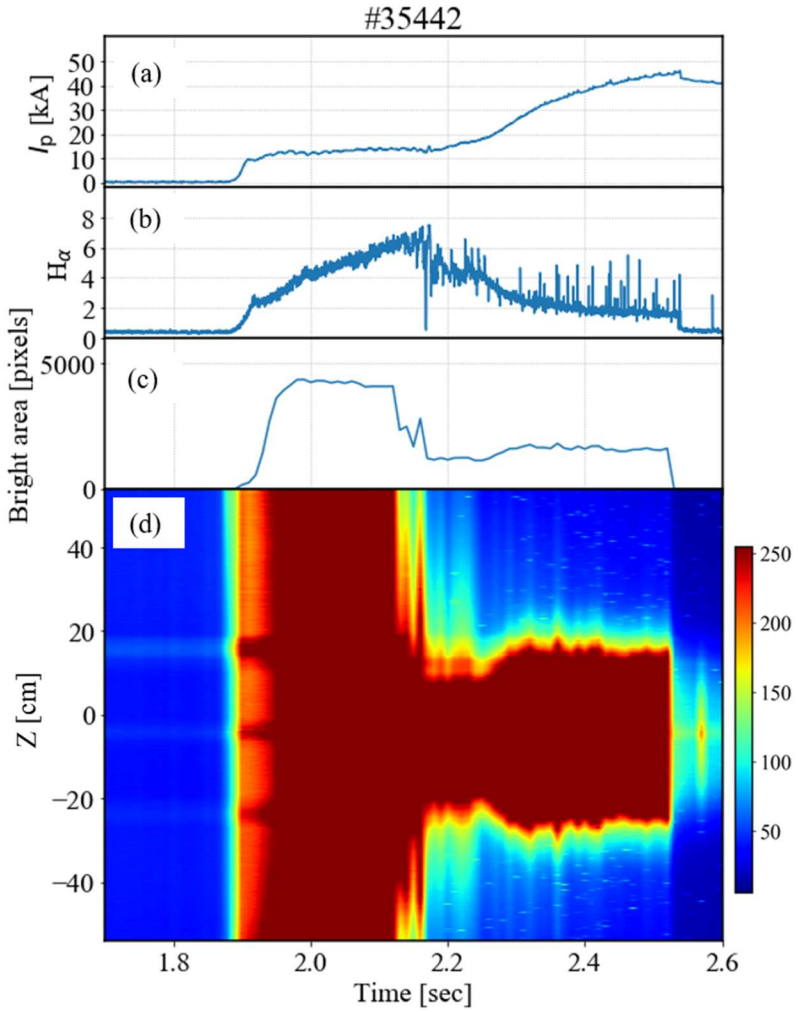

Figure 4.28. The time evolution of (a) plasma current, (b) H_α intensity, (c) bright area, (d) z profile of the visible light on the surface of CS cover.

4.6 Conclusion

In QUEST, the non-inductive plasma current start-up using 28 GHz second harmonic ECRH has been demonstrated. The two different measurement systems were used as the Thomson scattering system and the HXR measurement system to measure the behaviors of the bulk electron and the tail electron. The electron energy shift from the bulk electron heating to the tail electron heating in second harmonic ECRH was observed. This electron energy shift has not been observed in experiments by using the fundamental ECRH. The tail electron temperature and density were estimated to satisfy the two consistencies. One is a consistency of driven current by the observation in the experiment and the simulation by the ray-tracing using RT-4 code. Another is the consistency of the stored energy by the magnetic reconstruction using EFIT code and the calculation including the tail electron parameters. The estimated tail electron temperature and density were guaranteed by the comparison of the observed HXR emission and the detectable bremsstrahlung emissivity by them. The RF single-pass absorption ratio between bulk and tail electrons based on the estimated tail electron parameters were evaluated. Not only the single-pass absorption but also the RF absorption power assuming multi-pass absorption was estimated by the power balance. The total RF absorption power is constant ~ 25 % of the total injection power regardless of whether the bulk or the tail electron heating. The finite Larmor radius effect causes the high RF absorption and the oblique injection enhanced the Doppler shift effect. The both effects give the highly efficient RF absorption and current drive in tail electron heating. Once, the tail electron heating is caused and enhance the RF absorption for the tail electron, and the energy exchange by tail-bulk electron collision is decreased. Finally, the positive feedback loop of the tail electron heating and the negative feedback loop of bulk electron heating are formed. Thus, the electron energy shift occurs. The finite Larmor radius effect is seen in only high harmonic ECRH not in fundamental ECRH. The sudden plasma current ramp-up was observed in tail electron heating independent with electron energy shift. The driven plasma current increase by the tail electron was observed after the neutral particle reduction due to the plasma-wall interaction less.

The electron energy shift by higher harmonic ECRH may be going to be an important mechanism for the near future operation. On one hand, the current drive efficiency is quite high in the case of the tail electron heating, the high-density plasma sustained by high plasma current can be generated as target plasma for NBI. On the other hand, there is the possibility that the incredibly high energy electron such as runaway electron to damage the wall will be generated. The operation region of electron energy must be selected depends on the operation object. The investigation of the selectivity of the energy shift for the avoidance of the tail electron heating is the future work.

5. 8.2 GHz fundamental X-mode high field side injection

5.1 Introduction and motivation

EBWH is a candidate to generate plasma production and plasma current start-up, because EBW which is a kind of electrostatic wave can propagate and heat the plasma without the cut-off density. Although the electrostatic wave has to be excited from ECW, because the electrostatic wave cannot propagate the vacuum region. In general, the slow X-mode mode couples to EBW at upper hybrid resonance (UHR) due to the corresponding roots of both dispersion relation. Various methods were applied to excite EBW. A method for EBW heating in STs was first proposed by Cairns et al [70]. The mode conversion methods from ECW to EBW have been established three types of methods. The general method as known as the O-X-B mode conversion involves excitation of EBW by ECW injection from low field side (LFS) of the magnetic field. The O-X-B mode conversion is carried out by the double mode conversion from ordinary mode (O-mode) to extraordinary mode (X-mode) at O-mode cutoff layer and X-mode to electron Bernstein mode (B-mode) at UHR layer. The O-X-B mode conversion was demonstrated in LATE [44], TCV [71], W7-AS [50] and LHD [51]. The O-X-B mode conversion via the double mode conversion has the difficulty to obtain the high mode conversion efficiency with the large density change during the plasma current start-up. The most key part is the O-X mode conversion. The proper injection angle to fit with the density profile is required. The second method is X-B mode conversion from LFS injection. The X-B mode conversion from LFS injection was achieved in TST-2 [43]. It requires the very steep density gradient to obtain high mode conversion efficiency, so it also difficult to apply to the plasma current start-up. Third method is X-B mode conversion from HFS which is the simplest and promised to obtain highly efficient conversion. The access of X-mode to UHR layer can convert the EBW in case of the plasma density less than L-mode cut-off without the injection angle adjustment and the steep density gradient. The code simulation for EBW excitation in QUEST was expected by Ray-tracing code GENRAY [72]. It showed that X-B mode conversion from HFS is possible without a complicated injection angle adjustment and O-X-B mode conversion requires the injection angle adjustment [73]. The X-B mode conversion from HFS has been investigated in COMPASS-D [41] , WT-3 [74], LHD [39], Versator II [38] and QUEST [75]. In LHD, the direct launching of the X-mode from HFS is possible to utilize a merit of helical magnetic field [39]. In presented experiments, most of devices uses a mirror located on the CS surface except QUEST. However, the use of mirror is difficult to confirm the mode purity of X-mode after reflection at the mirror. Thus, in this research, the direct X-mode injection from HFS was planned by setting ECW antenna inside QUEST and the experiment was performed. The comparison of direct X-mode injection from HFS and O-mode injection from LFS has been demonstrated to confirm the EBWH property.

The observation of the EBW excitation by the mode conversion is critical point. In case of O-X-B

mode conversion from LFS injection, the monitoring stray radiation to evaluate O-X-B mode conversion efficiency is a useful [51]. If the O-mode could mode convert to the X-mode, the stray radiation was deceased showing the high mode conversion efficiency. In case of LFS injection, the observation of over-dense plasma than cut-off density of ECW is one of the collateral evidences to show the EBW excitation. However, in the case of HFS injection, the observation of the stray radiation and the over-dense is not be useful to determine EBW excitation, because it does not matter with RF cut-off. The collateral observation of the mode conversion should be established to determine EBW excitation regardless of any mode conversion method. The observation of parametric decay instability (PDI) which is known as three-wave parametric decay process is a good candidate for the collateral observation of the EBW excitation. In Versator II, the parametric decay waves (PDWs) of the upper hybrid wave and the lower hybrid wave (LHW) frequency ranges were observed in X-mode injection from HFS[38]. The large amplitude of the electric filed in the UHR with the mode conversion produce PDWs which may provide the collateral evidence of the EBW excitation. In this research, the observation of PDWs by using the electrostatic probe was applied to plasmas with both injections.

5.2 Experimental setup

The direct X-mode injection was realized by inserting an antenna inside the vacuum vessel. Two main transmission lines made of copper waveguides were installed as shown in Figure 5.30. The copper waveguides for vacuum conditions were connected to atmospheric RG-50 waveguides connecting with 20kW/8.2 GHz klystrons. The switch was inserted between klystron and main waveguide to change HFS injection and LFS injection smoothly. To avoid arcing inside the antenna due to cross the ECR layer, SF_6 gas was filled up until the vacuum window from klystron. The vacuum windows were installed in HFS of ECR layer. The avoidance of arcing was confirmed in the bench test before the installation. The vacuum window was not equipped with a water-cooling system, so the discharge time was restricted to short durations. For the X-mode HFS injection, the polarization of X-mode was adjusted by TE_{10} waveguides directions. The surface of the HFS injection antenna was located at R = 323 mm. The plasma contacting with the cupper waveguides was prevented by the stainless steel cover SUS304 and two tungsten limiters next to the antenna. The tip of the tungsten limiter was located at R = 363 mm.

The injected RF power was typically 40 kW. Each transition line injects 20 kW. The fundamental ECR layer for the 8.2 GHz ECW was located at R = 437 mm. The toroidal magnetic field is 0.21 T at R = 600 mm.

All measurement systems are drawn as Figure 5.29. The injected RF wave was reflected by the surface of the center stack and detected by the antenna located at the same observation port. RF leakage monitor (RLM) was equipped outside of vacuum vessel and the signal was used to evaluate the RF absorption. Two electrostatic probes were equipped. One probe was placed at R= 465 mm, Z =820 mm

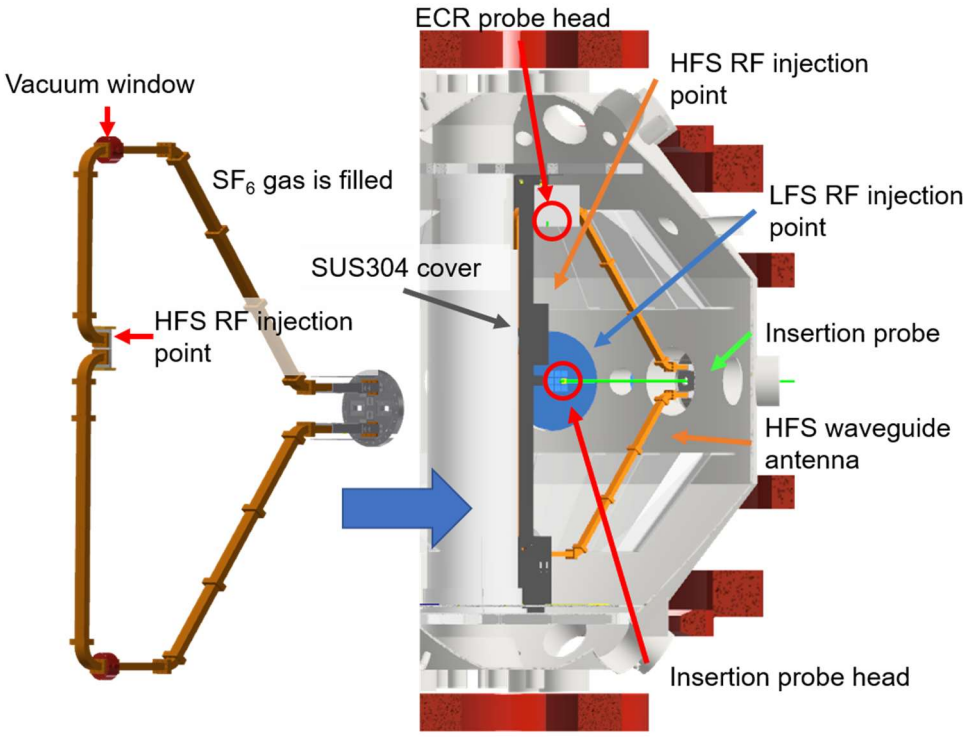

Figure 5.30: The schematic drawing of HFS injection system and the measurement systems.

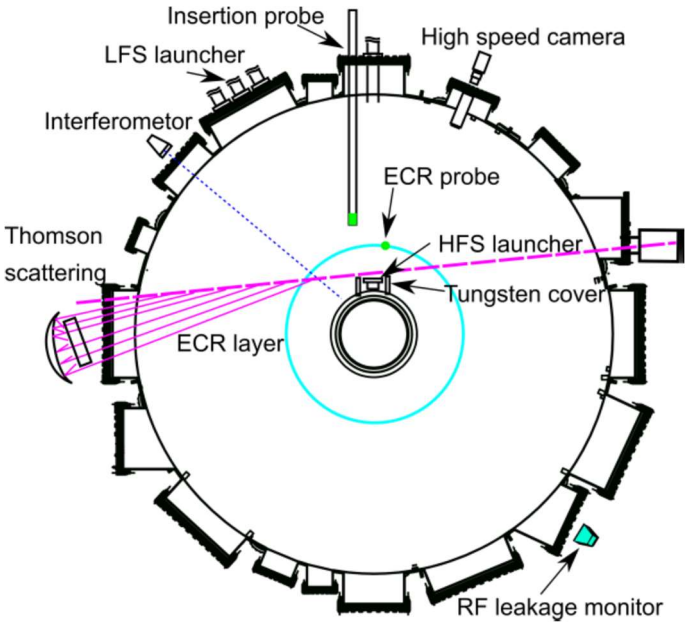

Figure 5.29: The schematic drawing of the measurement systems.

around ECR layer (ECR probe) and next to the sustain less steel cover. Another probe can be inserted in plasma from R = 400 – 1150 mm, Z = 0 mm (Insertion probe). ECR probe works the reference signal to confirm the plasma reproducibility. The insertion probe was pulled back to R = 1150 mm during the Thomson scattering measurement, so the simultaneous measurement could not be obtained.

The exposed electrostatic probe pins were made of tungsten with a diameter of 1 mm and length of 1.6 mm. The insertion probe was sustained by stainless steel SUS304 pipe. The stainless-steel pipe was covered by an alumina ceramic tube with a length of 960 mm. The discharge duration for PDI measurement was quite short < 30 ms to avoid the damage and cracks due to heat load in the alumina ceramic cover. The probes were connected to an oscilloscope with -20 dB attenuator. The oscilloscope was type HDO8038A which could measure a sampling rate of 1.25 GS/s.

5.3 Comparison of X-mode high field injection and O-mode low field injection with Open magnetic field surface

The plasma current startup was performed non-inductively. The relatively long discharge time was restricted for 110 ms in this experiment. The result of HFS and LFS injections is shown in Figure 5.31. The same RF power and same magnetic field applied on both injections. The clearly different

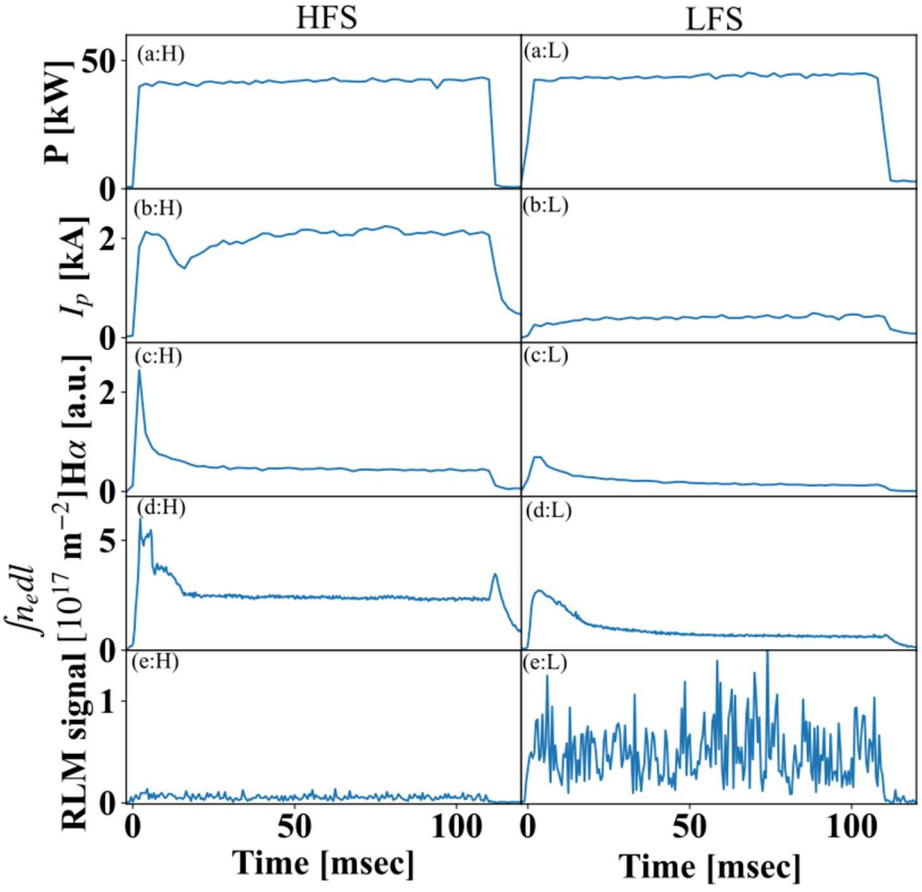

Figure 5.31: Time evolution of (a: H, L) RF input power, (b: H, L) plasma current, (c: H, L) line integrated density, (d: H,L) H α intensity, and (e: H, L) RLM signal. (a - e: H) X-mode HFS injection. (a - e: L) O-mode LFS injection. In (e: H, L), a green dotted line shows the maximum value of RLM signal in no plasma with same input power.

performance was observed. The plasma current was high ~ 2 kA in HFS injection and low ~0.5 kA in LFS injection. Four times higher plasma current in HFS injection than in LFS injection was observed. The line integrated densities were $\int n_e dl \sim 2.5\times10^{17}$ m^{-2} in HFS injection and $\int n_e dl \sim 1\times10^{17}$ m^{-2} in LFS injection. The RLM signal showed the low RF leakage in HFS injection. The HFS injection showed better performance than the LFS injection. The RF leakage signal was investigated to estimate approximate RF absorption. The investigation was carried out roughly, but it can indicate the approximate RF absorption efficiency, not absolute RF absorption.

$$P_{leak} = V/A_{leak} \qquad 5.51$$

where, the partial leaked power is P_{leak}, the RLM signal is V, the ratio between RLM signal and the partial leaked power in case of the RF injection for vacuum condition is A_{leak}. When we consider the assumption that the A_{leak} is fixed in case of plasma discharge, the estimation of RF absorption is given. The uncertainty about A_{leak} constant exists due to the reflection and interference of RF. A_{leak} was given from three discharges of RF injection to vacuum condition as shown in Figure 5.32.

The calculated A_{leak} for HFS and LFS injections were different. A_{leak} for HFS injection is 14.1 mV/kW, A_{leak} for LFS injection is 16.9 mV/kW. The difference should come from the difference of antenna location and injection angle. The RF absorption ratio R_{abs} can be given by Eq. 5. 52.

$$R_{abs} = (1 - P_{leak}/P_{in}) \times 100\% \qquad 5.52$$

The averaged RF absorption ratio R_{abs} from 10 ms to 100 ms for HFS injection and LFS injection show approximately 98 % and 30 %, respectively. In case of HFS injection, most of the RF input power was absorbed, which is acceptable in the theoretical view of EBW mode conversion and absorption.

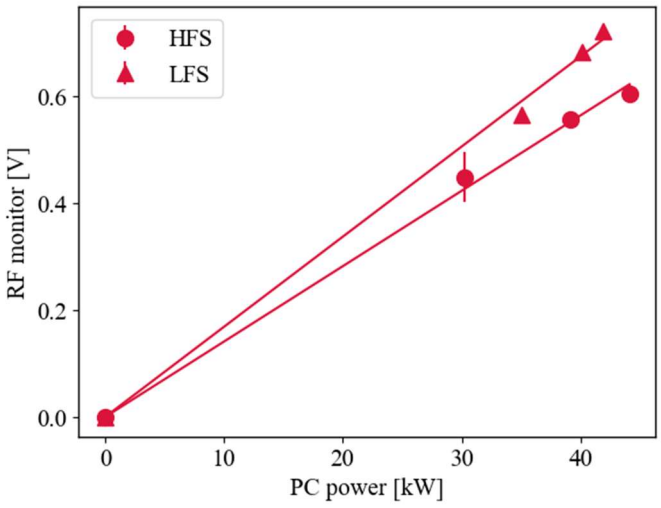

Figure 5.32: RF Leakage and klystron power from HFS injection and LFS injection without applying magnetic field.

The measured electron temperature and density also showed the high performance in HFS injection as shown in Figure 5. 33. The electron density peaks of both injections were $n_e \sim 5 \times 10^{17}$ m^{-3} in HFS injection and $n_e \sim 4 \times 10^{17}$ m^{-3} in LFS injection. The O-mode cutoff density at 8.2 GHz was 8.7×10^{17} m^{-3}. In both injections, the over-dense region was not observed on the estimated and measured electron density profile. Thus, it was not possible to obtain the O-X-B mode conversion from the LFS injection. The broad electron density profile was observed in the HFS injection, and the narrow-peaked electron density profile was obtained in the LFS injection. The EBW mode conversion should be confirmed in HFS injection.

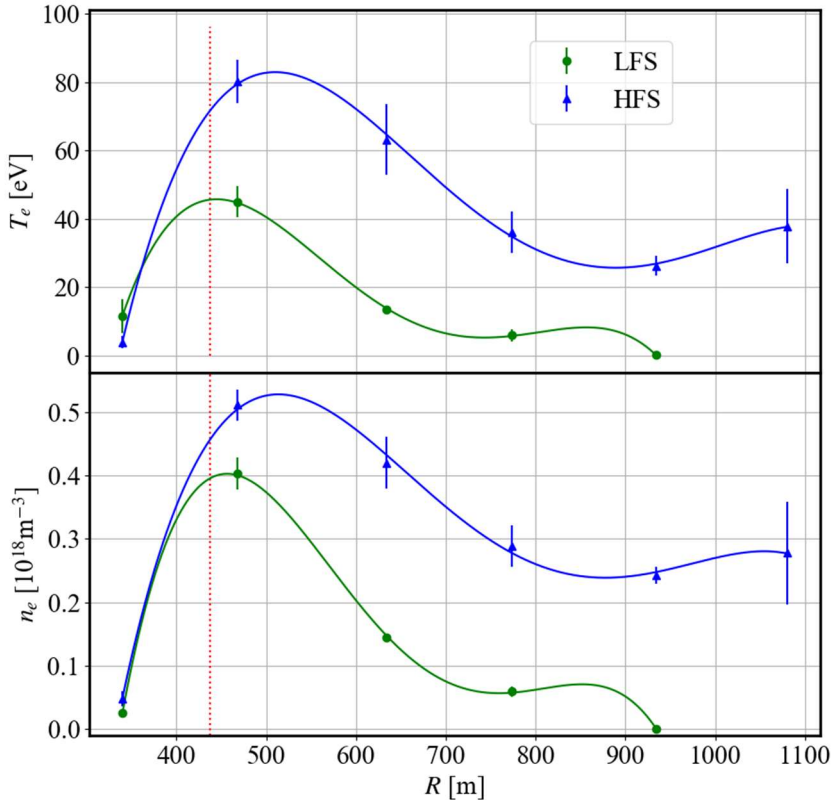

Figure 5. 33: The electron temperature and density distribution at t = 102 msec. Blue and green lines are HFS injection, LFS injection, respectively.

5.4 PDW Measurement in HFS injection and in LFS injection

The insertion probe was used for PDW measurement to confirm EBW excitation. The insertion probe was inserted at each 5 cm with plasma due to a reproducible operation. The discharge time was 10 ms to avoid the significant damage to the probe from the heat flux of the plasma. The plasma currents on each insertion probe location are shown in Figure 5.34. The plasma currents on each insertion location were consistent in the latter part of discharge, although, the peak value was decreased by the inserting deeply at the initial part of the discharges.

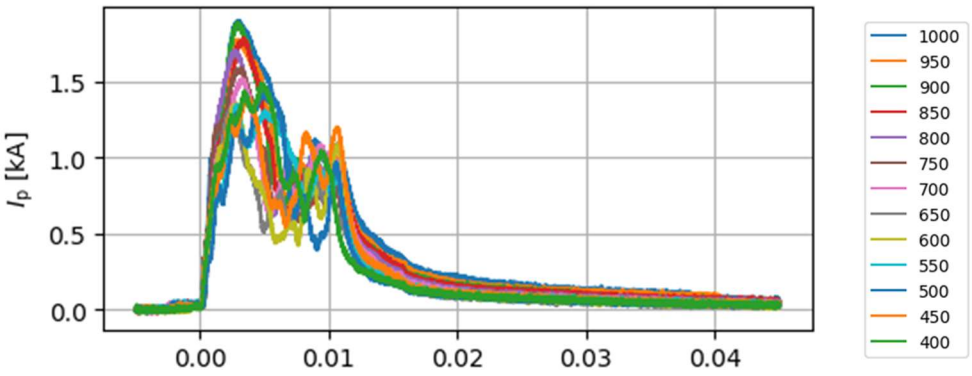

Figure 5.34: The plasma current for each insertion probe location.

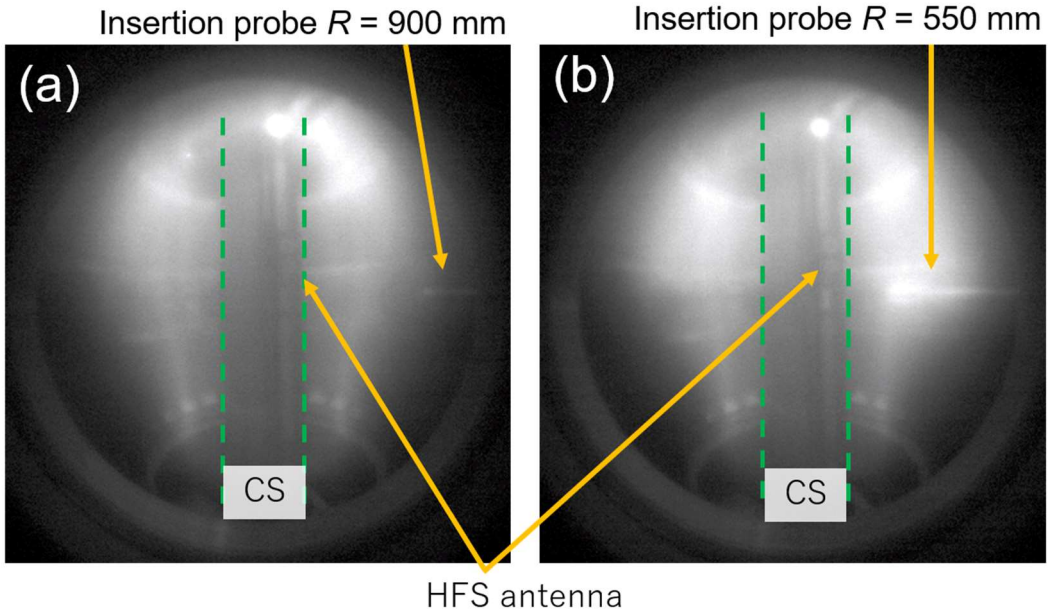

Figure 5.35 The visible light video images in the HFS injection at 5 msec. (a) Plasma without insertion probe (R = 900 mm). (b) Plasma with insertion probe (R = 550 mm).

The latter part of the insertion probe signal was used to compare the discharge property. The camera image of plasma with (R=550 mm) and without inserting the probe (R = 900 mm) in the HFS injection were recorded, as shown in Figure 5.35. A slightly bright area was induced by the insertion of the probe in open magnetic surface [see Appendix VI].

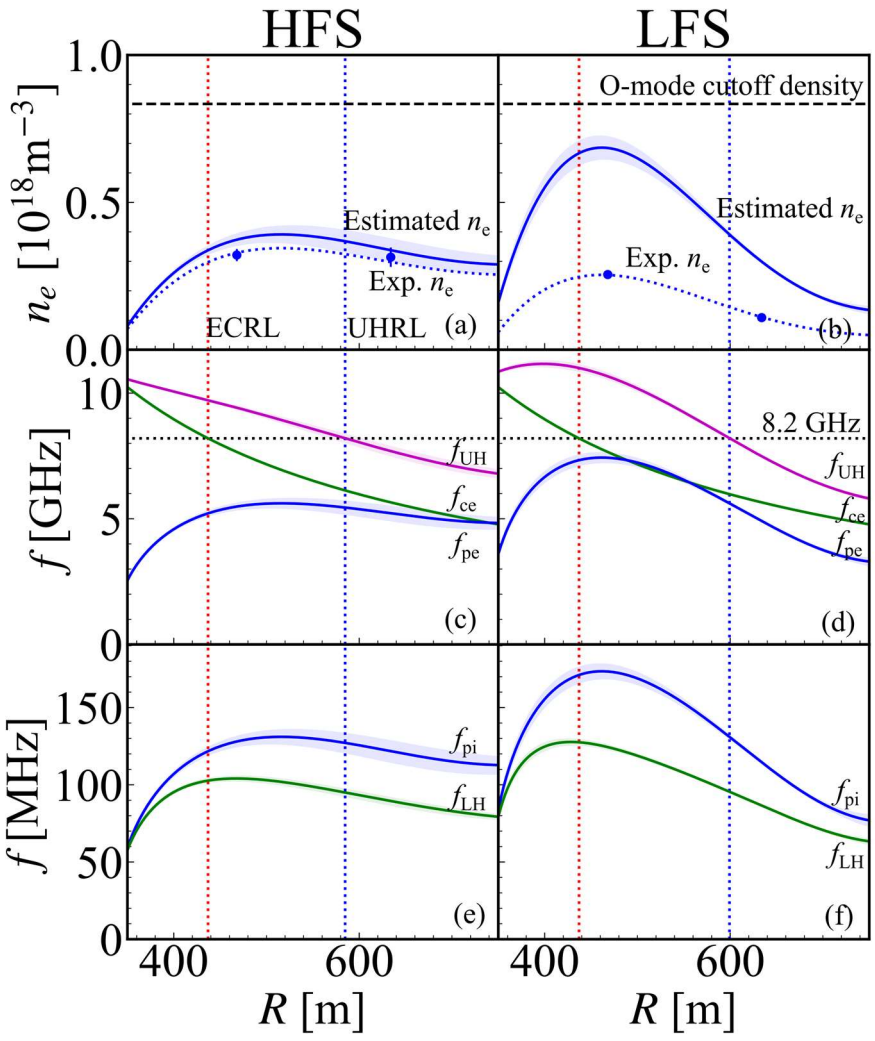

Figure 5.36: (a,b) The solid blue lines show the estimated ne profiles during 8.5–9.5 msec for HFS (#39351) and LFS (#39358) injections. The dotted blue lines show the obtained ne profiles by the Thomson scattering measurement (HFS: # 39395, LFS: #39410). The black dash line shows the O-mode cutoff density. (c–f) The calculated frequencies that depend on the estimated electron density distribution. The red, blue and dotted -black lines show the locations of the ECR layer, UHR layer and the frequency of the injected ECW. (a, c, e) The HFS injection. (b, d, f) The LFS injection. (c, d) Frequency of GHz order in the R direction. The solid blue, green, and magenta lines show the electron plasma frequency, the electron cyclotron frequency, and the upper hybrid frequency, respectively. (e, f) Frequency of MHz order in the R direction. The solid blue and green lines show the ion plasma frequency and the lower hybrid frequency, respectively.

The estimated electron density profiles are shown in Figure 5.36 (a, b). To estimate a density profile, the line integrated electron density and Thomson scattering measurement were used, however the correction was necessary to regulate their different measurement timing [see Appendix VII]. According to the estimated electron density profiles, the characteristic frequencies of interest were calculated, as shown in Figure 5.36 (c–f). The corresponding location with the upper hybrid frequency and the injected wave frequency shows the UHR layer location. The UHR layer of the HFS and LFS injections were located at $R = 575$ mm and $R = 600$ mm, respectively. In the experiment, the discharges on the probe, inserted on $R = 550$ mm and $R = 600$ mm, were selected to analyze the PDW for the HFS and LFS injections, respectively. The detectable PDW frequency by insertion probe is on the range of LHW frequency. The LHW frequencies on HFS and LFS injections are $\cong 95 \pm 3$ MHz and $\cong 95 \pm 1$ MHz at the UHR layer, respectively. The ion plasma frequency is close with the LHW frequency. The ion plasma frequency on HFS and LFS injections are $\cong 127 \pm 6$ MHz and $\cong 131 \pm 1$ MHz at the UHR layer, respectively.

The time evolution of the averaged power spectrum density (PSD) magnitude of the broadening of the low-frequency PDW from 90 MHz to 110 MHz is as shown in Figure 5.37. The time evolution of

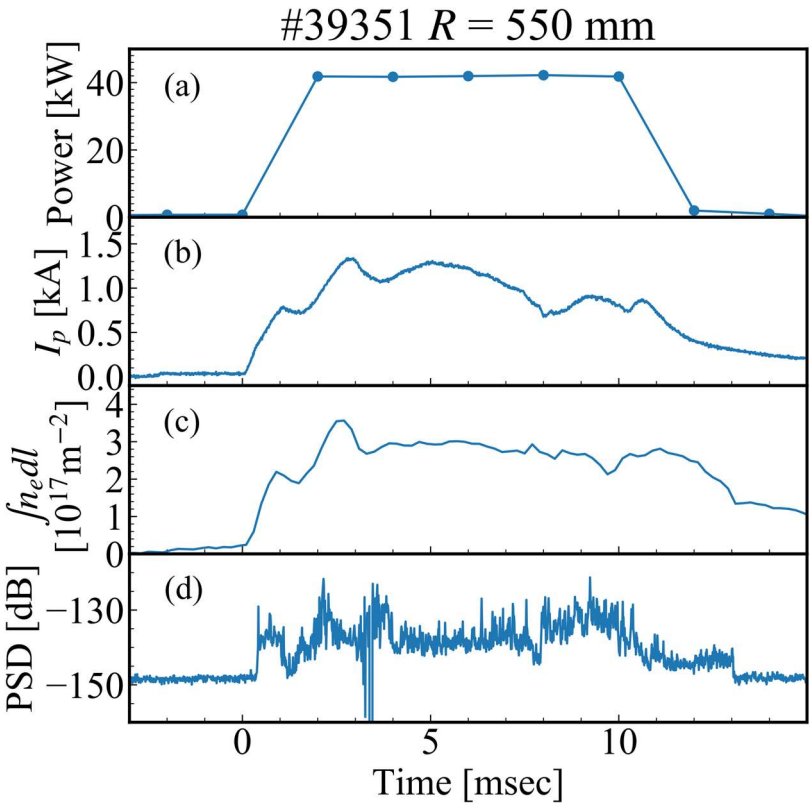

Figure 5.37: Time evolution of (a) RF power (time resolution 2 msec), (b) plasma current, (c) line integrated density and (d) the averaged FFT spectrums for 90–110 MHz range on the insertion probe.

the averaged PSD magnitude does not accurately show the PDW intensity because the PDW frequency is changed by the drastically change of electron density profile, but the possibility of maintained EBW excitation for the entirety of the discharge is shown in the X-mode HFS injection.

The spectra by the fast Fourier transform (FFT) analysis were got as shown in Figure 5.38, The spectra was obtained by analyzing the measured potential signals with the insertion probe around the UHR layer and the ECR probe as the reference signal. As shown in Figure 5.38 (c), the clear amplitude enhancement in the broad frequency range up to 250 MHz was observed by the insertion probe in HFS injection. In Figure 5.38 (a), the spectra on the ECR probe on HFS injection was also observed in the broad frequency. By comparing with the ECR probe and the insertion probe, the increment of amplitude by the insertion probe was clearly much larger than that by the ECR probe. It suggests that the wave having such spectra were excited around the UHR layer and propagated to the ECR probe direction. In contrast, such spectra were not observed in LFS injection. The clear difference was obtained by the injection direction. The PSD denoted in Figure 5.38 (c) displays a strong spectrum of around 80–120 MHz including PDW frequency and a spread in the range of 40–240 MHz in the X-

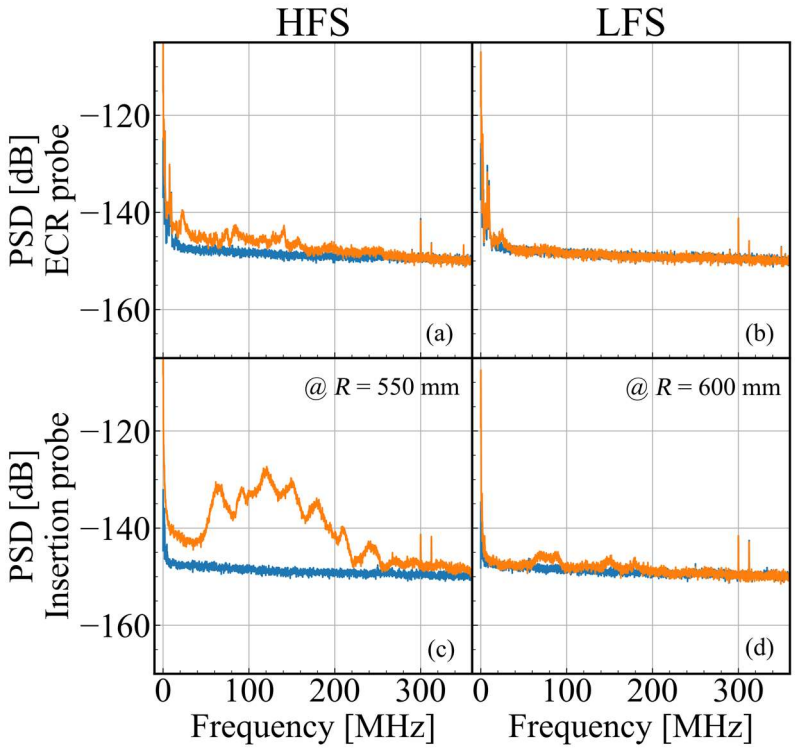

Figure 5.38: Power spectral densities (PSDs) of (a, b) the ECR probe and (c,d) the insertion probe around the UHR layer (HFS: R = 550 mm, LFS: R = 600 mm) on (a,c) HFS injection (# 39351) and (b,d) LFS injection (#39358). The blue lines are PSDs before RF injection. The orange lines are PSDs in the time range of 8.5–9.5 msec.

mode HFS injection. The actual low-frequency PDW frequency should be spread to the higher side from LHW frequency by the effect of ion temperature [76]. Frequencies lower than the LHW frequency might indicate the propagation of low-frequency PDW which was generated in lower densities on the UHR layer. On the other hand, few PSDs showing PDW were observed in the O-mode LFS injection as shown in Figure 5.38 (d), due to the lack of no mode conversion through O-X-B and X-B from LFS as indicated by their electron density profiles. Even in LFS injection, the possibility of X-B mode conversion from HFS through multi-pass reflection is remained. The clear difference of the PSDs between the both injections showed the mode conversion efficiency. The observed broadening of the PSD in HFS injection does not conflict to the previous observation of the PDW spectrum in Versator II [38]. The broadening of the spectrum achieved the second harmonic frequency (190–240 MHz); however, the second peak was obscured. This may be caused by the difference in low-frequency PDW (≅ 400 MHz in Versator II and ≅ 95 MHz in QUEST). The gap between fundamental and second harmonics of PDW may be buried by the frequency broadening. It is unclear whether the presence of second harmonic frequency is caused by wave excitation at the resonance or by the sheath on the surface of the probe [38, 17].

The high-frequency PDW should be measured to prove the three-wave coupling. The combined RF injection was performed by HFS and LFS injections with each 20 kW. The half of RF power was injected from LFS, although, the EBW excitation was expected by HFS injection. One of RF injection antenna in HFS injection was used to detect high-frequency PSD. The coupler with -60 dB attached on the injection antenna divided the signal to spectrum analyzer. The obtained spectrum is shown in

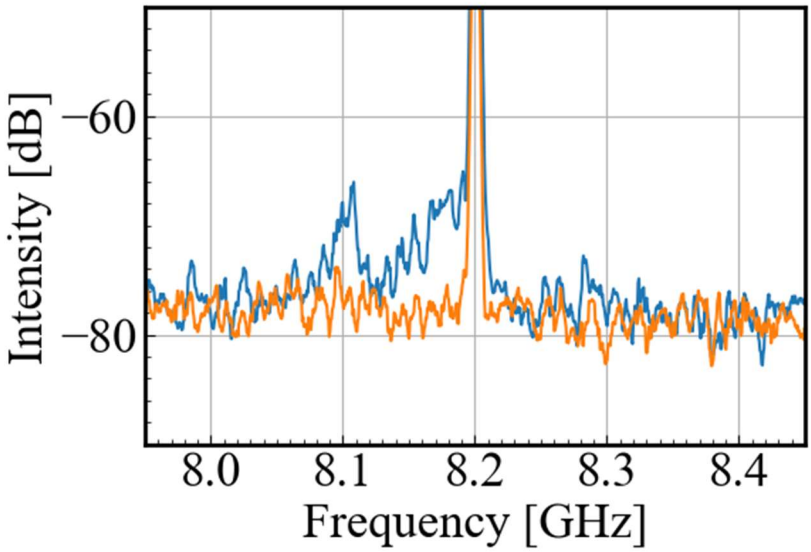

Figure 5.39: The spectrum detected by the HFS antenna on the combined injection from HFS and LFS and LFS injection only. Blue line shows the combinate injection. Orange line shows the LFS injection only.

Figure 5.39. The expected frequency of high-frequency PSD was approximate 8.1 GHz. It was compared with LFS injection. In Figure 5.39, the highest spectrum is on 8.2 GHz which is the injected RF frequency as ECW X-mode. The small spectrum of -65 dB is on 8.1 GHz. In case of LFS injection only, the spectrum on 8.1 GHz is same level with background signal of -75 dB. The observed spectrum in HFS injection indicates the high-frequency PSD. Unfortunately, the simultaneous measurement could not be obtained because the detection antenna is far, but the spectrums indicating PDI through the three-wave coupling process. The PDI measurement indicates the EBW excitation in the HFS injection.

5.5 Plasma current start-up with closed flux surface configuration

We tried to demonstrate the plasma current start-up by EBWH. The formation of a closed flux surface is the minimum requirement to demonstrate the the plasma current start-up. The adjustment of vertical magnetic field is required to form the closed flux surface. Only using a pair of PF coils cannot change the vertical magnetic field configuration. The method to form the closed flux surface using the trapped particle driven procession currents is namely the trapped particle configuration (TPC) which was suggested by Forest *et al*. [78] and demonstrated by the numerical simulation by Ono *et al*. [65]. In the TPC, the vertical magnetic field configuration was described by the decay index which was investigated by Uchida *et al.* [79]. The decay index is given as Eq. 5.3. According to Uchida *et al.*, the necessary decay index depends on the aspect ratio. For example, in aspect ratio of 3, the necessary decay index is approximate 0.3. In the STs, the necessary decay index is enough low. In this experiment, the HFS injection antenna locates in HFS and plays as an inboard limiter. Thus, the required decay index is expected high due to the high aspect ratio by the HFS antenna.

$$n_{index} = -\frac{R}{B_z}\frac{\partial B_z}{\partial R} \qquad 5.3$$

The decay index was given by the vector potential calculation by the poloidal field coil currents [see Appendix V].

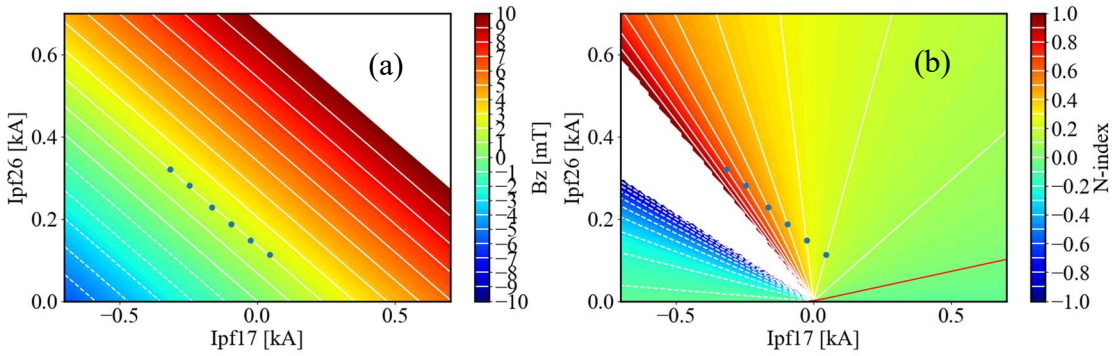

Figure 5.40: The decay index adjustment from 0.2 to 0.7 on vertical magnetic field of 2 mT by PF 2-6 and PF 1-7 coils. (a) The color contours of the vertical magnetic field on R = 0.6 m. (b) The color contours of decay index (N-index) on R =0.6 m.

The optimized the decay index and the vertical magnetic field were investigated to form the closed flux surface. The used poloidal coils were PF 1-7 and PF 2-6 coils. The decay index on the constant vertical field on the major radius was surveyed. The general major radius is R = 0.6 m. The coil currents for each poloidal coil were applied on the decay index on 0.2 − 0.7 on the different vertical magnetic field on 1, 1.5, 2, 2.5 mT, respectively. The poloidal coil currents on the decay index on 0.2 − 0.7 on the vertical magnetic field of 2 mT were estimated as shown in Figure 5.40.

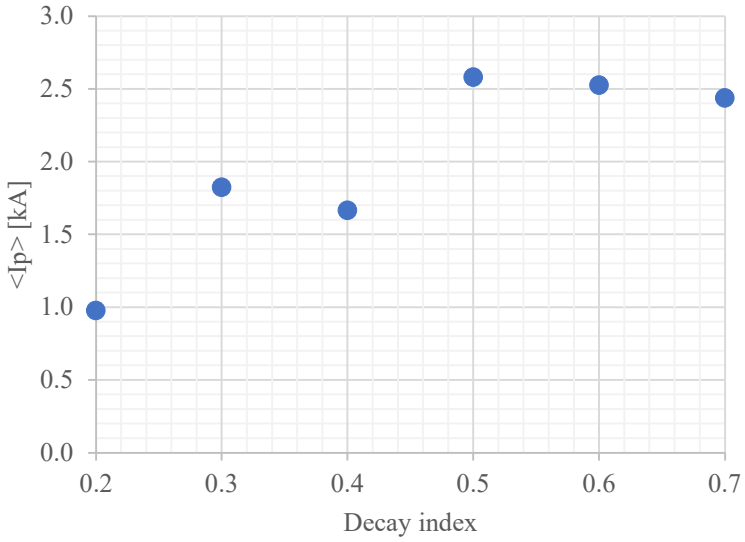

Figure 5.41: The averaged plasma current for decay index adjustment from 0.2 to 0.7 on vertical magnetic field B_z of 2 mT. The current jump was observed from decay index 0.5 in HFS injection.

In the case of vertical magnetic field of 2 mT, the average plasma current for the decay indexes in HFS injection are shown in Figure 5.41. The average plasma current is a good indicator showing the current jump. The current jump is known as a specific feature of the closed flux surface formation as investigated by Yoshinaga *et al.*[80] and supported by Uchida *et al.*[79]. When the plasma current jump occurs the average plasma current increase. Until decay index 0.4, the current jump was not observed. From decay index of 0.5, the current jump was observed. The same vertical magnetic field

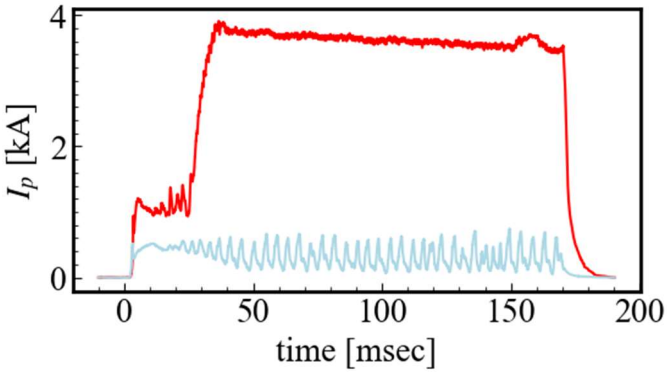

Figure 5.42: The plasma current on HFS injection and LFS injection at decay index of 0.5 and vertical magnetic field of 2 mT. In HFS injection, the plasma current jump was observed.

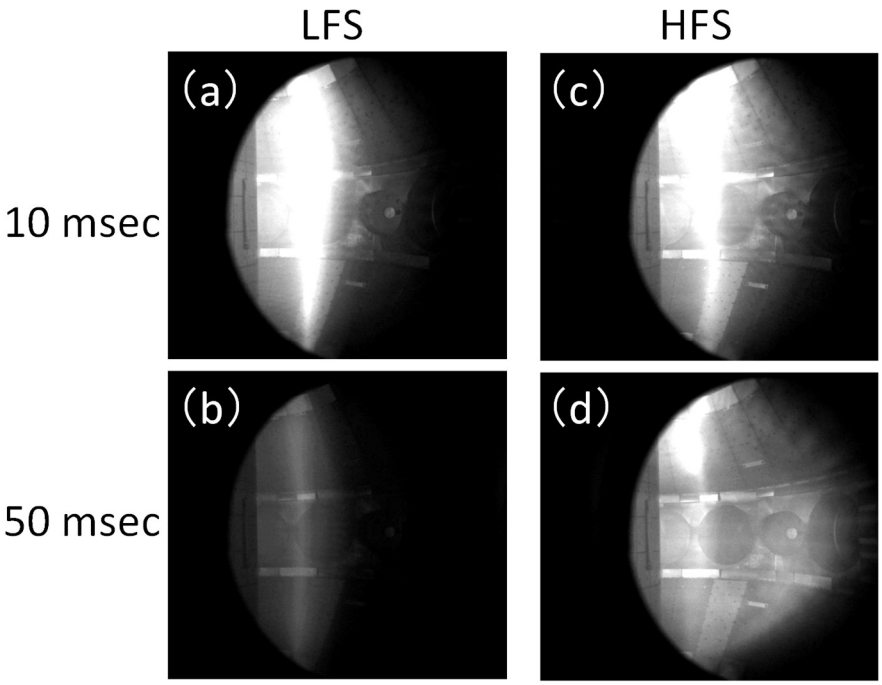

Figure 5.43: The high-speed camera images on LFS and HFS injection at t = 10 msec and 50 msec at decay index of 0.2 and vertical magnetic field of 2 mT. (a, b) The camera images at 10 msec and 50 msec in LFS injection. (c, d) The camera images at 10 msec and 50 msec in HFS injection.

was applied in LFS injection, but the current jump was not observed as shown in Figure 5.42. In high speed camera image, the formation of closed flux surface was indicated in HFS injection as shown in Figure 5.43 (d). The closed flux surface configuration was observed in camera image during high plasma current. The observation of the current jump and the camera image indicate the formation of the closed flux surface in HFS injection. The achieved plasma current on the closed flux surface configuration was achieved approximate 4 kA which is 8 times higher than one in LFS injection. The difference in the formation of the closed flux surface might be caused by the different heating efficiency by EBWH and ECRH.

The observation of PDI measurement was carried out in the initial phase of the plasma start-up in HFS injection. The insertion probe location was set on R = 1100 mm to avoid the damage from the confined energetic electron and ion. The PDI measurement was carried out for 40 ms to obtain the high sampling rate. The initial part of plasma current start-up was investigated as shown in Figure 5.44. The wide spectrum including the low-frequency PDW was observed from same timing of the plasma

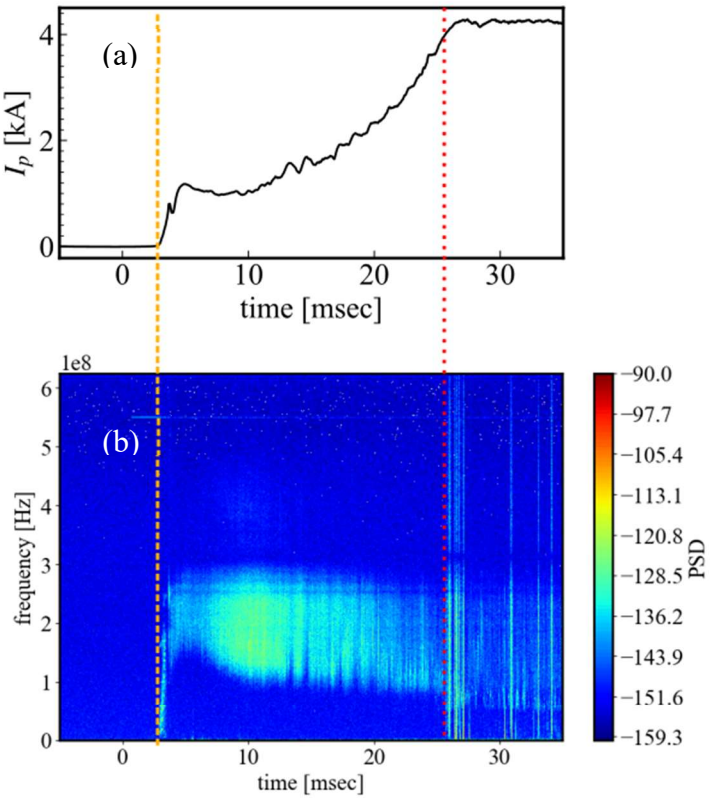

Figure 5.44: (a) The initial part of the plasma current start-up in HFS injection and (b) the color map of power spectrum density (PSD) on the insertion probe . The orange dash line shows the start-timing of the plasma current start-up. The red dot line shows the start-timing of the noisy signal on the insertion probe.

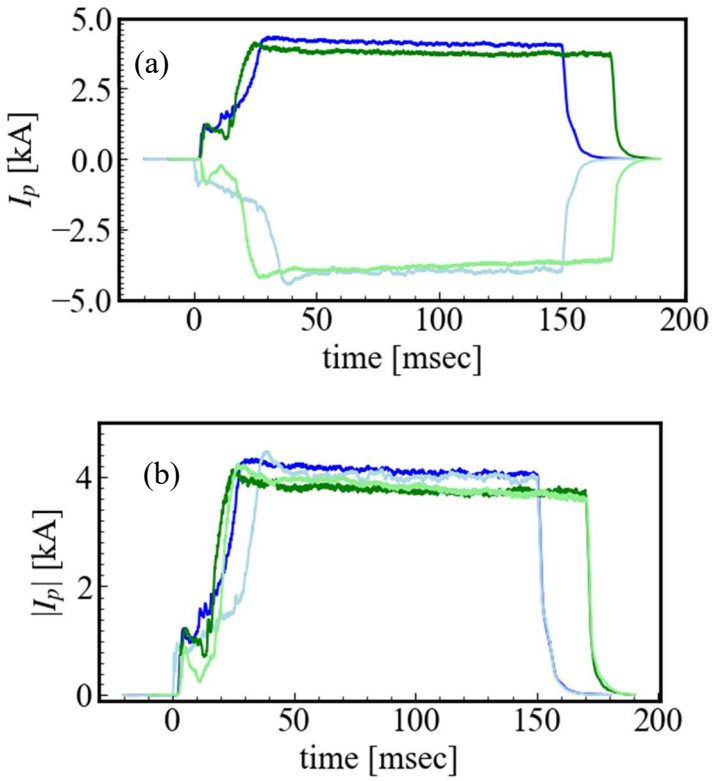

Figure 5.45: (a) The plasma current on different TF coil and PF coil directions. (b) The absolute value of the plasma current on different TF coil and PF coil directions. Blue and light blue line shows the plasma current on negative and positive PF coil current direction on negative TF coil current. Green and light blue green shows the plasma current on negative and positive PF coil current direction on positive TF coil current.

current start-up showing the EBW excitation. This indicates the EBW excitation occurred before the formation of closed flux surface. The noisy signal was started detecting from t = 26 ms. The PDW is a electrostatic wave, so the interaction with antenna and the plasma is necessary to detect signal. The plasma de-touch by the formation of closed flux surface lose the interaction with antenna and plasma. The noisy signal might be caused by the interaction less due to plasma de-touch, or the accelerated energetic electron hitting in confined region. The accelerated energetic electron hitting is also possible noise source, because the insertion probe was broken by sufficient heat load when we inserted inside closed flux surface.

It should be considered the reason of high enough plasma current start-up in HFS injection to form the closed flux surface. The candidates of the plasma current driving source are EBW current drive and pressure drive. The possibility of EBWCD was investigated by the changing toroidal magnetic field coil direction. The EBWCD current direction is changed by the toroidal magnetic field direction as discussed by Shevchenko, *et al*. [41]. Thus, the EBWCD direction should be opposite by the opposite toroidal magnetic field direction. In experimental result, the direction of plasma current was

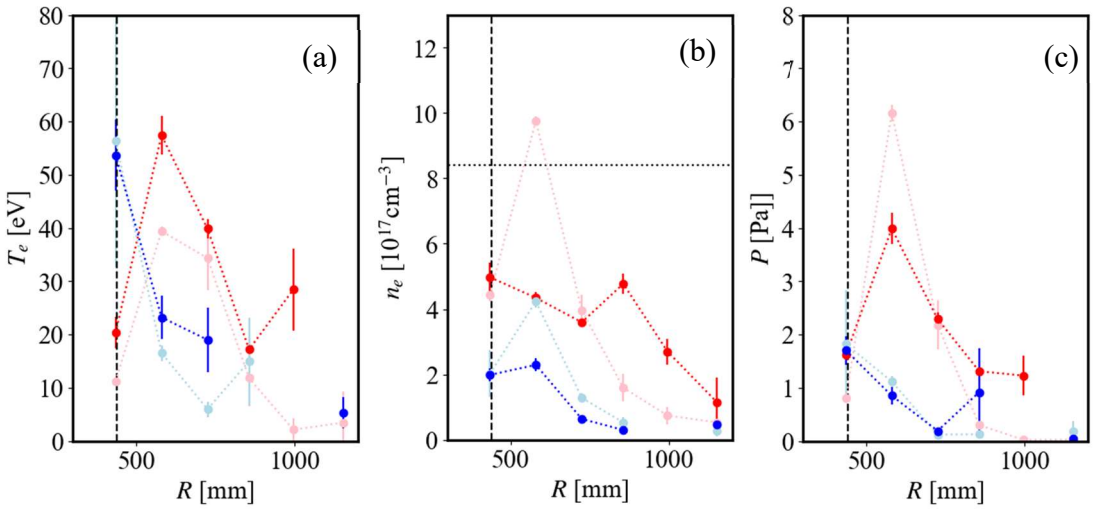

Figure 5.46: (a) Electron temperature, (b) electron density, (c) pressure profiles in HFS injection and LFS injections. Pink and red solid circles show the HFS injection at 21, 121 msec. Light blue and blue solid circles show the LFS injection at 21, 121 msec. Black dash line shows the ECR layer location. In (b), black dot line shows the o-mode cut-off density.

not changed by the changing of toroidal magnetic field direction as shown in Figure 5.45 (a). The plasma current direction depends on the poloidal field direction. The plasma current was changed to opposite direction by the opposite poloidal field coil direction. The absolute value of the plasma current was a little different for the toroidal coil direction. The plasma current on negative TF coil current is slightly higher than one on positive TF coil current. Even if it is caused by the EBWCD, the most of plasma current is driven other current driving source because the plasma current direction depends on the poloidal magnetic field direction. Thus, the pressure drive is a high candidate for driving source of the plasma current in this experiment.

The electron temperature and density profiles in HFS and LFS injections are also different as shown in Figure 5.46. In HFS injection, at the initial discharge not forming the closed flux surface at 21 ms, the electron temperature and density are much higher than those in LFS injection. The over-dense plasma was also observed in Figure 5.46 (b). The EBW heating causes the high-pressure plasma in case of open flux surface also. The direction of pressure driven current on the open flux surface depends on the poloidal magnetic field direction as a precession current ($j_{prec} \sim -p_e/RB_{p,o}$ where $B_{p,o}$ is poloidal field where the orbit crosses the mid-plane). In case of averaged electron temperature of 30 eV, density of 5×10^{17} m^{-3}, the precession current is 3 kA as similar as the experiment. In the close flux surface configuration, the bootstrap current also may drive the plasma current.

5.6 Conclusion

EBW heating was expected to heat more efficiently than ECRH without the cut-off density. However, EBW has to be mode converted from ECW. As fundamental physics experiment, the HFS X-mode injection took place expecting the highly efficient mode conversion. The comparison with LFS O-mode injection showed clear difference by EBW because the mode conversion to EBW is not expected. The higher plasma current and density were observed in HFS X-mode injection. The high RF absorption in HFS X-mode injection over 90 % was observed. The high RF absorption is one of EBW heating property.

To confirm the EBW excitation, the PDI measurement was performed. The PDW frequency of high frequency is approximately 8.1 GHz and one of low frequency is approximately 95 MHz. This PDW frequency was estimated the electron density profiles by the Thomson scattering measurement system on both injections. One of injection antennas in HFS was used to detect the high frequency PDW. The insertion and ECR probes were used to detect the low frequency PDW. In HFS X-mode injection, the high spectrum showing PDW through three-wave coupling by the EBW excitation was observed. In contrast, in LFS O-mode injection, the spectrum was not observed showing the EBW excitation. The PDI measurement showed the EBW excitation in HFS X-mode injection and led to a better understanding of the mode conversion to EBW.

The adjustment of decay index plays to form the closed flux surface in only case of HFS injection regardless the same magnetic field was applied in both injections. The higher decay index than or equal to 0.5 formed the closed flux surface in HFS injection. In initial part of plasma current start-up before forming the closed flux surface, the PDW showing the EBW excitation was observed. The non-inductive plasma current start-up by EBW heating was first demonstrated with $I_p \sim 4$ kA. The source of plasma current drive was investigated by changing the magnetic coil current direction, and it suggested the pressure drive. In fact, the pressure is high enough to drive the plasma current of 3 kA by precession current. It is considered that the formation of the closed flux surface was caused and maintained by the high pressure driven current by the EBW heating.

6. Summary

ST has a high advantage for the plasma confinement owing to the high beta. However, the inductive current drive does not work because of the small cross-section of CS coil. As one of non-inductive current drive, ECRH was demonstrated. However, ECRH cannot work for the higher density than the cut-off density. The plasma current start-ups by two methods of non-inductive current drive using RF to overcome the cut-off density of the fundamental ECRH were studied. One method is the second harmonic ECRH and another one is the EBW heating. Both methods demonstrated the higher electron density than the cut-off density of fundamental ECRH.

In the second harmonic ECRH, the oblique injection was supposed to induce the high Doppler shirt effect to couple with the high energy electron component and drive the high plasma current. In fact, the high plasma current ~ 60 kA was achieved. As the unique phenomena on second harmonic ECRH, the electron energy shift which shows the shift from the bulk electron heating to the tail electron heating was observed. It was cleared by the power balance calculation assuming multi-pass absorption that once the bulk electron cooling occurs, the negative feedback loop of bulk electron heating and the positive feedback loop of tail electron heating are induced. This is a cause of the electron energy shift. The difficulty to establish both bulk and tail electron heating which can obtain high plasma current and high electron temperature was shown. The possibility of occurrence of electron energy shift is also for the large tokamak devices. The tail electron heating might be serious problem in large tokamak devices from point of damage assessment. As future work, the selectivity of bulk electron heating and tail electron heating should be investigated. The operational selectivity is important to avoid the runaway discharge as result of the tail electron heating. The RF injection angle and polarization are the operation parameter for wave. The toroidal electric field should also adjust to control the high energy electron component.

X-mode HFS injection and O-mode LFS injection were demonstrated and the comparison of PDI measurement was on both proved the EBW excitation in X-mode HFS injection. The PDI spatial measurement was first in tokamak device and proved the EBW excitation. The X-mode HFS injection showed the high efficient RF absorption of over 90 % with EBW excitation and the high electron temperature of ~ 60 eV and over-dense of 1×10^{18} m^{-3}. The vertical field adjustment helped to form the closed flux surface. At vertical magnetic field of 2 mT and decay-index of 0.5, the closed flux surface was formed in HFS injection only. The pressure driven current due to high pressure by EBWH formed the closed flux surface. In this study, the plasma current start-up of 4 kA with EBWH was demonstrated first. High RF absorption efficiency in even low density is very attractive to plasma current start-up. Such highly efficient plasma start-up method does not exist in other method. The EBW current drive could not be demonstrated. The demonstration of EBWCD is a future work. The less of collision damping is important to drive EBWCD, so high plasma confinement should be

achieved with poloidal filed coil build-up with longer pulse discharge after equipping the cooling water channel with vacuum window.

The initial plasma current start-up was achieved in the both advanced RF heating methods. In second harmonic ECRH experiment, the plasma current ramp-up was demonstrated. In X-mode HFS injection experiment, the closed flux surface formation was observed.

By the study of plasma current start-up due to two different advanced RF heating methods, we could find the two common mechanisms of plasma current drive. A first point is that the pressure driven current as bootstrap current is dominant in the plasma start-up with efficient bulk electron heating. In the second harmonic ECRH experiment, it was concluded that the plasma current during the bulk electron heating of 12 kA was sustained by the pressure driven current. In the EBWH experiment, the plasma current of 4 kA was driven by pressure driven current. Second point is that the oblique injection is a key to drive the plasma current. In the second harmonic ECRH experiment, the plasma current of 60 kA was achieved in the tail electron heating. The plasma current is driven by the tail electron having parallel velocity which is resonated on Doppler shift ECR layer enhanced by the oblique injection. In the EBWH experiment, the EBWCD also should be driven by the resonant electron having parallel velocity on Doppler shift ECR layer, because the mode converted ray naturally become the parallel with magnetic field direction. Unfortunately, EBWCD was not observed in this experiment due to the RF absorption before reaching ECR layer by the strong damping. The most effective current drive may be accomplished in significant bulk electron heating by RF in oblique injection. The pressure driven current by bootstrap current is high and the plasma current by ECCD due to Doppler shift effect is also high. In second harmonic ECRH, the oblique injection may only cause the tail electron heating by finite Larmor radius effect, but in EBWH, the oblique injection naturally occurs and effectively heats the bulk electron. The suitable plasma current start-up should be established as the future work.

Acknowledgement

本研究実施の機会を与えてきただき、遂行にあたり細部に亘り多大な御指導を賜りました九州大学応用力学研究所教授　花田和明 博士に深甚な感謝の意を表します。

グリーンアジアプログラムの学生として大変お世話になりました、九州大学総合理工学府量子プロセス理工学専攻教授　内野喜一郎 博士に甚大なる謝意を表します。

本研究を進めるにあたり実験、解析に至るまで多大な御協力と御助言を頂きました九州大学応用力学研究所教授　出射浩 博士に深く感謝の意を表します。

本研究を遂行するにあたり解析プログラムの提供、論文執筆の御助言、共同研究の機会を賜りましたプリンストン大学プラズマ物理研究所教授　小野雅之 博士に深く謝意を表します。

研究、実験を進める上で有益な御助言と、多大な協力を頂きました九州大学応用力学研究所教授　井戸毅 博士、同特任教授　同准教授　永島芳彦 博士、同准教授　池添竜也 博士、同助教　長谷川真 博士、同助教　恩地拓己 博士、同特任助教　黒田賢剛 博士、中村一男博士、吉田直亮 博士に深く感謝致します。

実験遂行において、多くの技術的な御助言と御協力くださいました九州大学応用力学研究所の技術職員　東島亜紀氏、永田貴弘氏、島袋瞬氏、また同高温プラズマ理工学センターのテクニカルスタッフ　河野香 氏、川崎昌二 氏、山下雅典 氏、石村吉雄 氏、馬場賢哉 氏に大変感謝致します。

電子温度・密度を観測するトムソン散乱計測で東京大学准教授　江尻晶 博士をはじめとする研究グループ、分光計測で京都大学准教授　四竈泰一 博士をはじめとする研究グループ、ジャイロトロン開発で筑波大学プラズマ研究センター教授　假家強 博士をはじめとする研究グループ、光線軌道解析でプリンストン大学プラズマ物理研究所Nicola Bertelli 博士、共同研究にてプリンストン大学物理研究所 Roger Raman 博士、Luis Delgado-Aparicio 博士、高周波プローブ計測で九州大学応用力学研究所教授　稲垣滋 博士の多大な御協力に厚く感謝致します。

九州大学・高温プラズマ理工学センター会議の外部コーディネーターである東京大学教授　高瀬雄一 博士、京都大学教授　村上定義 博士より多くの御助言、御議論を頂きましたこと感謝致します。

研究生活では大変お世話になりました、Hatem Elserafy 博士、Huang Canbin　博士、Liu Yukai 博士、福山雅治 氏、岳其霖 氏、村上貴洋 氏、木谷彰彦 氏、平中芳樹 氏、加藤凌哉 氏、工藤倫大 氏、平賀涼輔 氏、武田康佑 氏をはじめとする学生の皆様には多くの御協力を頂きました。感謝の意を表します。

円滑な研究活動、学生生活のため、事務補佐員の浦野由紀枝 氏、山口香織 氏、南里裕子氏、江島和美 氏、吉永小百合 氏、土橋美佐子 氏に大変感謝致します。

本研究の一部は日本学術振興会科学研究費（特別研究員奨励費 19J12290）によりました。

最後に、私を支えて下さいました妻、家族に感謝の意を示させて頂きます。

Reference

[1] J. Wesson, *Tokamaks*. Oxford Univ. Press, (2011).

[2] M. Ichimura *et al.*, Plasma Phys. Reports, **28**, 9, (2002).

[3] Y. K. M. Peng, Phys. Plasmas, **7**, 5 II, (2000).

[4] S. M. Kaye *et al.*, Nucl. Fusion, **45**, 10, (2005).

[5] R. Raman *et al.*, Phys. Rev. Lett., **90**, 7, (2003).

[6] M. Uchida *et al.*, J. Plasma Fusion Res., **80**, 2, (2004).

[7] A. Ejiri *et al.*, "RF start-up and sustainment experiments on the TST-2@K spherical tokamak," in *Nuclear Fusion*, (2006), **46**, 7, pp. 709–713.

[8] K. HANADA *et al.*, Plasma Sci. Technol., **13**, 3, (2011).

[9] K. Hanada *et al.*, .

[10] K. Hanada *et al.*, Nucl. Fusion, **57**, 12, (2017).

[11] H. Miura *et al.*, Plasma Fusion Res., **10**, (2015).

[12] T. Kariya *et al.*, Nucl. Fusion, **55**, 9, (2015).

[13] H. Idei *et al.*, Nucl. Fusion, **57**, 12, (2017).

[14] R. Raman *et al.*, Phys. Plasmas, **11**, 5 PART 2, (2004).

[15] R. Raman *et al.*, Phys. Plasmas, **18**, 9, (2011).

[16] K. Kuroda *et al.*, Plasma Phys. Control. Fusion, **60**, 11, (2018).

[17] G. L. Jackson *et al.*, Nucl. Fusion, **51**, 8, (2011).

[18] S. Coda *et al.*, Plasma Phys. Control. Fusion, **42**, 12 SUPPL. B, (2000).

[19] K. Hanada *et al.*, Plasma Sci. Technol., **13**, 3, (2011).

[20] S. Shiraiwa *et al.*, Phys. Rev. Lett., **92**, 3, (2004).

[21] T. Wakatsuki *et al.*, Nucl. Fusion, **54**, 9, (2014).

[22] R. Raman *et al.*, Phys. Rev. Lett., **104**, 9, (2010).

[23] M. Ono *et al.*, Phys. Rev. Lett., **59**, 19, (1987).

[24] J. M. Perry *et al.*, Nucl. Fusion, **58**, 9, (2018).

[25] Y. Ono *et al.*, Plasma Phys. Control. Fusion, **54**, 12, (2012).

[26] M. Inomoto *et al.*, Nucl. Fusion, **59**, 8, (2019).

[27] Y. S. Bae *et al.*, Nucl. Fusion, **49**, 2, (2009).

[28] J. A. Bittencourt, *Fundamentals of plasma physics*, 3rd ed. Springer.

[29] V. Erckmann *et al.*, Plasma Phys. Control. Fusion, **36**, 12, (1994).

[30] R. Prater, Phys. Plasmas, **11**, 5 PART 2, (2004).

[31] N. J. Fisch *et al.*, **45**, 9, (1980).

[32] T. Ohkawa, Nucl. Fusion, **10**, 2, (1970).

[33] T. Ohkawa, Gen. At. Rep., **GA-A13847**, (1976).

[34] I. B. Bernstein, Phys. Rev., **109**, 1, (1956).
[35] F. W. Crawford *et al.*, J. Appl. Phys., **36**, 9, (1965).
[36] T. H. Stix, *Waves in plasmas*. American Institute of Physics Inc., (1992).
[37] H. P. Laqua, Plasma Phys. Control. Fusion, **49**, 4, (2007).
[38] F. S. McDermott *et al.*, Phys. Fluids, **25**, 9, (1982).
[39] H. Igami *et al.*, Nucl. Fusion, **49**, 11, (2009).
[40] V. F. Shevchenko *et al.*, EPJ Web Conf., **87**, (2015).
[41] V. Shevchenko *et al.*, Phys. Rev. Lett., **89**, 26, (2002).
[42] H. P. Laqua, Plasma Phys. Control. Fusion, **49**, 4, (2007).
[43] S. Shiraiwa *et al.*, Phys. Rev. Lett., **96**, 18, (2006).
[44] M. Uchida *et al.*, EPJ Web Conf., **87**, 2006, (2015).
[45] J. Preinhaelter *et al.*, J. Plasma Phys., **10**, 1, (1973).
[46] J. Preinhaelter, Czechoslov. J. Phys., **25**, 1, (1975).
[47] H. Weitzner *et al.*, Phys. Fluids, **22**, 7, (1979).
[48] E. Mjølhus, J. Plasma Phys., **31**, 1, (1984).
[49] F. R. Hansen *et al.*, J. Plasma Phys., **39**, 2, (1988).
[50] H. P. Laqua *et al.*, Phys. Rev. Lett., **78**, 18, (1997).
[51] H. Igami *et al.*, Rev. Sci. Instrum., **77**, 10, (2006).
[52] A. Mueck *et al.*, Phys. Rev. Lett., **98**, 17, (2007).
[53] M. Porkolab *et al.*, Rev. Mod. Phys., **50**, 4, (1978).
[54] R. C. Davidson, *Methods in Nonlinear Plasma Theory*. Academic Press, (1972).
[55] M. Okabayashi *et al.*, Phys. Rev. Lett., **31**, 18, (1973).
[56] M. Henderson *et al.*, Phys. Plasmas, **22**, 2, (2015).
[57] T. Kobayashi *et al.*, Nucl. Fusion, **55**, 6, (2015).
[58] Y. S. Bae *et al.*, Nucl. Fusion, **49**, 2, (2009).
[59] H. Tanaka *et al.*, Nucl. Fusion, **31**, 9, (1991).
[60] H. Idei *et al.*, "Noninductive Electron Cyclotron Heating and Current Drive with Dual Frequency (8.2{28 GHz) Waves in QUEST," in *IAEA FEC 2016*, (2016), p. EX/P4-50.
[61] H. Idei *et al.*, Fusion Eng. Des., **146**, October 2018, (2019).
[62] K. Mishra *et al.*, Nucl. Fusion, **55**, 8, (2015).
[63] T. Yamaguchi *et al.*, Plasma Fusion Res., **8**, 2013, (2013).
[64] M. Hasegawa *et al.*, Fusion Eng. Des., **88**, 6–8, (2013).
[65] M. Ono *et al.*, 6TH Int. Conf. Biol. Sci. ICBS 2019 "Biodiversity as a Cornerstone Embrac. Futur. Humanit., **2260**, September, (2020).
[66] C. B. Forest *et al.*, Phys. Plasmas, **1**, 5, (1994).
[67] S. Tashima *et al.*, Nucl. Fusion, **54**, 2, (2014).

[68] S. M. Kaye *et al.*, Nucl. Fusion, **37**, 9, (1997).

[69] K. Hanada *et al.*, Plasma Sci. Technol., **18**, 11, (2016).

[70] R. A. Cairns *et al.*, Phys. Plasmas, **7**, 10, (2000).

[71] A. Pochelon *et al.*, Nucl. Fusion, **47**, 11, (2007).

[72] A. P. Smirnov *et al.*, Bull Amer. Phys. Soc., **39**, 7, (1994).

[73] R. Yoneda *et al.*, Plasma Fusion Res., **13**, (2018).

[74] T. Maekawa *et al.*, Phys. Rev. Lett., **86**, 17, (2001).

[75] H. Elserafy *et al.*, Plasma Fusion Res., **14**, (2019).

[76] A. T. Lin *et al.*, "Nonlinear penetration of upper-hybrid waves induced by parametric instabilities of a plasma in an inhomogeneous magnetic field," Wiley, (1981).

[77] A. J. Cohen *et al.*, Phys. Fluids, **14**, 7, (1971).

[78] C. B. Forest *et al.*, Phys. Plasmas, **1**, 5, (1994).

[79] M. Uchida *et al.*, Nucl. Fusion, **51**, 6, (2011).

[80] T. Yoshinaga *et al.*, Phys. Rev. Lett., **96**, 12, (2006).

Appendix

I. Bulk electron temperature and density distribution

The measured temperature and density distribution by Thomson scattering measurement were used for the bulk electron distribution to simulate the experiment. Usually, the polynomial fitting is used for fitting distribution, however, the polynomial fitting could not fit reliable distribution which showed negative value in distribution. The natural logarithm fitting was developed to fit original distribution. This fitting function can fit within the plasma size determined by EFIT. The fitting function is Eq.53. x_{in} and x_{out} show the inside and outside location of the plasma. This original natural logarithm fitting function could interpolate well than polynomial fitting as shown in Figure 47.

$$y = \frac{y_1 y_2}{y_1 + y_2} \tag{53}$$

$$y_1 = k_1\{(1 - e^{-a(x-x_{s1})}) - (1 - e^{-a(x_{in}-x_{s1})})\}$$

$$y_2 = k_2\{(e^{-b(x-x_{s2})}) - (e^{-b(x_{out}-x_{s2})})\}$$

The interpolated distribution by original natural logarithm was given as the bulk electron distribution for raytracing.

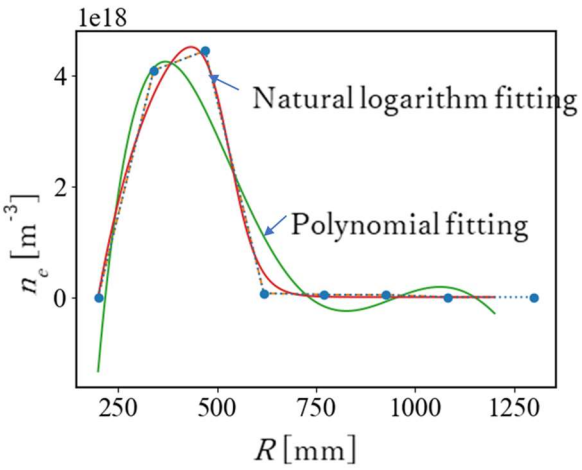

Figure 47.. The fitting function for density distribution measured by Thomson scattering system. Blue dots show the measured value. A green line shows the polynomial fitting line. A red line shows the original natural logarithm fitting.

II. Bremsstrahlung by estimated tail electrons

The accuracy of estimated tail electron temperature and density was evaluated by the bremsstrahlung intensity including relativistic effect. The bremsstrahlung emissivity for the arbitrary injection electron energy and emitted photon energy can be written in Eq. 54.

$$W(E_0,k) = kn_e(E_0)n_i v_0 \left\langle \frac{d\sigma(E_0,k,\theta_0)}{dkd\Omega_k} \right\rangle \qquad 54$$

E_0 is injection electron energy, k, $\boldsymbol{k}$ are emitted photon energy and momentum, n_e is the number of electrons on the injection electron energy and the electron distribution is assumed relativistic Maxwellian distribution for $T_{e\,tail}$ and $n_{e\,tail}$, n_i is the number of ions, v_0 is the injection electron velocity, Ω_k is element of solid angle in direction of $\boldsymbol{k}$, θ_0 is the angle of $\boldsymbol{v}_0$ with respect to $\boldsymbol{k}$. The unit bremsstrahlung cross section for the unit emitted photon energy and the unit solid angle $\frac{d\sigma(E_0,k,\theta_0)}{dkd\Omega_k}$ including relativistic effect was given from H.W. Koch, et al. (Formula 2BN in [A]). The cross section was averaged on the angle θ_0 from 0 to 90 degree to assume the forward emission as $\left\langle \frac{d\sigma(E_0,k,\theta_0)}{dkd\Omega_k} \right\rangle$.

$$\begin{aligned}\frac{d\sigma(E_0,k,\theta_0)}{dkd\Omega_k} = \frac{Z^2 r_0^2}{8\pi 137}\frac{1}{k}\frac{p}{p_0}\Bigg\{ & \frac{8\sin^2\theta_0(2E_0^2+1)}{p_0^2\Delta_0^4} - \frac{2(5E_0^2+2EE_0+3)}{p_0^2\Delta_0^2} - \frac{2(p_0^2-k^2)}{Q^2\Delta_0^2} \\ & + \frac{4E}{p_0^2\Delta_0} \\ & + \frac{L}{pp_0}\Bigg[\frac{4E_0\sin^2\theta_0(3k-p_0^2E)}{p_0^2\Delta_0^4} \\ & + \frac{4E_0^2(E_0^2+E^2)+2-2(7E_0^2-3EE_0+E^2)}{p_0^2\Delta_0^2} + \frac{2k(E_0^2+EE_0-1)}{p_0^2\Delta_0}\Bigg] \\ & - \left(\frac{4\epsilon}{p\Delta_0}\right) + \left(\frac{\epsilon^Q}{pQ}\right)\left[\frac{4}{\Delta_0^2} - \frac{6k}{\Delta_0} - \frac{2k(p_0^2-k^2)}{Q^2\Delta_0}\right]\Bigg\}\end{aligned} \qquad 55$$

$$L = \ln\left[\frac{E_0E + p_0p - 1}{E_0E - p_0p - 1}\right]$$

$$\Delta_0 = E_0 - p_0\cos\theta_0$$

$$\epsilon = \ln\left[\frac{E+p}{E-p}\right]$$

$$\epsilon^Q = \ln\left[\frac{Q+p}{Q-p}\right]$$

$$E = E_0 - k$$

$$Q^2 = {p_0}^2 + k^2 - 2p_0k\cos\theta_0$$

where E_0, E are the initial and final total energy of the electron in a collision, in m_0c^2 [erg] unit. T_0, T are initial and final kinetic energy of the electron in a collision, in m_0c^2 [erg] unit. $\boldsymbol{p}_0$, $\boldsymbol{p}$ are initial and final momentum of the electron in a collision, in m_0c [g*cm/s] unit. k, $\boldsymbol{k}$ are energy and momentum of the emitted photon, in m_0c^2 [erg] and m_0c [g*cm/s] unit. θ_0, θ are angles [rad] of $\boldsymbol{p}_0$ and $\boldsymbol{p}$ with respect to $\boldsymbol{k}$. $d\Omega_k$ is element of solid angle, $\sin\theta d\theta d\phi$, in the direction of $\boldsymbol{k}$. Z is atomic number of

target material. r_0 is classical electron radius 2.82×10^{-13} cm. The initial and final total energy are written by the initial and final kinetic energy of the electron as $E_0 = 1 + T_0$, $E = 1 + T$. The Lorentz factors are given as $\gamma_0 = E_0/m_0c^2$, $\gamma = E/m_0c^2$. The velocities are $v_0 = c\sqrt{\frac{\gamma_0^2-1}{\gamma_0}}$, $v = c\sqrt{\frac{\gamma^2-1}{\gamma}}$. The momentums are written as $p_0 = \gamma_0 v_0/c$, $p = \gamma v/c$.

The example of cross sections for the injection energy with 50 keV and 500 keV are shown in Figure 48. The cross section for lower photon energy is larger than one for higher photon energy in case of same injection electron energy. Front and back emission are seen in the injection electron energy with 50 keV. The cross section by electron having stronger injection energy emits more narrower emission having the directivity.

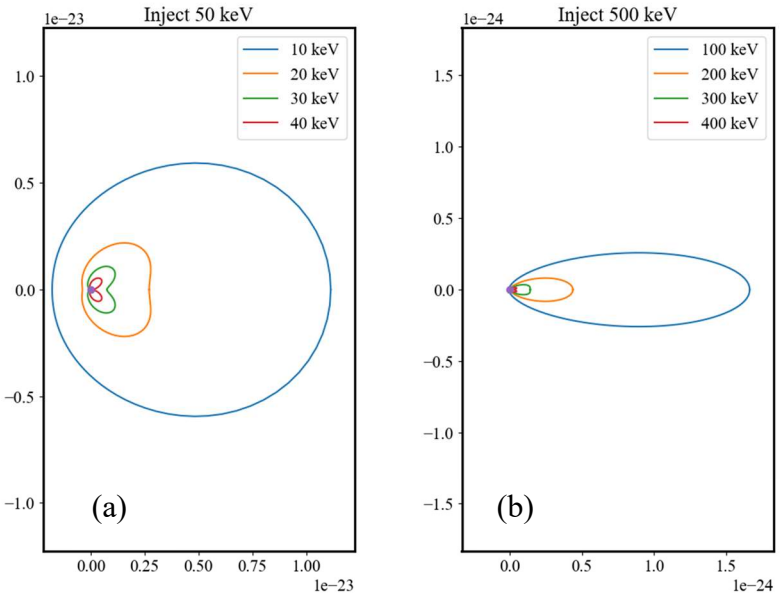

Figure 48. The bremsstrahlung cross sections for each emission energy caused by the injection energy (a) 50 keV and (b) 500 keV.

The bremsstrahlung emissivity on each the emitted photon is given as Eq. 56.

$$W(E_0, k, \theta_0) = kn_e(E_0)n_i v_0 \frac{d\sigma(\theta_0)}{dkd\Omega_k} \qquad 56$$

where k is the emitted photon energy, n_e is the electron density, n_i is the ion density, v_0 is the electron velocity, $\frac{d\sigma(\theta_0)}{dkd\Omega_k}$ is the cross section. The electron density was given by the relativistic Maxwellian

distribution [B] as Eq. 57.

$$n_e(E_0) = n_{e0} C \int e^{-\left(\frac{mc^2}{T}\right)\gamma_0} dv_0 \quad 57$$

$$C = \frac{\frac{mc^2}{T}}{4\pi(mc)^3 K_2\left(\frac{mc^2}{T}\right)} = \frac{1}{2\int_0^\infty e^{-\left(\frac{mc^2}{T}\right)\gamma_0} dv_0}$$

where $K_2\left(\frac{mc^2}{T}\right)$ denotes modified Bessel function. The difference between non-relativistic Maxwellian distribution and relativistic Maxwellian distribution is shown in Figure 49.

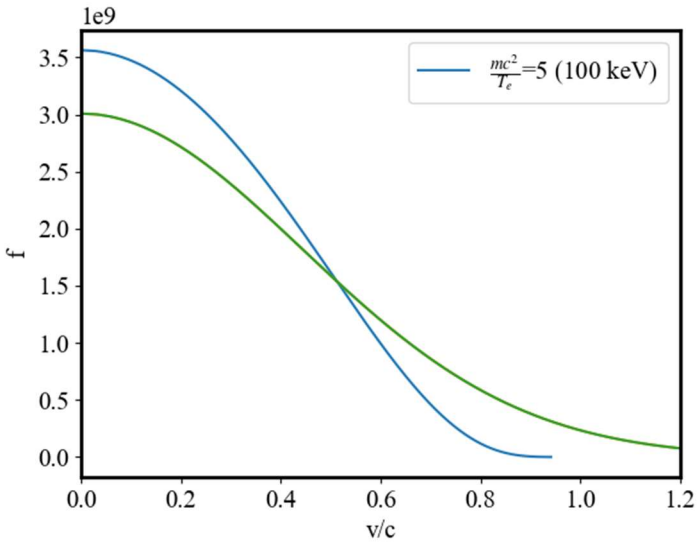

Figure 49. The non-relativistic Maxwellian distribution and relativistic Maxwellian distribution. The electron density is 1×10^{18} m^{-3} and electron temperature 100 keV.

The bremsstrahlung intensity on the certain photon energy for the impacting electron energy is integrated with the impacting electron energy, and obtained the bremsstrahlung intensity on the certain photon energy as shown in Eq. 58. The integrated bremsstrahlung intensity as function of photon energy is the bremsstrahlung intensity for electron temperature T_e as Eq. 59. The measurable intensity is restricted by the measurable energy range of CdTe detector. The energy range was set from 25 keV to 400 keV.

$$W(k) = \int W(E_0, k) dE_0 \quad 58$$

$$W(T_e) = \int W(k) dk \quad 59$$

$$W_{measure}(T_e) = \int_{25\ keV}^{400\ keV} W(k)dk \qquad 60$$

The total bremsstrahlung intensity $W(T_e)$ is given as Figure 50. The measurable HXR intensity $W_{measure}(T_e)$ is an integrated region described by the hatch area. The absolute value of measured HXR intensity is difficult to evaluate because of unknown solid angle by collimator size and the line of sight length. However, the tendency of bremsstrahlung intensity for the tail electron temperature and density is estimable. To assess the measured bremsstrahlung intensity, the cross section was averaged on the angle θ_0 from 0 to 45 degree to assume the forward emission as $\left\langle \frac{d\sigma(E_0,k,\theta_0)}{dkd\Omega_k} \right\rangle$.

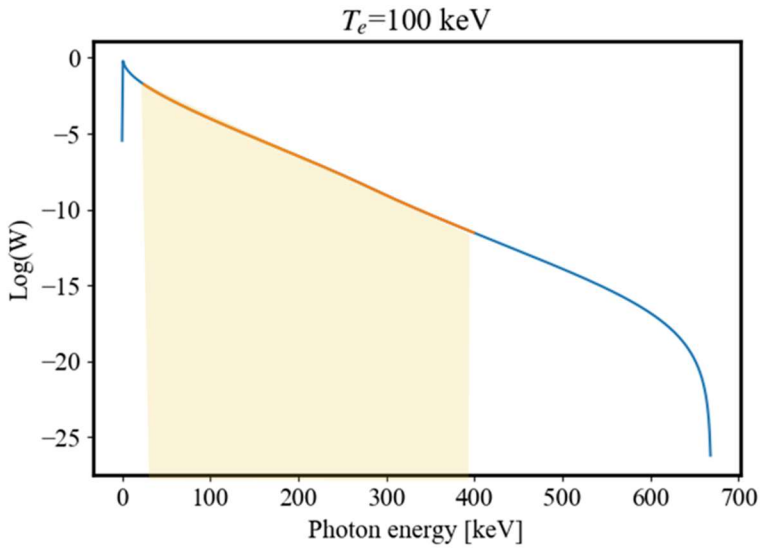

Figure 50. The bremsstrahlung intensity for the electron temperature and the measurable region. The electron temperature is 100 keV. The orange shadow shows the integrated area to estimate the bremsstrahlung emission.

III. Collision time and Confinement time

The power by energy relaxation though Coulomb collision as $P_{tail\to bulk}$, P_{eibulk} , P_{eitail} can be calculated as Eq. 61. The image of the energy relaxation is that running test particle collide to other bulk body.

$$P_{t\to j} = \frac{3}{2} e n_j \frac{T_t - T_j}{\tau_t^{tj}} \qquad 61$$

$$\tau_t^{tj} = \frac{3\sqrt{2\pi}\pi\varepsilon_0^2 m_t m_j}{n_j Z_j^2 Z_t^2 e^4 \ln\Lambda}\left(\frac{T_t}{m_t} + \frac{T_j}{m_j}\right)^{\frac{3}{2}}$$

where subscripts t, j show the test particle and the bulk body. T_t, T_j are temperature in unit eV. n_j is the density of the bulk body in unit m^{-3}. Z is the charge number. e is charge in unit J. m is the mass in unit kg. $\ln\Lambda$ is Coulomb logarithm. The Coulomb logarithm in case of electron-electron collision is shown in Eq. 62.

$$ln\Lambda = 8.3 + 2.3\log_{10}\frac{T_e}{\sqrt{n_e/10^{20}}} \quad 62$$

The actual electron-neutral collision has complex process such as the ionization, excitation for various kinds of atom and the dissociation for molecular. As simple discussion, the ionization of hydrogen from ground state was considered. The collisional cross section of the ionization and the excitation of hydrogen atom are summarized by Janev, et al [C]. The collisional cross section from the ground state is shown in Figure 52. We assumed the energy loss by one collision time is 13.6 eV for the ionization from ground state. The electron-neutral particle collision time is given by Eq. 64.

$$P_{en} = \frac{W_{stored\ energy}}{\tau_{en}} \quad 63$$

$$\tau_{en} = \frac{T_e}{13.6\ [eV]}\tau_{en\_1state} \quad 64$$

$$\tau_{en-1state} = \frac{1}{n_n\langle\sigma_{1s}v\rangle}$$

$$\langle\sigma_{1s}v\rangle = \frac{1}{n_e}\int \sigma_{1s}v f(v)dv$$

P_{en} was given by the division of the stored energy by the electron-neutral particle collision time. $\tau_{en-1state}$ is the electron-neutral collision time by a collision. The collisional cross section was the function of energy. The cross section has to be the averaged cross section for the velocity of the function of electron temperature as $\langle\sigma_{1s}v\rangle$. If the electron temperature is less than 13.6 eV, the collisional cross section is estimated due to the existence of the higher energy electron than 13.6 eV on the Maxwellian distribution as shown in Figure 51. In the low electron temperature, it also be calculated the power loss by the electron-neutral particle collision. The power loss $P_{E\ bulk}$ for not relating with electron collision was given by the global energy confinement time scaling. The global energy confinement time was used the L-mode scaling given by Kaye, et al [68].

$$P_{E\ bulk} = \frac{W_{stored\ energy}}{\tau_{\ ITER89-p}} \quad 65$$

$$\tau_{ITER89-p} = 0.038 I_p^{0.85} R^{1.5} (R/a)^{-0.3} \kappa^{0.5} \bar{n}_e^{0.1} B_T^{0.5} M_{eff}^{0.5} P^{-0.5}$$

The plasma current I_p and line averaged density $\bar{n}_e$ were given by the measurement value. The plasma formation was given by the EFIT code simulation. B_T = 0.25 T, κ = 1.3, M_{eff} = 1 AMU were set.

$P_{E\,tail} = \frac{W_{stored\ energy}}{\tau_{E\,tail}}$ is tail electron power loss. In 8.2 GHz ECRH experiment, the power loss deposited on the limiter was ~ 20 kW, and the stored energy of the tail electron was ~ 200 J, so the confinement time should be $\tau_{E\,tail}$~ 10 ms.

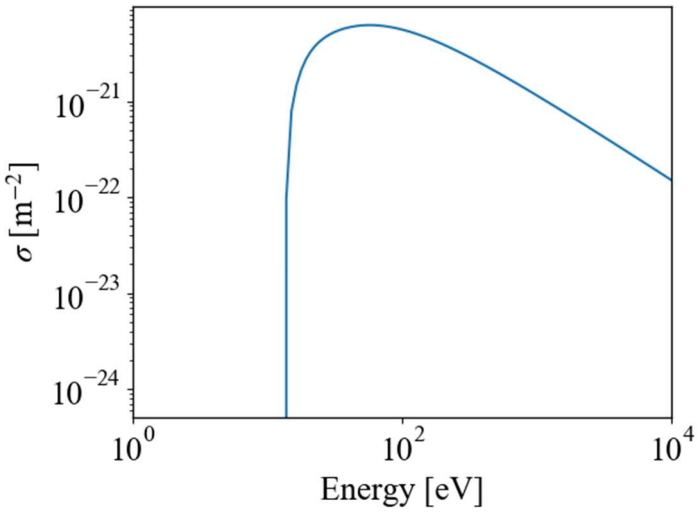

Figure 52. The electron impact ionization cross section from ground state.

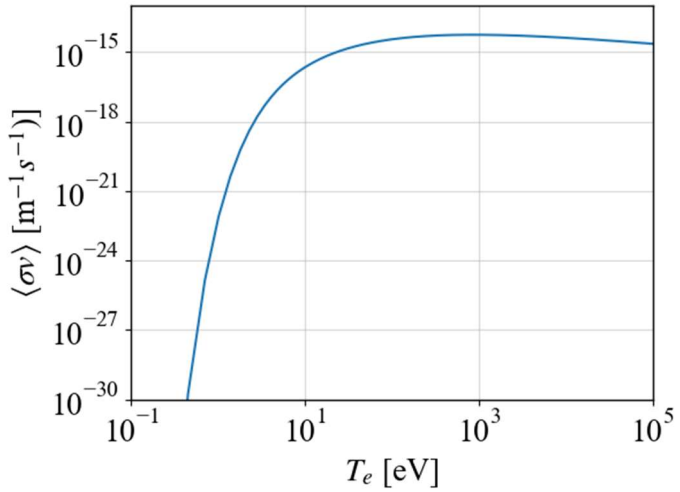

Figure 51. The averaged electron impact ionization cross section from ground state for the electron

IV. Multi-pass process

The multi-pass process was considered as Eq. 4.4. The first important part is the absorption rate of η_{tail}, η_{bulk} for tail and bulk electron thorough the single-pass process. The single-pass absorption was calculated with averaged injection angle of $N_{||}$ = 0.5. The color map showing the absorption rate of η_{tail}, η_{bulk} on each tail electron temperature and density is shown in figure IV-1. The satisfying part of the stored energy shows the absorption rate of η_{tail}, η_{bulk} is approximately 1:1. The second consideration is the absorption rate of $P_{RF\,tail}$, $P_{RF\,bulk}$ by multi-pass absorption which is obtained by the satisfaction of power balance. The color map showing the absorption rate of $P_{RF\,tail}$, $P_{RF\,bulk}$ on each tail electron temperature and density is shown in figure IV-2. The absorption rate of $P_{RF\,tail}$, $P_{RF\,bulk}$ should be same with the absorption rate of η_{tail}, η_{bulk} to be 1:1. The tail electron temperature of 2 keV and density of 6 % of bulk electron density satisfy the stored energy and the absorption rate of 1:1 on the multi-pass process and the single-pass process.

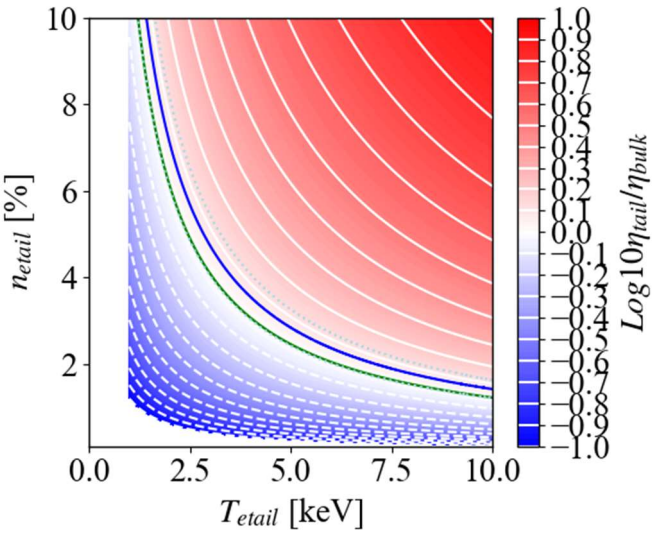

Figure IV-1: The color map of absorption rate of η_{tail}, η_{bulk} thorough single-pass absorption with $N_{||}$ = 0.5 to assume multi-pass reflection. The blue line and blue dot line show the stored energy by EFIT and 10 % error of the stored energy. The green line shows the same absorption amount for tail and bulk electron that is the absorption rate of η_{tail}, η_{bulk} of 1:1.

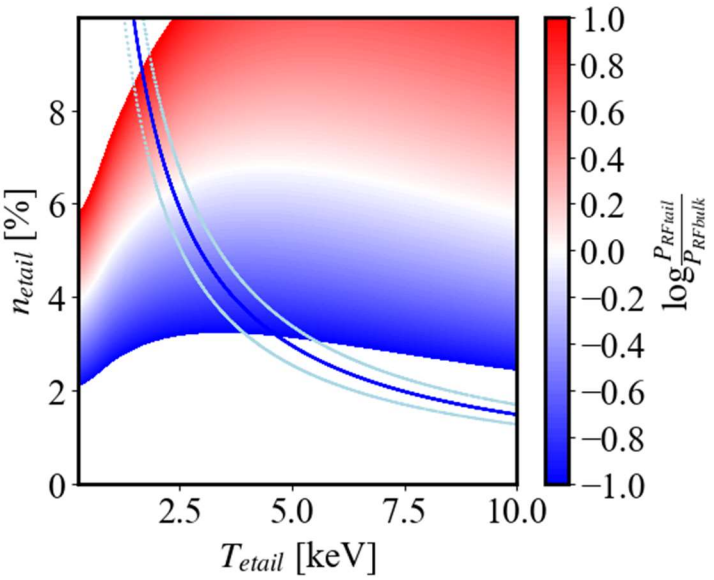

Figure IV-2: The color map of absorption rate of $P_{RF\,tail}$, $P_{RF\,bulk}$ thorough multi-pass absorption. The blue line and light blue line show the stored energy by EFIT and 10 % error of the stored energy.

V. Magnetic field calculation

The vector potential was defined by Eq. V-1 [D].

$$A_\varphi = \frac{\mu_0 I}{4\pi} \oint \frac{dl}{L} \tag{V-1}$$

The cylinder coordination was used to estimate the vector potential as shown in Figure V-1. The vector potential considered the geometry was written by Eq. V-2.

$$A_\varphi = \frac{\mu_0 I}{2\pi} \int_0^{2\pi} \frac{R\cos\theta\, d\theta}{\sqrt{R^2 + r^2 + z^2 - 2rR\cos\theta}} \tag{V-2}$$

where R is the radius of coil. r and z are the radius and height of estimated vector potential. I is the coil current. The Eq. V-2 was modified by $\theta = \pi - 2\psi$, $k^2 = \frac{4Rr}{(R+r)^2+z^2}$ to Eq. V-3 and Eq. V-4.

$$A_\varphi = \frac{\mu_0 I}{2\pi} \sqrt{\frac{R}{r}} k \int_0^{\pi/2} \frac{2sin^2\psi - 1 d\psi}{\sqrt{1 - k^2 sin^2\psi}} \tag{V-3}$$

$$A_\varphi = \frac{\mu_0 I}{2\pi} \sqrt{\frac{R}{r}} k \int_0^{\pi/2} \left\{ \frac{1 - {k^2}/{2}}{\sqrt{1 - k^2 sin^2\psi}} - \sqrt{1 - k^2 sin^2\psi} \right\} d\psi \tag{V-4}$$

Eq. V-4 can be re-written in terms of the complete elliptic integrals of the first and second kind as

$K(k) = \int_0^{\pi/2} \frac{1}{\sqrt{1-k^2 sin^2\psi}} d\psi$, $E(k) = \int_0^{\pi/2} \sqrt{1-k^2 sin^2\psi}\, d\psi$ as Eq. V-5.

$$A_\varphi = \frac{\mu_0 I}{2\pi} \sqrt{\frac{R}{r}} \left\{ \left(1 - {k^2}/{2}\right) K(k) - E(k) \right\} \quad \text{V-5}$$

The vertical magnetic field of B_r and B_z can be written as Eq. V-6 and Eq. V-7.

$$B_r = -\frac{\partial A_\varphi}{\partial z} = \frac{\mu_0 I}{2\pi} \frac{z}{r\sqrt{(R+r)^2 + z^2}} \left[-K + \frac{R^2 + r^2 + z^2}{(R-r)^2 + z^2} E \right] \quad \text{V-6}$$

$$B_z = \frac{1}{r}\frac{\partial}{\partial r}(rA_\varphi) = \frac{\mu_0 I}{2\pi} \frac{z}{\sqrt{(R+r)^2 + z^2}} \left[K + \frac{R^2 - r^2 - z^2}{(R-r)^2 + z^2} E \right] \quad \text{V-7}$$

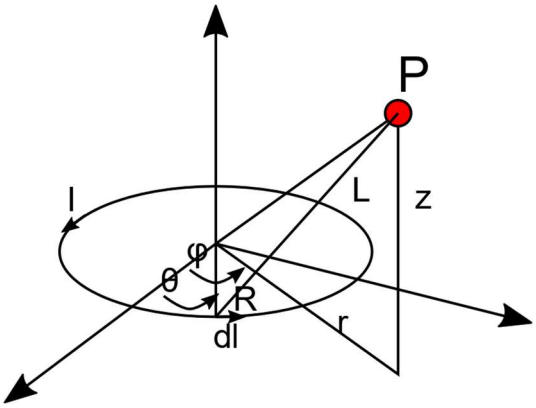

Figure V-1: The geometry to estimate vector potential.

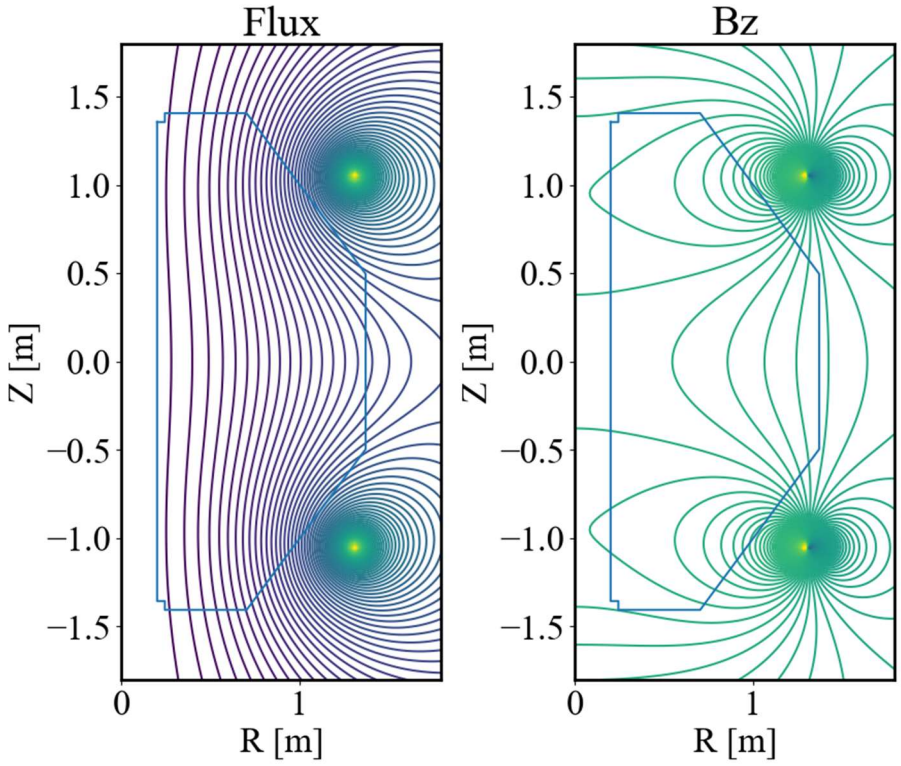

Figure V-253: The contours of flux and vertical magnetic field for z direction with PF 2-6 coil current 0.1 kA.

The flux $\Phi = \oint \vec{A}\, dl = 2\pi R A_{\varphi}$ and B_z can be estimated by the poloidal coil currents with PF 2-6 of 0.1 kA as shown in Figure IV-2. The decay index was based on the estimated B_z.

VI. Investigation of closed flux surface on PDI measurement

The impact of the probe does not affect for a whole of plasma formation. If the closed flux surface were formed, the probe insertion would interrupt particles on same flux surface surrounding the magnetic axis causing a large impact on the plasma parameters [E].

The spontaneous current jump is the one of feature showing the bridges from the open flux surface to the closed flux surface [F]. The vertical magnetic field to maintain the plasma loop in equilibrium is given by the Shafranov formula.

$$B_v = \frac{\mu_0 I_p}{4\pi R}\left(\ln\frac{8R}{a} + \frac{l_i}{2} - \frac{3}{2} + \beta_p\right) \qquad \text{VI-1}$$

where $l_i = \ln(1.65 + 0.89\upsilon)$ is the self-inductance, $\upsilon = q_a/q_0 - 1$, q_a and q_0 are the safety factors at the edge and center of plasma, $\beta_p = 2\mu_0\langle p\rangle/B_a^2 = 8\pi^2 a^2\langle p\rangle/\mu_0 I_p^2$ is the beta poloidal. The no observation of the spontaneous current jump indicates keeping the open flux surface. To discuss whether the exist or not the spontaneous current jump, the same normalized formula should be used.

$$\overline{B_v} = \left(\ln\frac{8R}{a} + \frac{l_i}{2} - \frac{3}{2}\right)\overline{I_p} + \frac{1}{\overline{I_p}} \qquad \text{VI-2}$$

where $\overline{B_v} = \sqrt{\frac{2}{\mu_0}}\frac{(R/a)B_v}{\sqrt{\langle p\rangle}}$, and $\overline{I_p} = \sqrt{\frac{\mu_0}{8}}\frac{I_p}{\pi a\sqrt{\langle p\rangle}}$. The first term is proportional to the plasma current

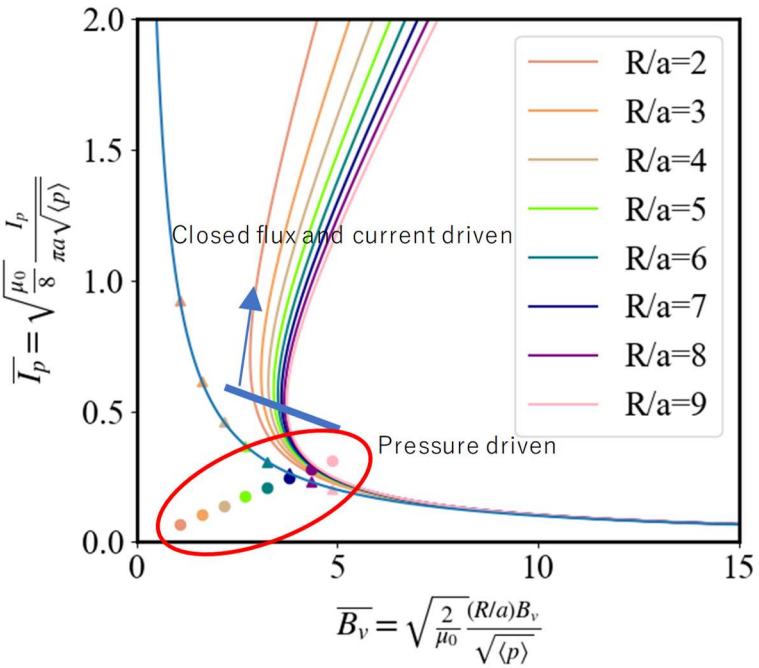

Figure VI-1: The figure is showing the equilibrium plasma current and the vertical magnetic field by calculation based on Eq. VI-2. The measured current is marked by circle points. The measured current is in the pressure driven regime.

showing the characteristic term of the closed flux surface. The second term is inversely proportional to the plasma current showing the open flux surface.

The pressure was calculated by the T_e and n_e profiles as measured using Thomson scattering. The measured plasma currents are marked on Figure . The observed plasma current was relevant to the pressure driven current in the open magnetic flux surface estimated. The evidence for the formation of a closed flux surface was not obtained. Therefore, the difference in I_p did not play a role in the modification of the magnetic surface. The PDW measurement was carried out in the open flux surface. The plasma parameters are regarded as the same plasma due to no observation of the large different on each discharge.

VII. Estimation of electron density and temperature on PDW measurement

The UHR layer location and the PDW frequency was estimated from the measured electron density profiles by Thomson scattering measurement. The simultaneous measurement with PDW

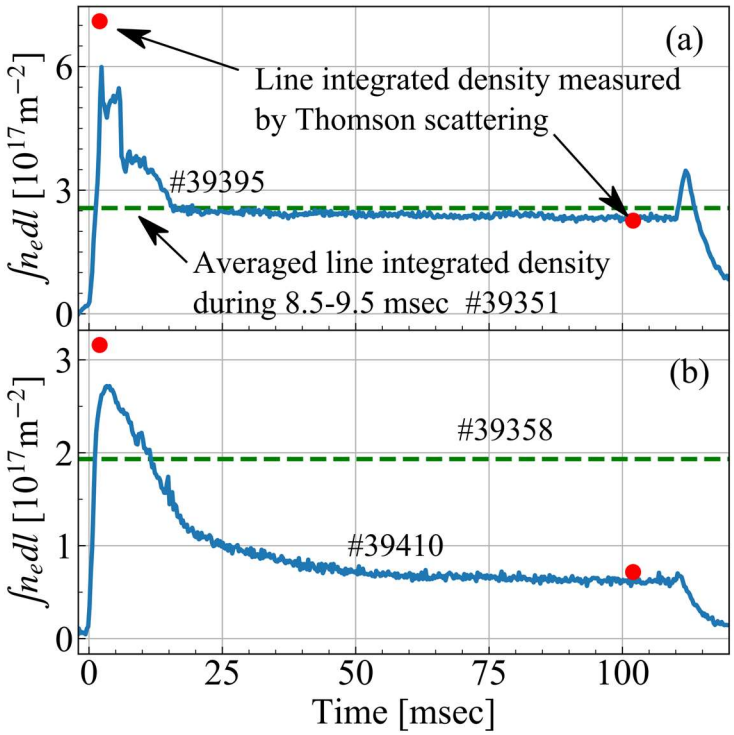

Figure VII-1: Time evolution of the line-integrated density 110 msec discharge for (a) the HFS injection (#39395) and (b) the LFS injection (#39410) are drawn by the blue lines. The line-integrated densities calculated on n_e profiles measured with Thomson scattering measurement were marked by the red points. The green dot lines show averaged line-integrated density during 8.5–9.5 msec in 10 msec discharges (HFS: # 39351, LFS: #39358).

measurement and Thomson scattering measurement could not be performed. The line integrated electron density was measured in both measurements. The PDW measurement evaluated the PDW signal from 8.5-9.5 ms because the reproducibility was confirmed. The averaged line integrated electron density from 8.5 – 9.5 m and the line integrated electron density after 15 ms on the discharge measured by Thomson scattering measurement were similar values in HFS injection as shown in Figure VI-1. The formation of electron density profile was assumed the same in the discharges of PDW measurement and the Thomson scattering measurement. The Thomson scattering measurement points were 2 points at 2 ms and 102 ms. To evaluate the most suitable electron density profile, the integrated electron density from the electron density profile by the Thomson scattering measurement was also compared. The electron density profile measured at 102 ms were the more reliable. The electron density profile at the PDW measurement was estimated by multiplying the electron density profile at 102 ms by each factor (FHFS: 1.1, FLFS: 2.7) to match the line integrated electron density by Thomson scattering measurement and the averaged line integrated electron density on the PDW measurement.

Reference in appendix

[A] H. W. KOCH *et al.*, Rev. Mod. Phys., **31**, 920, (1959).

[B] M. Lazar *et al.*, Open Plasma Phys. J., **3**, 1, (2014).

[C] R. K. Janev *et al.*, Tech. Rep. No. 4105, (2003).

[D] A. Wootton, Pvt Rep., (2012).

[E]M. Ishiguro *et al.*, Phys. Plasmas, **19**, 6, (2012).

[F] T. Yoshinaga *et al.*, Phys. Rev. Lett., **96**, 12, (2006).